Simulating Magnetoelectric Sensors in Inhomogeneous Magnetic Fields

Dissertation

for the degree of Dr.-Ing.

Submitted to the Faculty of Engineering
Kiel University

by
Mesut-Ömür Özden

Kiel
2024

First Referee: Prof. Dr. Martina Gerken

Second Referee: Prof. Dr.-Ing. Ludger Klinkenbusch

Date of oral examination: December 11, 2024

In memory of my father

Acknowledgements

This dissertation is the result of many years of dedication and work at the Chair for Integrated Systems and Photonics and the Chair for Computational Electromagnetics at the Department of Electrical and Information Engineering of Kiel University. My special thanks go to Prof. Dr. Martina Gerken for her guidance, leadership, advice, and mentoring throughout the years – and before all else – her patience and lasting support. Many thanks also go to Prof. Dr.-Ing. Ludger Klinkenbusch for the years of cooperation, experience, and the opportunity to grow continuously alongside the students that I had the privilege to support and tutor together with him. Even facing the most difficult of times, the support of both of you kept me on track – thank you.

I would like to thank all colleagues working within the Collaborative Research Center (CRC) 1261 "Magnetoelectric Sensors: From Composite Materials to Biomagnetic Diagnostics" and the German Research Foundation (Deutsche Forschungsgemeinschaft, DFG) for enabling this research. My deep appreciation for meaningful discussions, shared expertise, and new ideas goes to Prof. Dr.-Ing Eckhard Quandt, Prof. Dr.-Ing. Gerhard Schmidt, Prof. Dr.-Ing. Michael Höft, Dr.-Ing. Julius Schmalz, Dr. Matthias Krantz, Dr.-Ing. Jascha Lukas Gugat, Dr.-Ing. Alexander Teplyuk, Dr. Dirk Meyners, Dr.-Ing. Mevlüt Yalaz, and Giuseppe Barbieri.

The years at Kiel University were precious to me, and for making every day there special, I would like to thank all my colleagues throughout the years. My heartfelt appreciation for countless wonderful memories goes to Dr. Yolande Murat, Dr.-Ing. Johannes Bläsi, Dr.-Ing. Igor Titov, Stefanie Lehmann, Hannes Lüder, Christian Richard Kalhöfer, Mona Stölting, Marleen Schweichel, Shi Li, Mihail Balanici, Heather Cavers, Heike Thodt, and Jülf Buschmann.

Lastly, my endless love and gratitude go to the special person that lifted me up whenever I fell down and cheered me on every time I struggled in life. Thank you for believing in me, Marissa.

Declaration

I hereby declare that I have written this dissertation entitled

Simulating Magnetoelectric Sensors in Inhomogeneous Magnetic Fields

independently and without improper external assistance, and that I have identified all quotations of other authors. Furthermore, this thesis has not been, partially or completely, submitted to any other university or institute in the context of an examination procedure. Parts of the content of the work have already been published in my scientific publications and are stated accordingly. I declare that the following work has been written in compliance with the rules of good scientific practice established by the German Research Foundation and furthermore that no academic degree has been withdrawn from me.

Pinneberg, 08.01.2025 — Place, Date

Mesut-Ömür Özden

Scientific Contributions

Journal Publications

1. **M.-Ö. Özden**, A. Teplyuk, Ö. Gümüs, D. Meyners, M. Höft, and M. Gerken, "Magnetoelectric cantilever sensors under inhomogeneous magnetic field excitation," *AIP Adv.*, vol. 10, no. 2, p. 025132, Feb. 2020, doi:10.1063/1.5136239

2. S. Zuo, J. Schmalz, **M.-Ö. Özden**, M. Gerken, J. Su, F. Niekiel, F. Lofink, K. Nazarpour, and H. Heidari, "Ultrasensitive Magnetoelectric Sensing System for Pico-Tesla MagnetoMyoGraphy," *IEEE Trans. Biomed. Circuits Syst.*, vol. 14, no. 5, pp. 971–984, Oct. 2020, doi:10.1109/TBCAS.2020.2998290

3. **M.-Ö. Özden**, J. Schmalz, and M. Gerken, "A Combined Magnetoelectric Sensor and Human Head Model for Biomagnetic FEM Simulations," *IEEE Sens. J.*, vol. 23, no. 24, pp. 30259–30270, Dec. 2023, doi:10.1109/JSEN.2023.3329579

4. **M.-Ö. Özden**, G. Barbieri, and M. Gerken, "A Combined Magnetoelectric Sensor Array and MRI-Based Human Head Model for Biomagnetic FEM Simulation and Sensor Crosstalk Analysis," *Sensors*, vol. 24, no. 4, p. 1186, Feb. 2024, doi:10.3390/s24041186

Conference Talks

1. **M.-Ö. Özden** and M. Gerken, "Trade-off between spatial resolution and sensitivity of magnetoelectric magnetic field sensors," in 2021 *International Conference on Electromagnetics in Advanced Applications* (*ICEAA*), Honolulu, HI, USA: IEEE, Aug. 2021, pp. 124–124, doi:10.1109/ICEAA52647.2021.9539722

2. **M.-Ö. Özden** and M. Gerken, "A joint magnetoelectric sensor and human head model for biomagnetic simulation," in 2022 *International Conference on Electromagnetics in Advanced Applications* (*ICEAA*), Cape Town, South Africa: IEEE, Sep. 2022, pp. 021–021, doi:10.1109/ICEAA49419.2022.9900002

Advised Theses

1. Bachelor's thesis: "Transferfunktion eines magnetoelektrischen Sensors", Ömer Gümüs, 2018

2. Master's thesis: „Erstellung von 3D-Modellen zur quantitativen Flussbildgebung mittels Magnetresonanztomographie“, Eva Peschke, 2018
3. Bachelor's thesis: „Analytische Berechnung und numerische Auswertung der elektrischen Potentialverteilung in sphärischen Strukturen“, Hannah Carstens, 2019

Abstract

The world of biomedical diagnostics is vast, and novel sensing devices with outstanding capabilities enable advanced clinical and technical applications. One diagnostic field of high research interest is biomagnetic measurement, where sensing devices are used to measure the magnetic field emanating from the human body. These measurements can be used by medical experts to monitor the activity of organs such as the heart or brain, and to diagnose the causes of pathological disorders like cardiac arrhythmias and seizures. Artificial signals such as from implanted deep brain stimulation (DBS) electrodes can be measured as well, enabling post-op localization. One approach to measure extremely small biomagnetic signals is to use a sensing device based on the magnetoelectric effect. Such magnetoelectric (ME) sensors offer particularly valuable benefits over competing sensor systems, like the low-cost MEMS manufacturing processes, room-temperature operation, and a limit of detection (LOD) in the $\mathrm{pT}/\sqrt{\mathrm{Hz}}$ range.

The scope of this dissertation includes finite element method (FEM) modeling and simulation of ME magnetic field sensors, arrays of ME sensors, as well as combined models including simplified and magnetic resonance imaging (MRI) based human heads as excitation sources for sensor arrays. The ME sensor behavior is simulated through excitation with homogeneous and inhomogeneous magnetic fields, different orientations and positions of the sensors, as well as different excitation mechanisms, including a small coil around the ME sensor or a dipole source inside a human head.

Results show that cantilever ME sensors exhibit highly position-dependent sensitivity and a simple theoretical point-sensor approximation at the geometric center of the sensor is not accurate. The point of highest sensitivity along the cantilever long axis is located at a distance of approximately 17% of the free sensor length from the clamped position. Furthermore, simulations with a combined model consisting of three orthogonal ME sensors and a simplified human head containing a dipole source show highly position- and direction-dependent behavior of the individual sensors in the array. The sensor output depends on the position and orientation of the source inside of the head, as well as the location and orientation of the individual sensors inside the array, as the ME sensors exhibit a strong sinusoidal dependence with a maximum response at incident magnetic field angles that are parallel to the long axis of the cantilever. Lastly, improving the head model and using an MRI-based head geometry, combined with an array of fifteen ME sensors, results in valuable insights on the magnetic crosstalk effect between adjacent ME sensors in array configurations. Within such an array in a homogeneous excitation field, the outermost ME sensors exhibit significantly

less crosstalk than the innermost sensors, and crosstalk decreases with increasing distance between neighboring sensors, down to a negligible effect at a distance of 5 cm, which corresponds to approximately 20 sensor widths.

The dissertation consists of an introductory chapter, followed by two chapters on the fundamentals of ME sensors and the utilized simulation models. After that, three chapters which consist of the main journal publications including an overview of the author's contribution and a summary of their key scientific findings follow. Finally, the thesis closes with a chapter containing a summary of the scientific contribution, discussion of the results, and outlook on potential future studies in the field of ME sensor modeling and simulation, based on the insights provided by this dissertation.

Zusammenfassung

Die Welt der biomedizinischen Diagnostik ist umfangreich und neuartige Sensorsysteme mit herausragenden Eigenschaften ermöglichen fortschrittliche klinische und technische Anwendungen. Eines der diagnostischen Fachgebiete mit hohem Forschungsinteresse sind biomagnetische Messungen, durch die das magnetische Feld des menschlichen Körpers detektiert werden kann. Mit Hilfe dieser Messungen können medizinische Expertinnen und Experten die Aktivität von Organen wie beispielsweise des Herzens oder des Gehirns überwachen und Ursachen pathologischer Störungen wie Arrhythmien oder Krampfanfällen diagnostizieren. Künstliche Signale wie solche, die durch implantierte Elektroden für die tiefe Hirnstimulation (*deep brain stimulation*, DBS) erzeugt werden, können ebenfalls detektiert werden und ermöglichen beispielsweise die Lokalisierung des Implantats im Kopf im Rahmen postoperativer Untersuchungen. Ein Ansatz, um solche extrem schwachen biomagnetischen Signale zu detektieren, ist die Nutzung eines Sensors, dessen Funktionsweise auf dem magnetoelektrischen (ME) Effekt beruht. Solche ME-Sensoren bieten bedeutsame Vorteile gegenüber konkurrierenden Sensorsystemen, beispielsweise kostengünstige MEMS-Fertigungsprozesse, Betrieb bei Raumtemperatur und eine Detektionsgrenze (limit of detection, LOD) im Bereich von $\mathrm{pT}/\sqrt{\mathrm{Hz}}$.

Der Umfang dieser Dissertation beinhaltet die Modellierung und Simulation auf Basis der Finite-Elemente-Methode (*finite element method*, FEM) von einzelnen ME-Sensoren und Arrays von ME-Sensoren, sowie kombinierte Modelle mit ME-Sensoren und einem vereinfachten oder realistischen menschlichen Kopfmodell auf Basis von Magnetresonanztomographie- (MRT) Messungen als Anregungsquelle für die Sensorarrays. Das Verhalten von ME-Sensoren wird simuliert unter dem Einfluss von homogenen und inhomogenen Anregungsmagnetfeldern, verschiedenen Ausrichtungen und Positionen der Sensoren, sowie je nach Modell unterschiedlichen Anregungsmechanismen, einschließlich einer um den Sensor befindlichen Ringspule oder einer im menschlichen Kopf befindlichen Dipolquelle.

Die Ergebnisse zeigen, dass ME-Sensoren auf Biegebalkenbasis stark positionsabhängige Empfindlichkeiten aufweisen und einfache theoretische Näherungen als Punktsensoren in ihrem geometrischen Zentrum ungenau sind. Der Punkt der höchsten Empfindlichkeit entlang der langen Achse des Biegebalkens ist ca. 17% der freien Sensorlänge vom geklemmten Ende entfernt. Weiterhin zeigen Simulationen mit einem kombinierten Modell, bestehend aus drei zueinander orthogonal angeordneten Sensoren und einem vereinfachten menschlichen Kopf einschließlich Dipolquelle, ein hochgradig positions- und richtungsabhängiges Verhalten von individuellen Sensoren im Array. Das Sensorsignal hängt sowohl von der Po-

sition und Orientierung der Dipolquelle im Kopf als auch der des individuellen Sensors im Array ab, da ME-Sensoren eine sinusoidale Richtungsabhängigkeit aufweisen. Dadurch bedingt entsteht die höchste Sensorantwort bei parallel zur Längsachse des Biegebalkens anliegenden Feldern und sie wird minimal bei Feldern, die orthogonal zur Längsachse anliegen. Schließlich liefert die Verwendung eines akkurateren und verbesserten Kopfmodells auf Basis von MRT-Messungen in Kombination mit einem Array aus fünfzehn ME-Sensoren wertvolle Erkenntnisse zum magnetischen Übersprechen (*crosstalk*) zwischen benachbarten Sensoren in verschiedenen Arraykonfigurationen. In einem solchen Array innerhalb eines homogenen Anregungsfeldes weisen die am weitesten außen liegenden Sensoren ein erheblich geringeres Übersprechen auf als die innen liegenden Sensoren und der Effekt nimmt mit steigendem Abstand zwischen benachbarten Sensoren ab, bis zu einem vernachlässigbaren Wert bei einer Entfernung von 5 cm, was etwa der 20-fachen Breite des Sensors entspricht.

Diese Dissertation besteht aus einem einleitenden Kapitel, gefolgt von zwei Kapiteln zu den Grundlagen von ME-Sensoren und den verwendeten Simulationsmodellen. Die drei darauffolgenden Kapitel enthalten die wissenschaftlichen Veröffentlichungen als Erstautor, einschließlich jeweils eines Überblicks über die den geleisteten Beitrag des Autors und einer Zusammenfassung der wesentlichen wissenschaftlichen Erkenntnisse. Die Doktorarbeit schließt ab mit einem Kapitel, welches die Zusammenfassung des geleisteten Forschungsbeitrags, eine Diskussion der Ergebnisse, sowie einen Ausblick auf mögliche zukünftige Untersuchungen auf dem Gebiet der Modellierung und Simulation von ME-Sensoren beinhaltet, basierend auf den Erkenntnissen aus dieser Dissertation.

Contents

Chapter 1

Introduction

1.1 Aim and Scope of this Dissertation

The human body is a profoundly complex, yet elegantly simple biological machine. Like many other machines, its functioning relies on the flow of electrical currents. Within the body, current flow consists of ionic currents through biological tissues like nerve and muscle cells; a phenomenon which has been of remarkable research interest since at least the 19th century [1]. Ionic currents control the body's activity from down at the cell level all the way up to organs such as the heart and brain. The discovery that electric currents, in general, caused magnetic fields was made in the early 19th century by *Hans Oersted* and soon after formulated into the crucial Biot-Savart law by *Jean-Baptiste Biot* and *Felix Savart* [2, 3].

Many essential medical diagnostics principles function by measuring the electrical activity of the body. Electrodes are placed on the surface of the skin and record the electrical potentials relative to reference points. Well-known applications of this measurement principle include recording the heart activity in an electrocardiogram (ECG), or the brain activity in an electroencephalogram (EEG). These electrical measurements are relatively simple to perform, cost-effective, widely available, and offer high temporal resolution. However, they also come with the inherent drawbacks of electrical measurements such as comparatively low spatial resolution (which may also negatively impact the temporal resolution [4]), requirements of direct contact with a patient's skin (often using conductive gel between the skin and electrode), and the risk of incorrect positioning of electrodes or reversal of leads [5]. In order to overcome these drawbacks and either replace or complement electrical measurements, magnetic measurements based on the underlying bioelectrical activity can be performed. These magnetic measurements offer benefits such as higher spatial resolution and increased patient comfort. Particularly interesting applications arise due to the ability of magnetic field measurement to be taken contactlessly and over small distances. This gives rise to the ability to perform, for example, a fetal MCG in which the cardiac activity of a fetus is magnetically recorded through the maternal abdomen, allowing non-invasive diagnosis of potentially threatening conditions such as arrythmias as early as in the 13th week of pregnancy [6].

Over the last decades, many different magnetometer concepts have emerged from

various scientific disciplines such as engineering, astronomy, or medicine. These sensor systems are promising in the field of biomagnetic measurements, and each of them contains a suite of benefits and drawbacks in certain categories. Among the selection of relevant sensor systems that fall within the context of this thesis are superconducting quantum interference device (SQUID) magnetometers [7–9], optically pumped magnetometers (OPMs) [10, 11], fluxgate magnetometers [12–14], and magnetoelectric (ME) magnetic field sensors [15–17].

SQUID magnetometers have been in use for industrial and academic applications, as well as clinical diagnostics for many decades [7], and remain the gold standard in many biomagnetic measurements [6, 18]. These devices function by the principle of superconduction and utilize Josephson junctions as their active element, enabling a supercurrent to flow in the junction between superconductors [7], [19]. As the measured impedance of the SQUID loop (i.e. the voltage across the Josephson junctions) is a function of the external magnetic flux, the device's sensing principle is transducing magnetic flux into an electric voltage [7]. Based on this measurement principle, SQUIDs can function in different varieties, such as the DC SQUID with two junctions or the RF SQUID with a single junction, and can achieve otherwise unmatched field resolutions in the order of magnitude of 10-17 T [18]. However, they also come with severe challenges and, because of that, are usually only found in large clinics such as university hospitals or in research institutions. Among their main drawbacks is their high financial cost, both in initial acquisition and in maintenance. They require cryogenic cooling with liquid helium [7], large magnetically shielded chambers due to their system size, and severely ill patients often need to be transported over long distances to the location of these rare devices, making large-scale clinical point of care (POC) or ambulatory diagnostics extremely challenging.

OPMs saw a rise in popularity for use in biomedical applications due to their comparatively lower cost at similar magnetic field resolutions compared to SQUIDs. *Shah* and *Wakai* report sensitivities of 6–10 $\mathrm{fT}/\sqrt{\mathrm{Hz}}$ under ideal conditions and a 3-dB bandwidth of around 100 Hz, which would principally make their magnetometer suitable for biomagnetic applications such as MEG and MCG [10]. A major limitation of OPM sensors, however, is their sensitivity to ambient background magnetic fields, such as environmental interferences from the power grid at 60 Hz (in the USA) and generally lower bandwidth than SQUIDs – which is an additional trade-off to their sensitivity [10], [11]. While these devices reach impressive sensitivities, their operation outside of magnetically shielded chambers is challenging due to their inherent susceptibility to external interferences. Although they cannot immediately replace SQUID devices in every regard as of today, future studies such as the investigation of OPM arrays [10] or pulsed OPMs that can operate without shielding [20] might be very promising for the clinical applications of tomorrow.

Another sensing device used for measurements of weak magnetic fields is the fluxgate magnetometer. Historically, fluxgate magnetometers became interesting because of their stability, sensitivity, cheaper operation than SQUIDs and – contrary to OPMs – their ability to measure the components of the magnetic field directly and therefore act as vector magnetometers [12]. The combination of properties such as their high sensitivity, high dynamic range and excellent offset stability

makes them the most widely used type of magnetometer in space applications [13]. Although classical fluxgate magnetometers are not suitable for general measurements of the extremely weak biomagnetic fields of the human body, recent developments for this sensor type show promising results in medical applications, such as the ability to detect the R-peak of the QRS complex of a human cardiogram [14].

In the following, this dissertation will focus on ME sensors as novel devices for measuring extremely small biomagnetic signals. Measurements with these sensors are based on the magnetoelectric effect. Sensing devices based on the magnetoelectric effect utilize the physical principles of magnetostriction and piezoelectricity to transduce a magnetic field into an electric potential [21–23]. Most commonly, such sensors consist of cantilever beams with a composite material layer structure, where the layers are separated by function, i.e., they consist of a separate substrate layer, magnetostrictive layer, and piezoelectric layer. This is done in order to utilize the indirect magnetoelectric effect, which is much more pronounced than the direct magnetoelectric effect [22–25]. Within the category of ME sensors, different approaches for the sensing principle are used. For the approach of direct detection in resonant bending mode, a cantilever ME sensor is designed in such a way that its mechanical resonance frequency matches the frequency of the measured magnetic field, as operating in resonant bending mode sharply increases the ME sensor's sensitivity [17, 26]. In some cases, matching the mechanical frequency to the magnetic field is not feasible, e.g., in direct measurements of the brain activity with typical frequencies well below 100 Hz. In such cases, frequency conversion techniques can be performed to enable wideband measurements at low frequencies with resonant sensors [27]. A different approach is chosen with so-called ΔE-effect ME sensors. This variation functions by utilizing a change in the Young's modulus dependent on the ambient magnetic field [28]. It is electrically excited at a frequency far above that of the measured magnetic field, resulting in the sensor's ability to detect small biomagnetic fields with increased sensitivity utilizing the concept of detuning [29].

Another highly promising approach in state-of-the-art ME sensor research is the surface acoustic wave (SAW) sensor principle, which was already discussed for potential use cases in oscillators and delay lines as early as 1979 [30]. In recent investigations on magnetoelectric SAW sensors, the magnetic material is placed on a delay line between two interdigital transducer (IDT) electrodes that are utilized to excite and receive Love waves, which then travel through the delay line [31]. Through the magnetoelastic effect, an external magnetic excitation field changes the elastic properties of the magnetic material and results in a delayed signal propagation between the two IDTs. The delay imposed on an acoustic wave traveling through the sensor geometry is measured and evaluated to enable extremely low LOD magnetic field sensing.

As the research interest in various ME sensor technologies is ever growing, detailed insights into the working principles and behaviors of these sensing devices are necessary in order to foster their potential for real-world applications. Focal points need to be set for research hypotheses, and theoretical as well as experimental investigations must be conducted with meticulous detail. This work focuses on modeling and 3D finite element method (FEM) simulation of cantilever

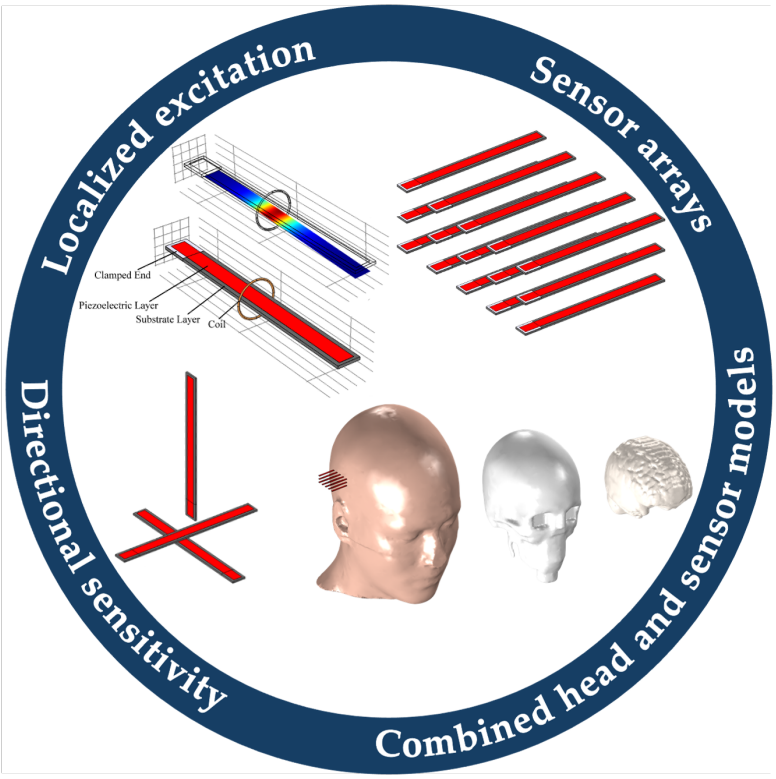

Figure 1.1 – An overview of the ME sensor research models covered in this thesis. Contributions are made in the areas of localized excitation, sensor arrays, directional sensitivity, as well as combined head and sensor models.

ME sensors in resonant bending mode for direct detection. The models are implemented and simulations are performed using the commercial FEM modeling software Comsol Multiphysics (Comsol Inc.) [32]. Additional postprocessing steps such as data extraction and result visualization are performed in Matlab (The Mathworks Inc.) [33]. The range of models that were developed and investigated during this PhD study covers single ME sensors under homogeneous and inhomogeneous magnetic excitation fields, different array configurations of up to fifteen ME sensors, and the combination of ME sensor models with simplified and MRI-based human head models for joint multiscale simulations. The latter approach includes electric dipole sources contained in the human head anatomy, leading to the creation and propagation of a magnetic field through the head's tissue layers, an air environment, and into an array of ME sensors. Figure 1.1 gives an overview of the research interests within the area of ME sensor modeling that are covered in this dissertation.

These detailed multiscale simulations have the potential for providing relevant theoretical insights that would otherwise be challenging to obtain with experimental measurement setups alone. The main findings of this dissertation are documented in the form of three peer-reviewed and published journal articles, each contributing to the previously mentioned research topics. The next section will give a brief outline of the contents of this work, including the main concepts of each journal article.

1.2 Outline

This dissertation is structured into seven chapters, with this introduction being the first. Chapter 2 gives an overview of the physical fundamentals required to understand the contents of this work. It contains Section 2.1, which gives an overview of biomagnetic measurements. Following that, Section 2.2 describes magnetoelectric sensors and their working principles, including subsections on magnetostriction, piezoelectricity, and the magnetoelectric effect. Lastly, Section 2.3 offers an overview of the topic of FEM modeling and simulation, which is the main method of obtaining results and the scientific backbone of this work. Following the fundamentals, Chapter 3 briefly introduces the implemented simulation models presented in this thesis. It is divided into the Section 3.1 describing the ME sensor model theory utilized in this dissertation and Section 3.2 and its subsections, describing the simulation models utilized in the three first-author journal publications. Following the fundamentals and methods, Chapters 4, 5, and 6 each represent the scientific contributions that were achieved during the author's doctoral studies in the form of peer-reviewed journal articles. Starting with Chapter 4, an ME sensor under localized inhomogeneous magnetic field excitation via a small circular coil is presented. Following that, Chapter 5 is dedicated to a combined ME sensor and simplified human head model in a joint multiscale simulation. Lastly, Chapter 6 presents a combined ME sensor array and MRI-based human head model, which contains fifteen individual ME sensors in different array configurations. Each of the three chapters on the peer-reviewed journal publications include a short introduction with a statement about the author's contribution to the work, the complete published journal article, and a summary of the key findings and scientific implications of the article. Lastly, Chapter 7 finalizes the dissertation by giving a summary of the presented work in Section 7.1, discussing the results and their implications in Section 7.2, and by offering an outlook on potential future research interests related to the findings of this dissertation in Section 7.3.

Chapter 2

Fundamentals

The scope of this dissertation covers the modeling and simulation of ME sensors and their interaction with magnetic fields from different excitation sources and within various modeling frameworks. The obtained results are based on numerical simulations utilizing FEM models. The following chapter aims to provide fundamental context for the understanding of this work and its results. It briefly describes the topics of biomagnetic measurements in Section 2.1, magnetoelectric sensors in Section 2.2, and the finite element method in Section 2.3.

2.1 Biomagnetic Measurements

As outlined in the introduction to this thesis, biomagnetic measurements are crucial for both clinical applications as well as academic research. Dating back many decades, researchers were always keen to study human physiology and the bioelectric phenomena originating from our bodies. While the electric activity of organs such as the heart or brain was fundamentally understood and utilized in clinical diagnostics, the magnetic field emanating from the same activity had yet to be thoroughly investigated. In the 1960s, Researchers like *Gerhard Baule*, *Richard McFee* and *David Cohen* studied magnetic fields emanating from the human body caused due to its electrical activity. *Baule* and *McFee* went on and eventually recorded the world's first MCG in 1963 [34, 35]. In one of his works, *Cohen* demonstrated that magnetic measurements contained QRS and T-wave structures similar to those of an electrocardiogram [36]. *Cohen* pointed out – in a pivotal statement – that both MCG and ECG were "powered from the same source" and stated important differences between the two concepts, while also listing benefits of magnetic measurements and forecasting its importance in future research and diagnostics [36].

Figure 2.1 shows two photographs published in a research article by Hämäläinen et al. in 1993 [37]. (a) depicts a SQUID magnetometer system which is located inside a magnetically shielded room at Helsinki University of Technology. The 122-channel neuromagnetometer with its helmet-shaped, liquid-helium-filled dewar surrounds a person's head during the measurement process. (b) shows the 24-channel neurogradiometer in Helsinki. The photograph is taken without the surrounding helium dewar of the machine above a human brain model to illus-

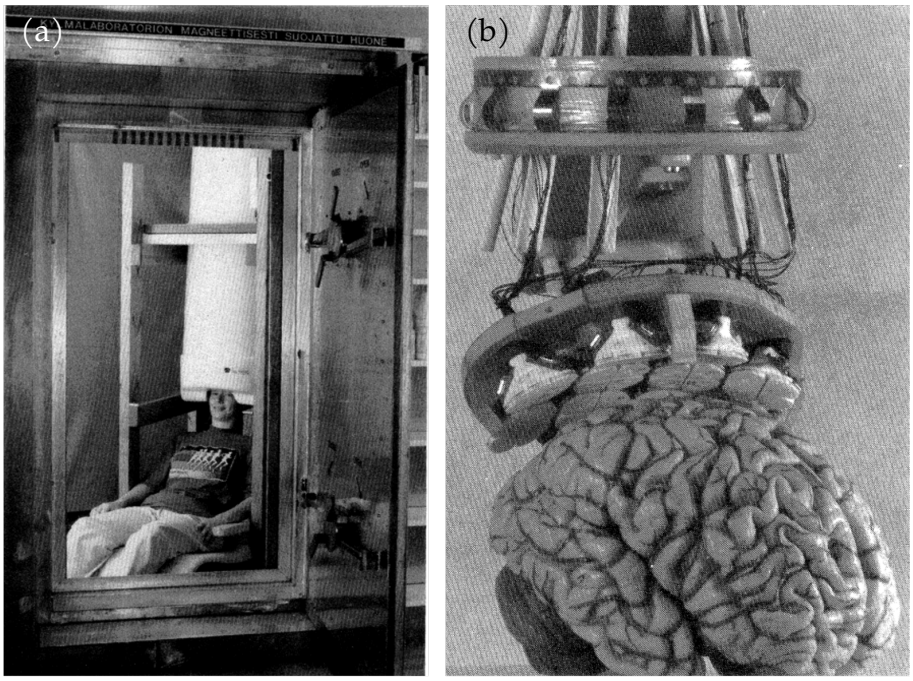

Figure 2.1 – Two photographs published in a 1993 research article from Hämäläinen et al. (a) shows a person sitting in the SQUID magnetometer system, located inside a magnetically shielded room at the Helsinki University of Technology (from [37]). (b) The 24-channel neurogradiometer in Helsinki is shown without the surrounding helium-filled dewar above a human brain model to illustrate the measurement distance and shape of the concave gradiometer measuring head (from [37], reprinted with permission from M. Hämäläinen, R. Hari, R. J. Ilmoniemi, J. Knuutila, and O. V. Lounasmaa, "Magnetoencephalography—theory, instrumentation, and applications to noninvasive studies of the working human brain," Rev. Mod. Phys., vol. 65, no. 2, pp. 413–497, Apr. 1993, doi: 10.1103/RevModPhys.65.413, © 1993 The American Physical Society).

trate the measurement distance and concave shape of the gradiometer measuring head.

In contrast to the large-scale SQUID magnetometer which requires helium cooling and magnetically shielded chambers to operate, newly emerging technologies such as ME sensors do not require these to operate and have additional advantages such as low-cost fabrication, as well as the potential for passive and unshielded operation without the requirement of external cooling or heating (as reiterated from Chapter 1) [15, 17]. Figure 2.2 shows a photograph of a modern packaged and assembled ME sensor on a printed circuit board (PCB) manufactured by the Fraunhofer Institute for Silicon Technology (ISIT) in Itzehoe, Germany [38].

While ME sensors are currently not as sensitive as SQUID devices and therefore not yet suitable for some of the most demanding applications like MEG, the technology is rapidly growing and its capabilities quickly improving. Novel application concepts like real-time magnetic localization of ultrasound probes, magnetic detection of positions and orientations of deep brain stimulation (DBS) electrodes, or magnetic motion analysis for swallowing detection in individuals suf-

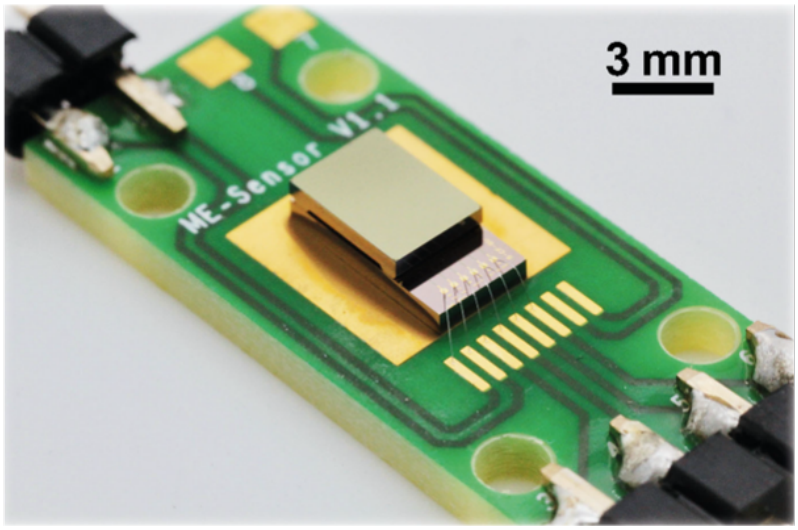

Figure 2.2 – A modern packaged and assembled ME sensor device on a printed PCB (from [38], licensed under Creative Commons Attribution license CC BY 4.0, https://creativecommons.org/licenses/by/4.0/).

fering from dysphagia are flexible and suitable use cases for biomagnetic measurements with ME sensors [39–42]. In the future, cost-efficient, highly sensitive, and flexible measurements could be possible with these devices that can already be manufactured with comparatively simple MEMS processes.

Figure 2.3 gives a qualitative overview of various biomagnetic sources with their corresponding magnetic noise density ($T/\sqrt{Hz}$) and frequency range. Additionally, several magnetic field sensing devices are incorporated in the figure, based on their corresponding limit of detection (LOD) and bandwidth [38, 43]. This comparison illustrates the requirements of different medical applications and how suitable for them current sensor technologies are.

Using a suitable sensing device for a specific biomagnetic measurement, i.e., considering key requirements like bandwidth, dynamic range and sensitivity, is crucial. As Figure 2.3 depicts, ME sensors at resonance can achieve an extremely low LOD only at specific frequencies and narrow bandwidths. While this is a limitation for certain applications, techniques such as frequency conversion can be applied to adjust the resonance frequency of the device in order to match required applications such as MCG or MMG [27]. As described in the introduction to this thesis, SQUID magnetometers are currently considered the gold standard for biomagnetic measurements and clinical applications. Other sensor technologies are rapidly improving, and ME sensors may soon become suitable for a wider range of clinical and research applications in the future. In order to help understanding the working principle of ME sensor technology, the following sections will provide details on the physical effects utilized for measurements with ME sensors.

2.2 Magnetoelectric Sensors

The existence of a material exhibiting a linear causality between its electric polarization and an applied magnetic field was first hypothesized by *Landau* and *Lifshitz*

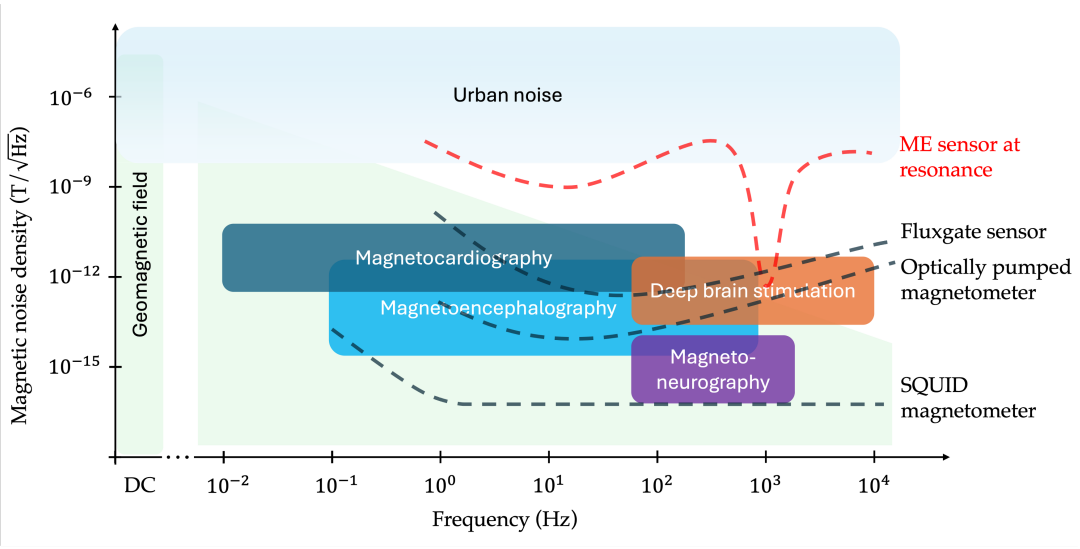

Figure 2.3 – A qualitative comparison of magnetic noise density values ($T/\sqrt{Hz}$) for different biomedical applications and related magnetic measurement devices. While devices such as the ME sensor at resonance can accomplish LODs suitable for applications related to magnetocardiography or deep brain stimulation electrodes, the SQUID magnetometer is the gold standard for biomagnetic measurements (based on [38, 43]).

in 1958, then later predicted theoretically within Cr_2O_3 by *Dzyaloshinskii* in 1959, and finally proven experimentally in the very same material by *Astrov* in 1960 in the former Soviet Union [21, 22]. Today, many different approaches for magnetoelectric sensors exist in literature, with some examples of them presented in the introductory chapter to this thesis. The basis for their functioning, however, comes down to three crucial physical effects, namely: magnetostriction, piezoelectricity, and the magnetoelectric effect. The following sections will briefly introduce these effects and highlight their importance for the operation of ME sensors.

2.2.1 Magnetostriction

The lowly humming noise of an electric power adapter plugged into a wall outlet is something most people are familiar with. Within these devices, transformers are responsible for turning the supplied 230 V of the outlet into a much lower voltage suitable to charge the batteries of smartphones, operate computers, and power countless other household appliances. What causes the audible humming is the same principle that allows us to operate ME sensors in the first place: the magnetostrictive effect. It describes the magnetoelastic coupling inside anisotropic ferromagnetic crystal structures leading to elastic deformation based on magnetization of the material [19]. In 1842, *James Prescott Joule* discovered that some materials would exhibit a change in shape while maintaining a constant volume in response to an applied magnetic field – the effect that we know as Joule magnetostriction today [19, 44]. The change in shape can manifest as an elongation of a material by a length ΔL when affected by an external magnetic field. This elongation is caused by the orientation of magnetic domains inside the material and is dependent on the strength and direction of the external magnetic field, as illustrated in

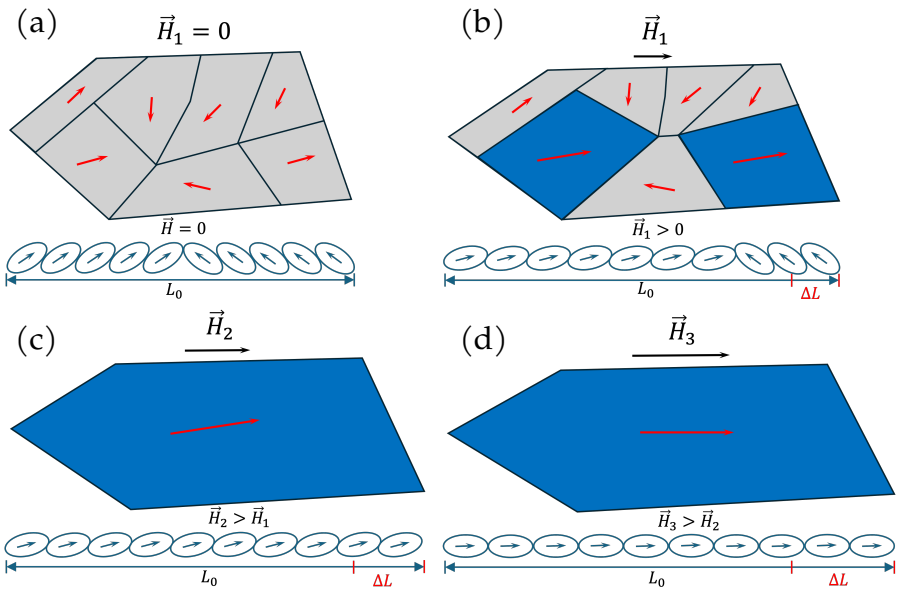

Figure 2.4 – An illustration of the magnetostrictive effect. In (a), no external magnetic field is applied to the material and the magnetic domains are oriented stochastically (or to a certain degree organized in different *Weiss domains*), and therefore in sum exhibit no net magnetization. In (b), adding an external magnetic field results in energetically favorable domains expanding at the expense of unfavorable domains, and further increasing the field strength in (c) results in total favorable domain expansion. An even further increase results in the rotation and alignment of the magnetic domain orientation with the magnetic field direction of the externally applied field (based on [45, 46]).

Figure 2.4.

At the initial stage without an applied external magnetic field, a magnetostrictive material with length L_0 exhibits magnetic domains which are not uniformly oriented, as depicted in Figure 2.4 (a). Upon applying an external magnetic field $\vec{H}_1$, the magnetic domains which are oriented energetically favorable to the direction of the field expand, while unfavorably oriented ones contract, as seen in (b) [45]. Further increasing the magnetic field strength results in the entire material exhibiting a complete energetically favorable domain expansion (c) and even further increase of the field strength results in rotation and alignment of the magnetic domain orientation with the field direction, leading to a saturation condition (d) [45]. The resulting elongation of the material is illustrated under each subfigure with an additional ΔL segment and corresponds with the orientation of the electron hulls, which is directly affected by the magnetic moments through the electrons' spin-orbit coupling [46], [47].

In the case of Joule magnetostriction, this change in length ΔL relative to the initial length without applied magnetic field L_0 can be used to calculate the magnetostrictive constant λ and the material may exhibit elongation or contraction depending on the sign of this constant [45]:

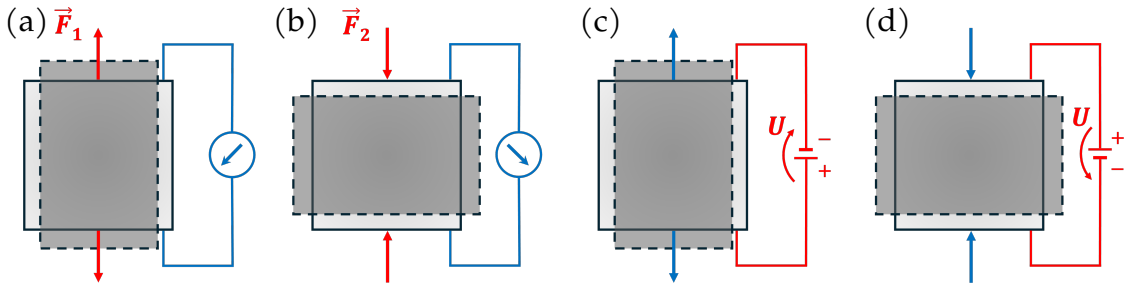

Figure 2.5 – The direct piezoelectric effect is illustrated in (a) and (b). The externally applied force $\vec{F}_1$ stretches the material in vertical direction, while $\vec{F}_2$ compresses it, resulting in opposite polarization signs and measurable electric potentials. In (c) and (d), the inverse piezoelectric effect is demonstrated, where applied electric fields with different signs result in either stretching or compression of the material. The applied forces and voltages are marked in red, while the resulting behavior is highlighted in blue (based on [49]).

$$\lambda = \frac{\Delta L}{L_0}. \tag{2.1}$$

An important coefficient used throughout the simulations presented in this thesis is the piezomagnetic coefficient $\boldsymbol{d}_{\mathrm{m}}$. Analogously to the use of the piezoelectric coefficient $\boldsymbol{d}$ to describe electromechanical coupling in piezoelectric materials, the piezomagnetic coefficient $\boldsymbol{d}_{\mathrm{m}}$ (a third order tensor) describes the change of the magnetostriction tensor $\boldsymbol{\lambda}$ (a tensor consisting of several magnetostriction constants) depending on a change in applied magnetic field intensity $\vec{H}$ [46, 48]:

$$\boldsymbol{d}_{\mathrm{m}} = \frac{\partial \boldsymbol{\lambda}}{\partial \vec{H}}. \tag{2.2}$$

As transducers of an external magnetic field to a measurable electric potential, ME sensors would not be functional without utilizing materials that exhibit the magnetostrictive effect. Combined with the principle of piezoelectricity, which is the subject of the following section, these sensing devices become operational.

2.2.2 Piezoelectricity

A lot of daily appliances, ranging from cigarette lighters and microphones to printer ink jets, utilize some variation of the piezoelectric effect. It describes the property of certain crystalline materials to exhibit a change of electric polarization within the material in reaction to its elastic deformation. Consequently, the polarization change results in an electric potential, the sign of which depends on the properties of the crystal and varies between the material being stretched or compressed in a certain direction, as illustrated in Figures 2.5 (a) and (b). The opposite of this effect is called inverse piezoelectric effect. Here, applying an electric field to the material results in stretching or compression of it, depending on the sign of the voltage and the crystal structure. Figures 2.5 (c) and (d) illustrate the reaction of the material to opposite polarizations of a connected voltage source.

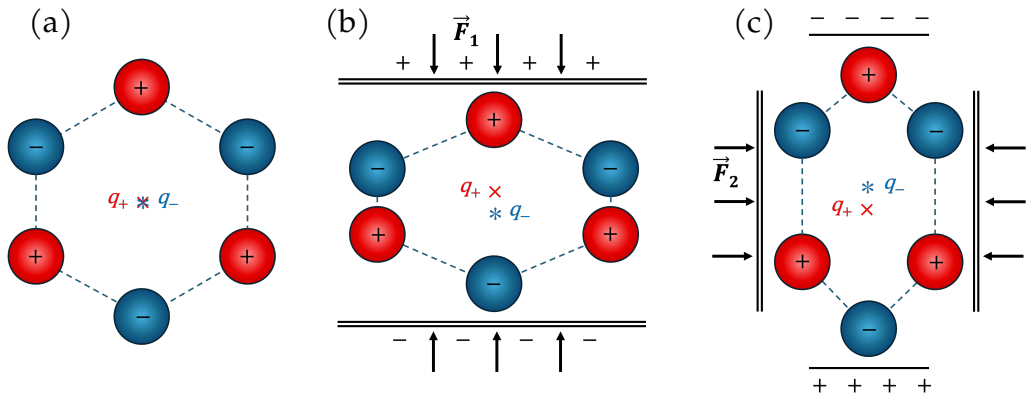

Figure 2.6 – Two-dimensional illustration of a quartz crystal and its centers of charge (a) without externally applied force, (b) with externally applied force $\vec{F}_1$ along the polar axis, and (c) with externally applied force $\vec{F}_2$ perpendicular to the polar axis (based on [43, 53]).

As a relational value for the charge per area $(\mathrm{C/m^2})$ on the surface of the polarized material, the electric flux density $\vec{D}$ can be calculated from the piezoelectric coefficient d multiplied with the mechanical stress $\boldsymbol{T}$ [50]:

$$\vec{D} = \boldsymbol{dT}. \tag{2.3}$$

Conversely, for the inverse piezoelectric effect, the mechanical strain $\boldsymbol{S}$ is dependent on the electric field strength $\vec{E}$ and the same piezoelectric coefficient $\boldsymbol{d}$, which is generally a third order tensor [46]:

$$\boldsymbol{S} = \boldsymbol{d}\vec{E}. \tag{2.4}$$

In order to exhibit piezoelectric properties, a crystal has to consist of point groups without an inversion center, a condition which is a prerequisite for the existence of a polar axis within the structure that enables the effect to occur [49, 51, 52]. Figure 2.6 illustrates the piezoelectric effect on an exemplary 2D quartz crystal structure [53]. In Figure 2.6 (a), a quartz crystal with its negatively charged oxygen and positively charged silicon atoms is given. Without applying any external forces, the structure is in equilibrium and the centers of the negative and positive charges are aligned. This state results in a neutral charge of the material. If an external force $\vec{F}_1$ is applied along the polar axis, the centers of the negative and positive charges shift, resulting in a polarization of the material. This relationship between direction of the applied force and polarization is called longitudinal piezoelectric effect and is illustrated in Figure 2.6 (b). If an external force $\vec{F}_2$ is applied in perpendicular direction, the polarization occurs orthogonally to the applied force, resulting in the transverse piezoelectric effect [43].

The piezoelectric effect is a crucial part of the functioning principle for ME sensors. In conjunction with the magnetostrictive effect, it enables the occurrence of the magnetoelectric effect which will be described in the following section.

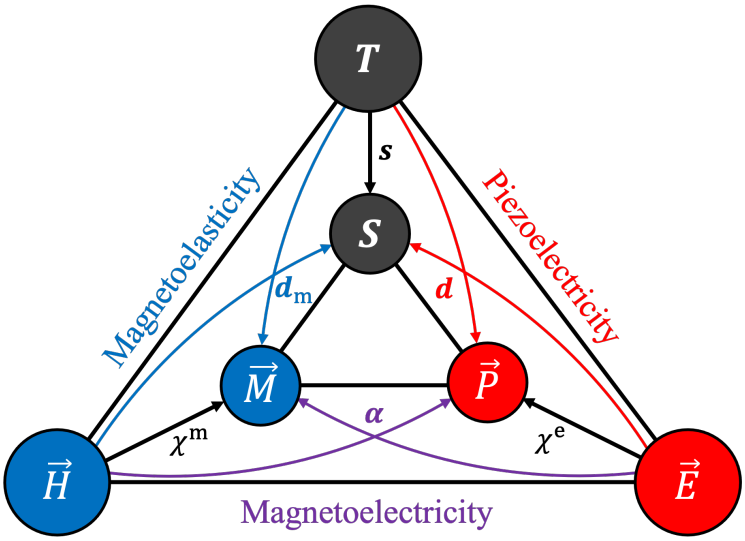

Figure 2.7 – The interconnections between magnetoelasticity, piezoelectricity, and magnetoelectricity. Based on the coupling of different effects and material properties, the pathways of the direct and indirect ME effects can be identified (based on [43, 56]).

2.2.3 Magnetoelectric Effect

The magnetoelectric effect (ME effect) is the namesake for ME sensors and consists of the combination of the magnetostrictive and piezoelectric effects. It describes the change of an electric field depending on the change of a magnetic field. In the context of ME sensor research, this relationship is known as the ME coefficient $\boldsymbol{\alpha}_{\mathrm{ME}}$:

$$\partial \vec{E} = \boldsymbol{\alpha}_{\mathrm{ME}} \partial \vec{H}. \tag{2.5}$$

Two types of ME effects are known: the direct and indirect ME effect. While the direct effect is exhibited in single-phase materials that combine magnetostrictive and piezoelectric properties [54], the much more pronounced indirect ME effect can be achieved by joining different materials with either piezoelectric or magnetostrictive properties into a composite material [25]. These composite materials consist of mechanically coupled piezoelectric and magnetostrictive layers, each subject to the corresponding effect based on their material parameters. Figure 2.7 illustrates the connection between magnetoelasticity, piezoelectricity, and magnetoelectricity. The pathways that the direct and indirect ME effects follow can be highlighted: While the direct ME effect would lead from a magnetic field $\vec{H}$ to a polarization $\vec{P}$ via the ME coefficient $\boldsymbol{\alpha}_{\mathrm{ME}}$, the indirect ME effect of a composite material is based on the magnetic field leading to a mechanical strain $\boldsymbol{S}$ inside the magnetostrictive material via the piezomagnetic coefficient $\boldsymbol{d}_m$, which in turn results in a mechanical stress $\boldsymbol{T}$ and the subsequent polarization $\vec{P}$ of the piezoelectric material via the piezoelectric coefficient $\boldsymbol{d}$. [25, 43, 55].

The sensor models described in this dissertation simulate composite materials exhibiting the indirect ME effect in order to leverage the increased sensitivity of

the resulting sensor systems. The combined magnetic, electrical, and mechanical properties of the separate material layers enable the ME sensor to function as a measurement device capable of sensing extremely weak biomagnetic fields in a variety of frequency ranges and applications.

2.3 Finite Element Method

The finite element method is a powerful numerical calculation method that can be used to solve extensive systems of differential equations. It is of major importance in several fields of engineering, physics, and mathematics in both research and industry. Automotive developers rely on FEM to calculate mechanical stresses and strains on a vehicle's drivetrain components, aerospace engineers utilize it to model heat transfer rates between different materials in an aircraft, and biomedical researchers apply it to simulate fluid flow in microfluidic channels of lab-on-chip biosensors.

The concept of the method is to break down extremely complex problems, which cannot be handled by conventional or analytical methods (e.g. due to the complexity of their materials, geometry, boundary conditions, or number of degrees of freedom) into a finite number of small, interconnected elements. After this breakdown (or discretization) step, the initial geometry can be represented as a mesh of elements and their connected nodes. Depending on the nature of the problem, different boundary conditions, material parameters, and physical effects can then be prescribed to different mesh elements. In a simple case, the calculation of stress and strain experienced by a metallic cantilever beam that is fixed on one end and displaced on the other end can be performed. Here, the relation between force, stiffness of the material, and displacement can be utilized to calculate the stress and strain in each node of the mesh, and therefore in the entire geometry. A crucial part of this simulated behavior is to calculate the stiffness matrix for each mesh element, which is performed by either direct or iterative solvers, such as the Galerkin method of weighted residuals. Once the stiffness matrix of each element is obtained, knowledge of the interconnections of the mesh elements allows for constructing the global stiffness matrix and therefore enables solving the equation for the desired variable in the entire cantilever geometry. One thing to keep in mind is that FEM simulation results are always numerical approximations of the ideal solution, and therefore not ideal themselves. The quality of said solution highly depends on the number of degrees of freedom of the model. This, in turn, is dependent on utilized physics, boundary conditions, number, and shape of mesh elements – the finer the resolution of the mesh, the higher the number of degrees of freedom. In practical applications, one must find a compromise between the better approximation of a solution resulting from a high number of degrees of freedom and the computational requirements like processing power, memory use, and calculation time [57, 58].

In order to perform numerical FEM calculations, specialized software is necessary. Different software tools exist for this purpose, ranging from specialized open-source packages used in academia, to commercial solutions for a wide range of industrial applications. One such commercial software is Comsol Multiphysics, which was used to calculate the results throughout the works presented in this

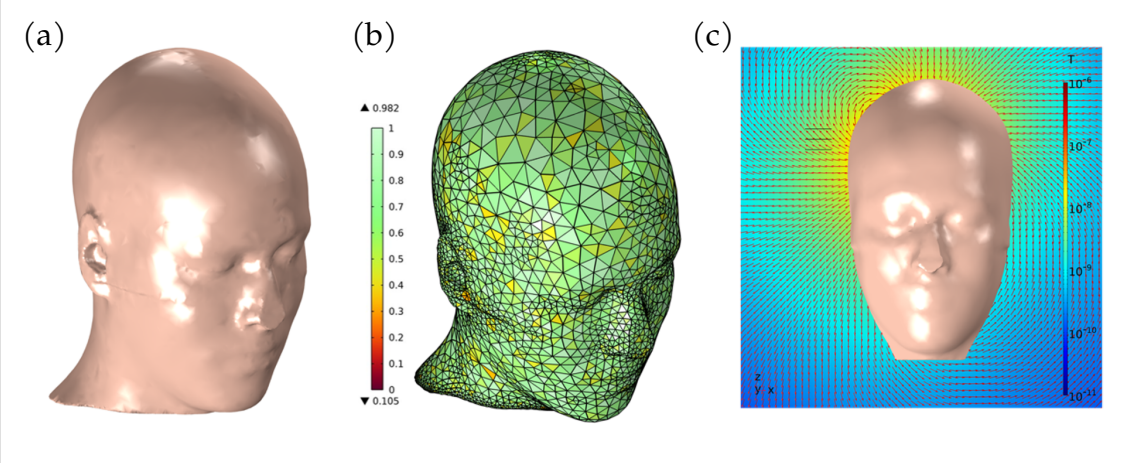

Figure 2.8 – The illustration shows three key aspects of setting up and evaluating an FEM model, on the basis of the human head model from the final journal publication presented in Chapter 6 of this dissertation [39]. (a) depicts the skin layer as the outermost compartment of the head. In (b) the geometry is then subdivided into the finite elements, which in this case results in a 3D mesh of tetrahedral elements. A typical figure of merit for the mesh is the skewness, which is shown here. (c) shows a graphical evaluation of the results after running the simulation. This example visualizes the magnetic flux density norm and direction resulting from an electric source located inside the head geometry.

dissertation. The software offers a built-in material library, integrated physics interfaces for mechanical, electrical, and magnetic models, as well as modeling specific physical properties such as magnetostriction and piezoelectricity and the coupling between them in multiphysics simulations. Utilizing the software's integrated features offers the benefit of simple and efficient collaboration between researchers while assuring comparability between results. Additionally, the software offers an application programming interface (API) to Matlab and similar tools for script-based adjustments and execution of simulations, as well as post-processing of results.

Figure 2.8 illustrates some of the key aspects of setting up and evaluating the FEM models that are specific to this work. The model shown in the illustration is that of the human head described in the final journal publication of this thesis [39]. It exemplifies three important stages in creating and evaluating an FEM model. Firstly, Figure 2.8 (a) depicts the skin layer as the outermost compartment of the head geometry. Secondly, (b) illustrates the surface of the tetrahedral finite element mesh that the entire geometry is subdivided into and solved for. It additionally visualizes the skewness of the mesh on a color scale, which is an important figure of merit. Finally, (c) shows a graphical evaluation of the solved simulation, in this case, the magnetic flux density norm and direction propagating from a source located inside the head outwards, e.g., to the volume of an ME sensor array geometry adjacent to the head.

Following this briefly summarized principle of the FEM and a first glimpse at one of the model geometries created and published in the scope of this dissertation,

the next chapter will include descriptions of and background information on the main models that contributed to this work.

Chapter 3

Simulation Models

A solid understanding of the physical principles behind ME sensors is required to be able to create accurate numerical models of them and evaluate simulation results. The previous chapter gave an overview of the most crucial physical effects and dependencies necessary for the functioning of ME sensors. Building upon those fundamental understandings, the following chapter will introduce the specific FEM simulation models that were created, calculated, and reported on within the scope of three journal publications that contribute to this cumulative work.

3.1 ME Sensor Model Theory

In general, the theoretical ME sensor model for FEM simulation can be described with sets of partial differential equations (PDEs) and constitutive equations, relating to prescribed physical effects and material properties. Many early numerical studies were published at a time where no commercial finite element package was available which was specifically designed to solve multiferroic systems, as described by *Blackburn et al.* in 2008 [23]. To overcome this challenge, researchers utilized versatile modeling software like Comsol Multiphysics [32], Ansys Mechanical [59] or CST Studio Suite [60] and manually entered the relevant equations in order to create a solvable system of PDEs [23, 61, 62].

The fundamental equations for the electromagnetic domain in the generalized system of PDEs are Maxwell's equations, based on a time-harmonic steady state [43]:

$$\nabla \times \vec{H} = \vec{J} + j\omega\vec{D}, \tag{3.1}$$

$$\nabla \times \vec{E} = -j\omega\vec{B}, \tag{3.2}$$

$$\nabla \cdot \vec{D} = \varrho_{\mathrm{v}}, \tag{3.3}$$

$$\nabla \cdot \vec{B} = 0. \tag{3.4}$$

Maxwell's equations are given in phasor form in (3.1)–(3.4), leveraging the time-harmonic steady state condition and the phasor definition:

$$\vec{G}(t) = \Re\left\{\vec{G}e^{j\omega t}\right\}. \tag{3.5}$$

The electric and magnetic field intensities as well as electric and magnetic flux densities are given with $\vec{E}$, $\vec{H}$, $\vec{D}$ and $\vec{B}$. $\vec{J}$ is the electric current density and ϱ_v the volume charge density. In previous work on ME sensor models, the general assumption of $\vec{J} = 0$ is made and applying the divergence to Equation (3.1) with Equation (3.6) yields Equation (3.7) and implies that no volume charge density exists [43, 46]:

$$\nabla \cdot \left(\nabla \times \vec{H}\right) \equiv 0 \tag{3.6}$$

$$\nabla \cdot \vec{D} = 0. \tag{3.7}$$

While this is the general formulation in previous literature on ME sensor modeling, depending on the complexity of the model and its setup, a volume charge density can exist in certain material domains (leading to the formulation in Equation (3.26) later in this section).

For linear elastic materials and simplified problems such as springs or 1D cantilevers, Hooke's law is a fundamental equation which defines that an applied force F to the material with a spring constant D results in an extension displacement Δl [43, 63]:

$$F = D \cdot \Delta l. \tag{3.8}$$

Similarly, the law can also be stated by relating the mechanical stress T to the mechanical strain S via the Young's modulus E (within the elastic limit of a material):

$$T = S \cdot E. \tag{3.9}$$

In the case of more complex, multidimensional problems such as ME sensor simulation, the general relationship between mechanical stress and strain is described by a stiffness tensor, as seen in Equation (3.10) below.

Based on the fundamental relations defined in Maxwell's equations, Newton's law, linear constitutive material equations, material parameters, and elasticity relations, the following equations throughout this section describe the typical setup of PDEs and constitutive material equations used to configure a solver [23, 62, 64–67]:

$$\boldsymbol{T} = \boldsymbol{c}^{EH}\boldsymbol{S} - \boldsymbol{e}^{\top}\vec{E} - \boldsymbol{e}_\mathrm{m}^{\top}\vec{H}, \tag{3.10}$$

$$\vec{D} = \boldsymbol{e}\boldsymbol{S} + \boldsymbol{\varepsilon}^S \vec{E}, \tag{3.11}$$

$$\vec{B} = \boldsymbol{e}_{\mathrm{m}}\boldsymbol{S} + \boldsymbol{\mu}^S \vec{H}. \tag{3.12}$$

Here, $\boldsymbol{T}$ and $\boldsymbol{S}$ denote the mechanical stress and strain tensors. $\boldsymbol{c}^{EH}$, $\boldsymbol{e}$ and $\boldsymbol{e}_{\mathrm{m}}$ are the stiffness, strain to electric field and strain to magnetic field coupling tensors; the permittivity and permeability are denoted by $\boldsymbol{\varepsilon}^S$ and $\boldsymbol{\mu}^S$.

To solve for the mechanical displacement $\vec{u}$, electric potential V and magnetic vector potential $\vec{A}$, which are the independent variables, the PDEs (3.13)–(3.15) are utilized [62]:

$$\nabla \cdot \boldsymbol{T} = -\rho\omega^2 \vec{u}, \tag{3.13}$$

$$\nabla \cdot \vec{D} = 0, \tag{3.14}$$

$$\nabla \cdot \vec{B} = 0. \tag{3.15}$$

Here, the particle density ρ, displacement vector $\vec{u}$, and angular frequency ω are described. Finally, Equations (3.16)–(3.18) typically link the constitutive material Equations (3.10)–(3.12) to the PDEs (3.13)–(3.15) to delineate the sensor response [62]:

$$\boldsymbol{S} = \frac{1}{2}\left[(\nabla\vec{u})^\top + \nabla\vec{u}\right], \tag{3.16}$$

$$\vec{E} = -\nabla V, \tag{3.17}$$

$$\vec{B} = \nabla \times \vec{A}. \tag{3.18}$$

Due to the inherent gauge freedom that Equation (3.18) is subjected to, the simulation models presented in this work utilize the Coulomb gauge condition:

$$\nabla \cdot \vec{A} = 0. \tag{3.19}$$

Simulation of multiferroic structures is relevant in many different scientific fields and for a large variety of applications. Over time, updated versions of the modeling tools were released and provided powerful, built-in modules to solve specifically for magnetostrictive and piezoelectric properties. The modeling work in this dissertation is performed using such built-in solvers for multiferroic materials in Comsol, for the most part eliminating the need to manually configure PDEs and use universal solvers. Instead, optimized interfaces and predefined coupling mechanisms for magnetostriction and piezoelectricity can be utilized, speeding up

the build process of new models, simplifying collaboration with other researchers, and reducing the complexity for introducing advanced model environments and components such as head models and different excitation mechanisms in combined models [39, 68, 69]. These built-in modules utilize the same general equation systems, relations, and material parameters as the equivalent PDEs from literature described in Equations (3.10)–(3.18), but due to the nature of the component-wise model configuration in Comsol, the equations are grouped by material properties and physical effects. This means, for example, that the equation describing the stress tensor does not incorporate electric and magnetic properties by including both coupling coefficients into one equation, but rather that the piezoelectric and magnetostrictive materials are first configured with their own respective stress tensors separately, and then subsequent calculations are performed using both components. As opposed to the previously given general formulation based on literature, the exact formulation for the built-in, component-wise set of PDEs (as displayed within Comsol Multiphysics 6.1) can be extracted from the final publication for this dissertation and will be described next [39]. Although different nomenclature may be used, the physical effects described are the same, e.g., the mechanical stress $\boldsymbol{T}$ and strain $\boldsymbol{S}$ described in Equations (3.13) and (3.16) are equivalent to the mechanical stress $\boldsymbol{S}$ and strain $\boldsymbol{\varepsilon}$ given in Equations (3.20) and (3.22).

The following equations are part of the first interface of the model, the *solid mechanics* interface. These equations couple mechanical, electrical and magnetic behavior of the ME sensor model and are separated into specific physics nodes with respective terms for each of the multiferroic layers' properties. Starting with Equations (3.20)–(3.23), the *linear elastic material* node is introduced. This node contains broader mechanical properties of the sensor model which are not uniquely and specifically related to the magnetostrictive or piezoelectric layers. The Young's modulus E and Poisson's ratio ν are parameters for the stiffness tensor $\boldsymbol{C}$ in between the mechanical stress $\boldsymbol{S}$ and the strain $\boldsymbol{\varepsilon}$ in the silicon substrate, as described in Equations (3.21) and (3.23):

$$-\rho\omega^2\vec{u} = \nabla \cdot \boldsymbol{S}, \tag{3.20}$$

$$\boldsymbol{S} = \boldsymbol{C} : \boldsymbol{\varepsilon}, \tag{3.21}$$

$$\boldsymbol{\varepsilon} = \frac{1}{2}\left[(\nabla\vec{u})^\top + \nabla\vec{u}\right], \tag{3.22}$$

$$\boldsymbol{C} = \boldsymbol{C}\left(E, \nu\right). \tag{3.23}$$

Within the solid mechanics interface, the *magnetostrictive material* node is set up next. In Equation (3.24), the stress resulting specifically due to magnetostrictive material properties is calculated in relation to the elasticity matrix $\boldsymbol{c}_H$, the coupling matrix in Voigt notation $\boldsymbol{e}_{HS}$, the strain and the magnetic field intensity. Additionally, the relation between magnetic flux density $\vec{B}$, relative permeability

$\mu_{\mathrm{r}S}$, magnetic field intensity $\vec{H}$, coupling matrix, and strain are given in Equation (3.25):

$$\boldsymbol{S} = \boldsymbol{c}_H : \boldsymbol{\varepsilon} - \vec{H} \cdot \boldsymbol{e}_{HS}, \tag{3.24}$$

$$\vec{B} = \mu_0 \mu_{\mathrm{r}S} \vec{H} + \boldsymbol{e}_{HS} : \boldsymbol{\varepsilon}. \tag{3.25}$$

The last set of equations within the *solid mechanics* interface covers the *piezoelectric material* node with its equations specifically applicable to the piezoelectric layer, analogous to the previously described layer equations specific to the magnetostrictive material:

$$\nabla \cdot \vec{D} = \varrho_{\mathrm{v}}, \tag{3.26}$$

$$\boldsymbol{S} = \boldsymbol{c}_E : \boldsymbol{\varepsilon} - \vec{E} \cdot \boldsymbol{e}_{ES}, \tag{3.27}$$

$$\vec{D} = \varepsilon_0 \varepsilon_{\mathrm{r}S} \vec{E} + \boldsymbol{e}_{ES} : \boldsymbol{\varepsilon}. \tag{3.28}$$

The built-in formulation for Gauss' law is given in Equation (3.26), with the electric flux density $\vec{D}$ and volume charge density ϱ_{v}. Analogous to the magnetostrictive material, the piezoelectric material's elasticity matrix $\boldsymbol{c}_E$ and coupling matrix in Voigt notation $\boldsymbol{e}_{ES}$ are given, as well as the electric field intensity $\vec{E}$ and the relative permittivity $\varepsilon_{\mathrm{r}S}$ in relation to the stress and electric flux density in Equations (3.27) and (3.28), respectively. The piezoelectric layer is modeled utilizing the stress-charge form and the magnetostrictive layer according to the stress-magnetization form. In addition to the *solid mechanics* node, which is responsible for the elastic material properties and coupling between sensor layers and to which Equations (3.20)–(3.28) are assigned to, the models shown in this dissertation also utilize the *magnetic fields* and *electrostatics* physics with their respective definitions and equations. The following Equations (3.29)–(3.33) based on the integrated physics nodes and boundary conditions of the *magnetic fields* and *electrostatics* interfaces are utilized to govern the electrical and magnetic behavior of the ME sensor and head models:

$$\nabla \times \vec{H} = \sigma \vec{E} + j\omega \vec{D}, \tag{3.29}$$

$$\vec{B} = \nabla \times \vec{A}, \tag{3.30}$$

$$\vec{E} = -\nabla V - j\omega \vec{A}, \tag{3.31}$$

$$\vec{D} = \varepsilon_0 \varepsilon_{\mathrm{r}} \vec{E}, \tag{3.32}$$

$$\vec{B} = \mu_0 \mu_\mathrm{r} \vec{H}. \tag{3.33}$$

Equations (3.29) and (3.30) are part of the *magnetic fields* interface and use the Ampère-Maxwell equation with σ as the specific conductivity and relate the magnetic flux density to the magnetic vector potential $\vec{A}$. Equation (3.31) correlates electric field, electric potential, and vector potential which are part of the *electrostatics* interface. Lastly, the additional Equations (3.32) and (3.33) are defined in the generic *Ampère's law* node of the *magnetic fields* interface. These are general constitutive equations relating electric and magnetic fields and flux densities with their respective permittivity and permeability for materials which do not have properties governed by the specific boundary conditions for piezoelectricity or magnetostriction, e.g., the silicon substrate. In addition, the generic Equation (3.32) is used for the magnetostrictive layer as it does not exhibit piezoelectric properties and Equation (3.33) for the piezoelectric layer, which in turn does not exhibit magnetostrictive properties [39].

The equations that are described above enable performing 3D numerical finite-element method simulations on the fully coupled ME sensor models, including the magnetostrictive, piezoelectric, and magnetoelectric effects, several excitation setups, as well as two different human head models in conjunction with ME sensor arrays in combined multi-scale models.

3.2 Overview of Utilized Simulation Models

The following sections give a brief overview of the simulation models utilized for each of the three first author journal publications contributing to this thesis. The focus will be on illustrating and describing the components, geometry, and research question of each model in a nutshell, while the full publications included in Chapters 4–6 of this dissertation contain detailed methodology, results, and discussion.

3.2.1 Inhomogeneous Excitation Model

In the first publication, *Özden et al.* (2020) [68], a single ME sensor model in an inhomogeneous excitation setup is introduced. The cantilever beam is locally surrounded by a small ring-shaped copper coil with one winding, inducing a strongly localized magnetic field around a small section of the sensor. The position of the coil can be varied along the long axis of the cantilever. Figure 3.1 shows the geometry setup of this model.

The scientific question that this investigation aims to answer is whether the ME sensor exhibits homogeneous sensitivity along its longitudinal axis, or a gradient of sensitivity along the cantilever length can be observed. Previously, studies on this type of ME sensor assumed homogeneously applied excitation magnetic fields. Evaluating the sensor response in a homogeneous excitation field, however, is unsuitable to provide information on specific local sensitivity differences of the sensor geometry, e.g., along the longitudinal sensor axis. Because the sensor has a size on the order of a few millimeters, post-processing steps or localization

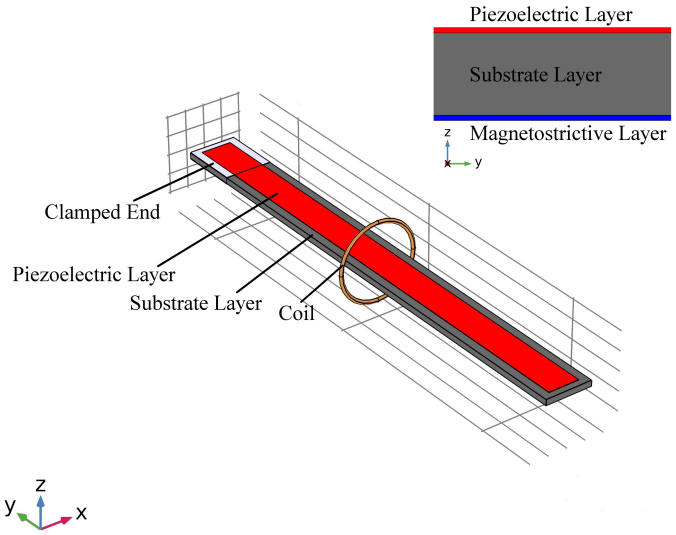

Figure 3.1 – An illustration of the sensor and coil model from the first main author publication contributing to this dissertation. The ME sensor consists of a silicon substrate with a piezoelectric and magnetostrictive layer on opposite sides of the substrate, a clamped end, and a free end. The coil is positioned to surround the cantilever geometry and varies its location longitudinally between the free and clamped end in y-direction. A strongly localized, inhomogeneous magnetic field was induced via electric current flow in the coil and applied as an excitation field. Based on its electric response for each coil position, local sensitivity variations along the long axis of the ME sensor are investigated. An experimental setup for the same concept is implemented and a comparison between simulated and measured results is featured in this publication (from [68], licensed under Creative Commons Attribution license CC BY 4.0, https://creativecommons.org/licenses/by/4.0/).

algorithms cannot simply regard the device as a point sensor or assign the maximum sensitivity to the geometric center of the sensor. By utilizing a small coil as a localized excitation mechanism and systematically applying this inhomogeneous excitation field to different positions along the sensor's long axis, the sensor response depending on the coil position can be investigated.

In addition to the FEM model and simulation results, this sensor and excitation setup are experimentally evaluated. The measured data shows good agreement with the model's behavior and validates the simulation setup. The same ME sensor geometry is subsequently used in the following investigations described in the second and third publication.

3.2.2 Combined ME Sensor and Simplified Human Head Model

The second publication, *Özden et al.* (2023) [69], introduces an array of three orthogonally placed ME sensors that are geometrically identical to the single sensor shown in the previous publication. The sensors are positioned in close proximity

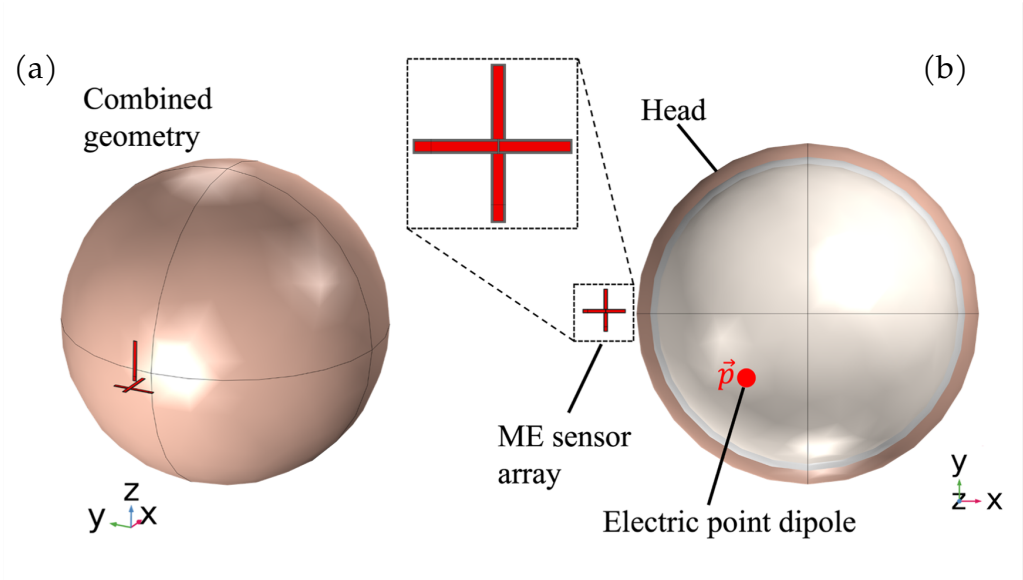

Figure 3.2 – An illustration of (a) the simplified head geometry with the 3-sensor array adjacent to it and (b) a cross-section of the human head in the x-y-plane showing the three tissue types of skin, skull, and white matter, from outermost to innermost. The white matter domain also contains an electric current point dipole source acting as the excitation mechanism by inducing a magnetic field through current flow inside the tissue (from [69], licensed under Creative Commons Attribution license CC BY 4.0, https://creativecommons.org/licenses/by/4.0/).

to each other and oriented in x-, y-, and z-direction, respectively. This orientation of the sensors serves the purpose of investigating directional dependencies of ME sensors, i.e., how the sensor response depends on the orientation of the sensor relative to direction and position of the magnetic field source. In addition to the array of three ME sensors, a novelty in this paper is the excitation mechanism, which consists of a simplified three-shell head model containing an electric current point dipole inside of its innermost layer. The layers, from outermost to innermost, are skin, skull, and white matter. Figure 3.2 gives an overview of the utilized ME sensor array and simplified human head geometries.

The aim of this study is to investigate the influence of the head geometry and the tissue layers' material properties on the induction and propagation of a magnetic field outside of the head, through the air environment, and into the sensor array. Based on the dipole's position and orientation, as well as the position of the sensor array and direction of each individual sensor, the sensors' responses for varying array positions in front of the head are evaluated. Additionally, the field propagation in the same head geometry with its material parameters set to those of air is investigated and compared to the case with tissue parameters, highlighting specificity and accuracy gains in using a combined sensor and head model with realistic material parameters [69].

In order to achieve accurate results for the behavior of the three orthogonal sensors, their directional sensitivity and the source dipole orientation must be taken into account. Therefore, the constitutive material equations described in Section 3.1

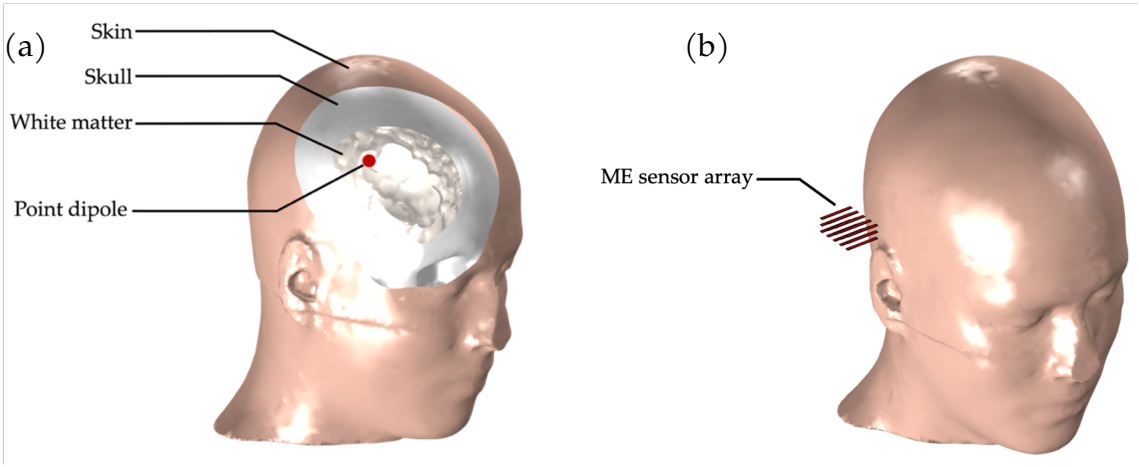

Figure 3.3 – (a) An illustration of the anatomically detailed human head model with its tissue compartments of skin, skull, and white matter, as well as the electric current point dipole source located inside the white matter volume. (b) View of the head geometry with adjacent ME sensor array, positioned to detect the magnetic field induced by the current flow inside the tissue and propagating outwards through the surrounding air environment (from [39], licensed under Creative Commons Attribution license CC BY 4.0, https://creativecommons.org/licenses/by/4.0/).

are adjusted by rotating the elasticity and coupling tensors for the magnetostrictive and piezoelectric layers according to each sensor's orientation [69].

Setting up this combination of ME sensor array and simplified human head model not only yields novel insights and contributions to the field of research, but also sets the foundation upon which to further develop this concept of a multi-scale model. The next publication is able to build on the fundamental ideas and lessons learned from this paper by introducing an array with a significantly larger number of sensors and, additionally, evolve the head model from a simple three-shell geometry to an anatomically detailed, MRI-based head model.

3.2.3 Combined ME Sensor Array and MRI-Based Human Head Model

The third publication, *Özden et al.* (2024) [39], further develops and extends both fundamental concepts of the previous work. Firstly, it introduces an array of now up to 15 ME sensors that are simulated simultaneously. Secondly, it improves the head model from a simple three-shell model to an anatomically detailed head based on human MRI data. Figure 3.3 (a) depicts a clipped model of the head with its three tissue compartments of skin, skull, and white matter, as well as an electric current point dipole located in the white matter section of the head. Figure 3.3 (b) depicts the combined ME sensor array and realistic human head model geometry reported in this publication, with the array of 15 ME sensors located adjacent to the surface of the skin at the right-hand side of the head.

This work aims to investigate the behavior of the 15-sensor array based on a dipole source located inside of the anatomically detailed human head. The dipole in-

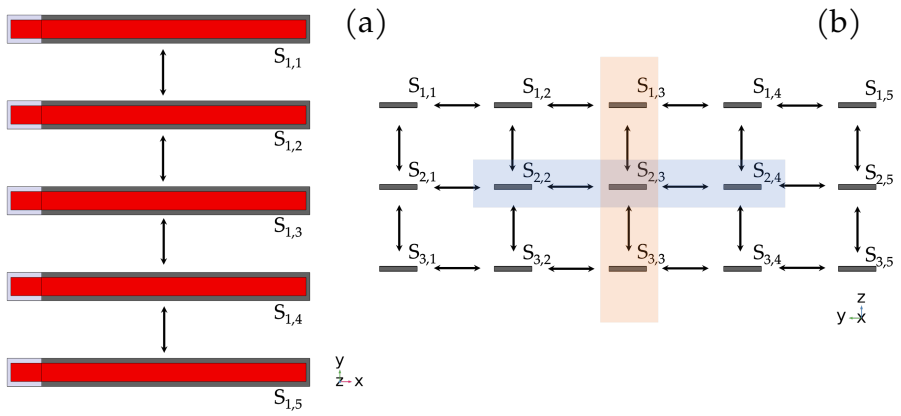

Figure 3.4 – (a) Top-down and (b) frontal view (on fixed end) of the 15-sensor array. Between each adjacent sensor is a variable distance between 1 mm and 5 cm. This figure shows equidistant sensor placement with 5 mm between the neighbors in both vertical and horizontal direction. The variable distance allows investigating the magnetic crosstalk between sensors and analyze the influence of the magnetostrictive layers on nearby ME sensors. The blue rectangle in (b) highlights the 3-sensor configuration for the horizontal sensor array, the red rectangle the vertical array which are included inside the full 15-sensor array configuration (from [39], licensed under Creative Commons Attribution license CC BY 4.0, https://creativecommons.org/licenses/by/4.0/).

duces a magnetic field inside the head structure, which propagates outwards, through the air environment, and into the ME sensor array. An important consideration for this study is the effect of crosstalk between adjacent ME sensors. Due to the high permeability of the magnetostrictive layer, localized distortions of the magnetic field can be caused around each individual ME sensor, potentially affecting the excitation field of adjacent sensors. Depending on the position within the array, distance to neighboring sensors, as well as the position relative to the source, the behavior of ME sensors could vary significantly. The sensors are positioned in a rectangular grid with three rows of five sensor columns each and variable distances between the sensors ranging from 0.1 mm up to 5 cm in vertical and horizontal direction, simultaneously. Figure 3.4 illustrates one such array configuration with the distance between neighboring sensors set to 5 mm in vertical and horizontal directions. The array of 15 ME sensors also contains subsets of 3-sensor arrays in horizontal configuration (sensors $S_{2,2}$, $S_{2,3}$, $S_{2,4}$; highlighted in blue) and vertical configuration (sensors $S_{1,3}$, $S_{2,3}$, $S_{3,3}$; highlighted in red) which were previously used for preliminary investigations before calculating the behavior of the full array, as depicted in Figure 3.4 (b).

A qualitative overview for preliminary simulations with the horizontal and vertical 3-sensor array configurations is shown in Figure 3.5. It depicts the magnetic flux density norm inside the MS layer, as well as the direction of the flux density vector around the adjacent sensors inside of the air environment. The figure illustrates the distortion of magnetic flux and its concentration towards the highly permeable magnetostrictive layer geometry. For both the horizontal (a)–(b) and vertical (c)–(d) configurations, the magnetic flux density norm inside the central sensor is slightly lower relative to the outer sensors, which makes the presence of

crosstalk effects apparent.

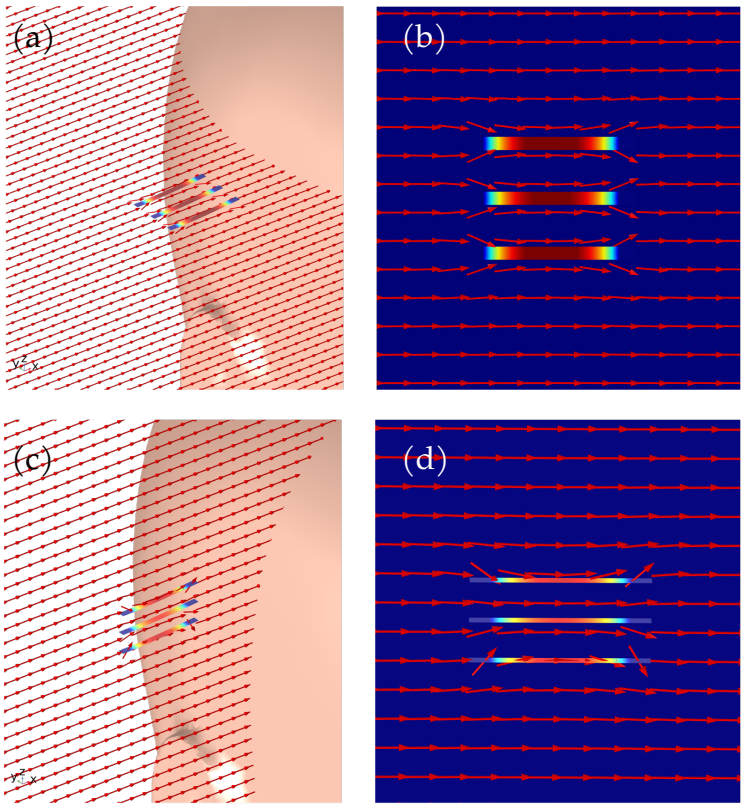

Figure 3.5 – An array of three horizontal (a)–(b) and vertical (c)–(d) ME sensors located to the side of the human head. The three sensors depicted here are located in the center of the extended 15-sensor array ($S_{1,3}$, $S_{2,3}$, $S_{3,3}$, for the vertical setup and $S_{2,2}$, $S_{2,3}$, $S_{2,4}$, for the horizontal case). Preliminary studies were performed with only 3 sensors in order to observe differences in the magnitude of crosstalk effects between horizontally and vertically adjacent sensors in the full 15-sensor array. This qualitative overview of the magnetic flux density norm inside of the magnetostrictive layer of each sensor and within the air environment illustrates the distortion of magnetic flux and its concentration towards the sensor geometry. The figure also indicates a slightly lower magnetic flux density norm inside the central sensor relative to the outer sensors in both variants.

To perform a detailed investigation of the crosstalk effects between adjacent sensors, the simulations are performed with a variable distance between the neighboring sensors in the vertical and horizontal direction. At a set distance from the head, the distance between the sensors is varied in several steps from 0.1 mm to 50 mm for the 3-sensor array. Due to computational requirements of a very fine mesh between sensors, the minimum distance between neighbors in the 15-sensor model had to be increased to 5 mm. An exemplary configuration of this distance sweep with 3 sensors is depicted in Figure 3.6, where the different distances between adjacent sensors and the resulting distortion of the magnetic flux density are illustrated. It shows the color-coded magnetic flux density norm and the x- and y-components of the magnetic flux density vector in the sensors and the surrounding air environment. The sensor array is located at a distance of approximately 15 mm from the surface of the head and the individual sensors are

at a distance from each other of (a) 0.1 mm, (b) 1 mm, (c) 5 mm, (d) 10 mm, (e) 20 mm, (f) 50 mm.

Following this brief overview of the main simulation models utilized in this research work, the next three chapters contain the complete published first author journal articles contributing to this dissertation.

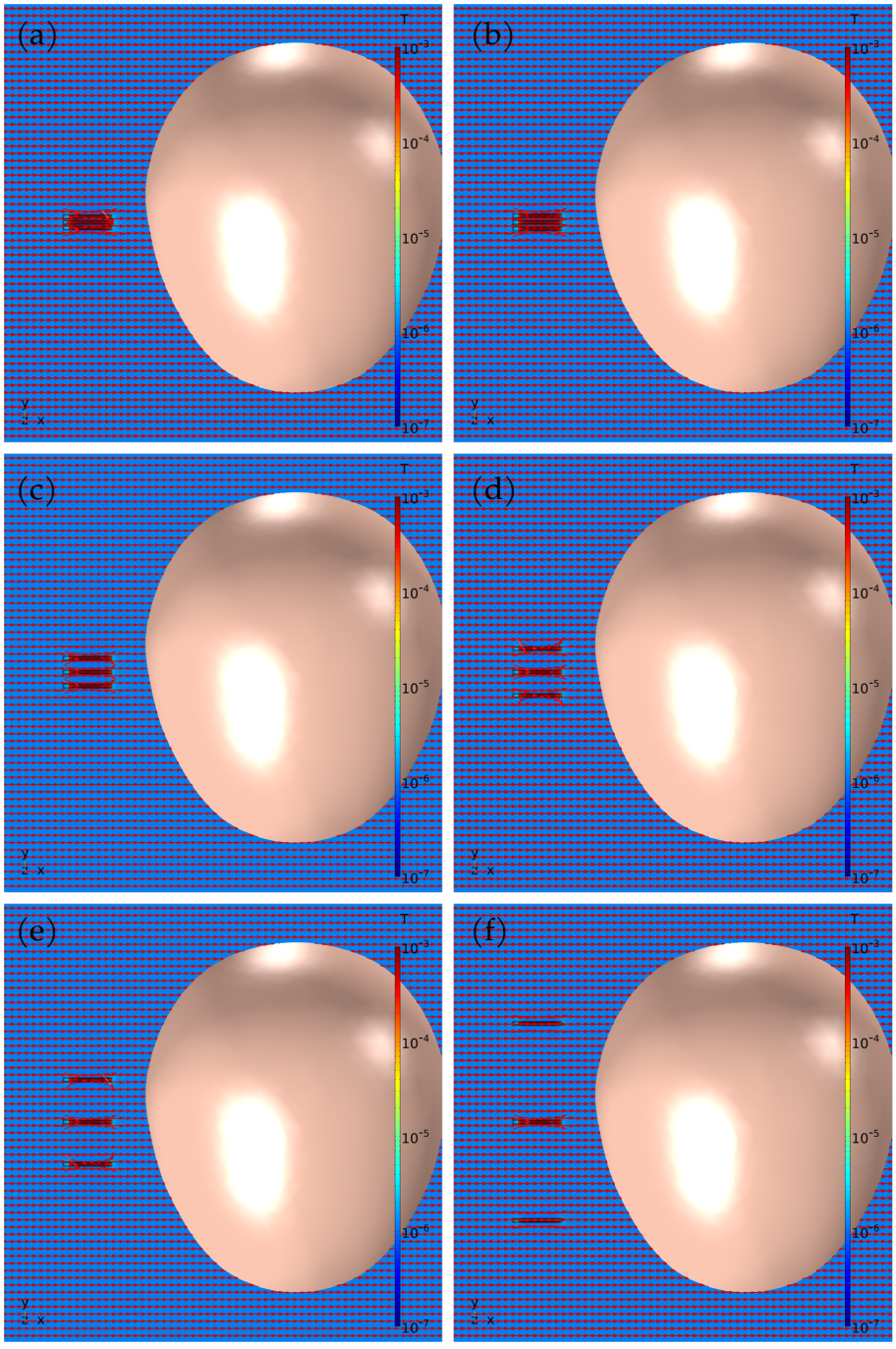

Figure 3.6 – The 3-sensor array in horizontal configuration next to the head model in top-view. Shown are the color-coded magnetic flux density norm and the x- and y-components of the magnetic flux density vector in the sensors and the surrounding air environment. The sensor array is located at a distance of approximately 15 mm from the surface of the head at its right-hand side and the individual sensors are at a distance from each other of (a) 0.1 mm, (b) 1 mm, (c) 5 mm, (d) 10 mm, (e) 20 mm, (f) 50 mm.

Chapter 4

Magnetoelectric Cantilever Sensors Under Inhomogeneous Magnetic Field Excitation

4.1 Published Article

Reference: *Mesut-Ömür Özden, Alexander Teplyuk, Ömer Gümüs, Dirk Meyners, Michael Höft, and Martina Gerken. "Magnetoelectric cantilever sensors under inhomogeneous magnetic field excitation". AIP Advances 10, 025132, pp. 025132-1–025132-6, 2020, doi:10.1063/1.5136239.*

Statement about own contribution:

For this work I established the modeling concept and performed preliminary simulations together with Ömer Gümüs in the scope of his bachelor's thesis as his advisor. I further developed the FEM model and conducted the simulations for the paper. The measurement was conducted by Alexander Teplyuk. Lastly, I evaluated the results and wrote the manuscript.

Conceptualization	Planning	Implementation	Manuscript preparation
High	High	Shared	High

AIP Advances ARTICLE scitation.org/journal/adv

Magnetoelectric cantilever sensors under inhomogeneous magnetic field excitation

Cite as: AIP Advances 10, 025132 (2020); doi: 10.1063/1.5136239
Submitted: 11 November 2019 • Accepted: 4 February 2020 •
Published Online: 20 February 2020

Mesut-Ömür Özden,[1,a] Alexander Teplyuk,[1] Ömer Gümüs,[1] Dirk Meyners,[2] Michael Höft,[1] and Martina Gerken[1]

AFFILIATIONS

[1] Faculty of Engineering, Institute of Electrical Engineering and Information Technology, Kiel University, Kaiserstraße 2, 24143 Kiel, Germany

[2] Faculty of Engineering, Institute for Materials Science, Kiel University, Kaiserstraße 2, 24143 Kiel, Germany

[a] Author to whom correspondence should be addressed: omoz@tf.uni-kiel.de

ABSTRACT

The behavior of strain-coupled composite magnetoelectric cantilever sensors under excitation with an inhomogeneous magnetic field is investigated. We consider a local excitation generated by a ring-shaped copper coil with one winding, variably positioned around the sensor. 3D finite-element-method simulations of the sensitivity along the longitudinal sensor axis are conducted and compared to the experimental results. The investigated sensor consists of a 2 μm thick magnetostrictive layer [$(Fe_{90}Co_{10})_{78}Si_{12}B_{10}$] and a 2 μm thick AlN piezoelectric layer on the opposite sides of a 350 μm thick silicon cantilever of 26.25 mm length and 2.45 mm width. The sensitivity along the sensor axis is investigated for three different frequencies—one below the resonance frequency, one at resonance, and one above resonance. A rich position-dependent sensitivity behavior is observed in simulations and experiments with a maximum sensitivity at ~4 mm from the fixed end of the cantilever for all three frequencies. Below and at the resonance frequency, a monotonously decreasing sensitivity is observed toward the free end of the cantilever. For the frequency above resonance, we observe a position of zero sensitivity at ~17 mm from the fixed end and a subsequent second maximum of sensitivity. We attribute the zero sensitivity to the destructive interference of local excitation and resonance effects.

Different sensor concepts and measurement principles for the detection of biomagnetic fields have been introduced in the literature. Among these concepts are sensors based on the giant magnetoresistive (GMR) effect, giant magnetoimpedance (GMI) effect, Hall effect, and spin-valve for use in magnetic particle imaging.[1–5] Detection of labeled samples such as biomolecules and cells[1–5] and label-free detection[6,7] are discussed extensively in previous publications. *Grimes et al.*[7] and *Kurlyandskaya et al.*[6] presented devices for label-free detection utilizing the distinct material properties of FeCoSiB (Metglas) and the frequency-dependent sensitivity behavior of their respective devices. *Brückl et al.*[8] described applications of magnetoresistive devices other than sensing, such as read heads in hard disk drives or magnetic random-access memory (MRAM) devices, and discussed their potential applications as logic elements or biochips. *Uchiyama et al.*[9] and *Mohri et al.*[10] presented their work on magnetoimpedance sensors based on amorphous wires. These sensors demonstrate pico-tesla resolution and the capability of performing biomagnetic measurements without magnetic shielding at room temperature. Here, we consider strain-coupled composite magnetoelectric (ME) cantilever sensors, which allow for uncooled and unshielded magnetic-field sensing with a limit of detection in the low $\boldsymbol{pT/\sqrt{Hz}}$ range.[11–19] ME sensors are based on the mechanical coupling between a magnetostrictive material layer and a piezoelectric material layer. In cantilever-type ME sensors operated in the resonant bending mode, the magnetostrictive layer causes deformation in the magnetic field. This deformation is converted into an induced electric potential by a piezoelectric layer, which, in turn, can be read out electrically. This measurement principle allows the sensor to be operated passively, as opposed to requiring, e.g., a pulse generation circuit feeding current into the device.[9,10] Past research has focused on the characterization of ME sensors in homogeneous magnetic fields. Here, we investigate for practical applications the

AIP Advances ARTICLE scitation.org/journal/adv

highly relevant case of ME cantilever sensors under inhomogeneous magnetic field excitation.

As ME sensors typically have a size on the order of a few millimeters, they cannot be regarded as point sensors for many biomagnetic measurements of interest. Therefore, there is a need to analyze the local sensitivity of the sensor volume and to determine if different sections of the cantilever geometry exhibit different sensitivity characteristics. With this knowledge, a meaningful transfer function may be established and allowed for correct interpretation of measurement data. We present a theoretical and an experimental study of the sensitivity behavior of an ME sensor excited by a single-winding coil concentrically positioned to the longitudinal axis of the sensor. The theoretical investigation is based on the assumption that the simulation of the small-signal behavior of ME sensors is possible under the hypothesis of linearity for the material model at the working point. The following constitutive equations for the coupled system are employed:[20–25]

$$\boldsymbol{T} = \boldsymbol{c}^{EH}\boldsymbol{S} - \boldsymbol{e}^{t}\vec{E} - \boldsymbol{e}_{m}^{t}\vec{H}, \tag{1}$$

$$\vec{D} = \boldsymbol{e}\boldsymbol{S} + \boldsymbol{\varepsilon}^{S}\vec{E}, \tag{2}$$

$$\vec{B} = \boldsymbol{e}_{m}\boldsymbol{S} + \boldsymbol{\mu}^{S}\vec{H}, \tag{3}$$

where $\vec{E}$, $\vec{H}$ and $\vec{D}$, $\vec{B}$ are the vectors of the electric and magnetic fields and the electric and magnetic flux density. The coupling between piezoelectric, magnetostrictive, and mechanical behaviors is expressed by the stiffness $\boldsymbol{c}^{EH}$ and strain to electric field and strain to magnetic field coupling constants $\boldsymbol{e}$ and $\boldsymbol{e}_m$, respectively. $\boldsymbol{\mu}^S$ and $\boldsymbol{\varepsilon}^S$ describe the permittivity and permeability. The following equations [(4)–(6)] describe the system of partial differential equations (PDEs):

$$\nabla \cdot \boldsymbol{T} = -\rho\omega^{2}\vec{u}, \tag{4}$$

$$\nabla \cdot \vec{D} = 0, \tag{5}$$

$$\nabla \cdot \vec{B} = 0, \tag{6}$$

which is set up for the independent variables $\vec{u}$, V, and $\vec{A}$.[20] These variables are solved for in the simulation and describe the displacement vector, the electric potential, and the magnetic vector potential, respectively. The following equations [(7)–(9)] determine the relation between the material equations [(1)–(3)] and the PDEs [(4)–(6)] and enable calculating the mechanic, electric, and magnetic behavior of the sensor:

$$\mathbf{S} = \frac{1}{2}\left[(\nabla\vec{u})^{t} + \nabla\vec{u}\right], \tag{7}$$

$$\vec{E} = -\nabla V, \tag{8}$$

$$\vec{B} = \nabla \times \vec{A}. \tag{9}$$

Figure 1(a) illustrates the modeled cantilever ME sensor setup including a cross-sectional view in the inset to illustrate the three separate sensor layers. Table I gives the sensor geometry parameters. The sensor is a composite consisting of three distinct and ideally

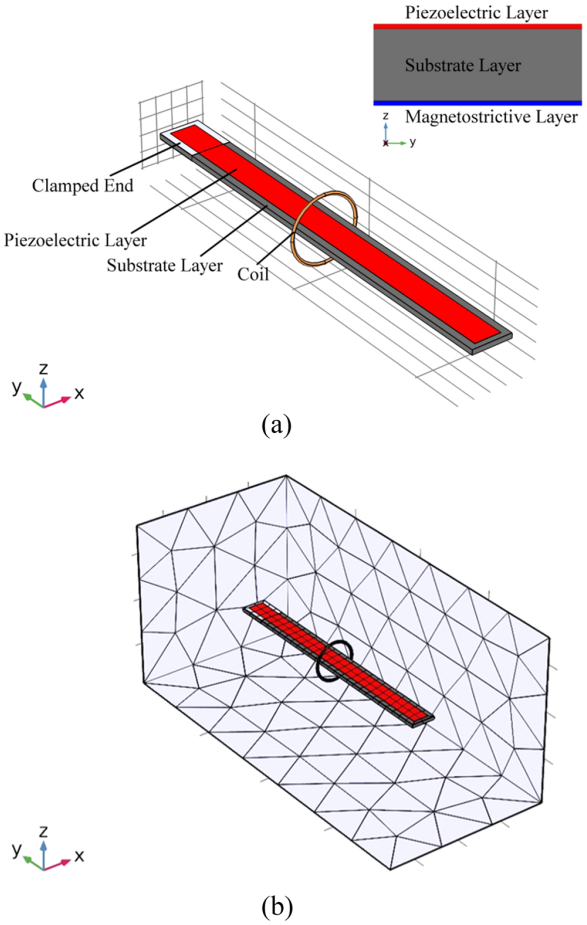

FIG. 1. (a) Geometry of the simulated cantilever ME sensor. The substrate layer (dark gray) with the piezoelectric material on top (red) is shown with the copper coil (brown) surrounding the geometry. The magnetostrictive layer is on the opposite side of the substrate, as seen in the inset illustrating a cross-sectional view of the device in the z-plane. (b) Mesh setup for the sensor, coil, and air box geometries. A finer, hexahedral mesh is chosen for the sensor layers, while the coil and the volume of the rectangular air box surrounding the sensor are meshed with coarser tetrahedral elements in order to reduce computational load. The dimensions of the simulation space shown are defined by the air box of size (W × D × H) 17.5 mm × 39.375 mm × 17.5 mm, and the dimensions of the sensor are listed in Table I.

interfaced layers without slip. These layers are the substrate layer, piezoelectric layer, and magnetostrictive layer. The copper coil has a major radius of 2.0 mm and a minor radius of 0.1 mm. The excitation current used in the simulations is 100 mA with a magnetic flux density of 30 μT in the center of the coil in free space (as a linear model is assumed, this is only relevant for interpreting the absolute numbers). The sensor geometry including the coil is placed inside a rectangular air box of size (W × D × H) 17.5 mm × 39.375 mm × 17.5 mm indicated by the meshed boundaries surrounding the cantilever in Fig. 1(b). This volume is assumed to be filled with

AIP Advances ARTICLE scitation.org/journal/adv

TABLE I. Layer geometry and materials of the investigated ME sensor.

Layer	Free length (mm)	Width (mm)	Height experiment (μm)	Height simulation (μm)	Material
Substrate	23.25	2.45	350.00	300.00	Silicon
Piezoelectric	22.92	1.60	2.00	20.00	Aluminum nitride
Magnetostrictive	22.90	1.80	2.00	20.00	$(Fe_{90}Co_{10})_{78}Si_{12}B_{10}$
Bottom electrode	22.70	1.80	1.00	...	Chrome-gold
Top electrode	7.50	1.40	1.00	...	Chrome-gold

air and serves the purpose of being a well-defined and controlled environment to apply numerical boundary conditions and investigate the disturbance of the applied magnetic field caused by the high permeability of the magnetostrictive material in air environment.[20] The sensor behavior is calculated numerically with three-dimensional (3D) finite-element method (FEM) simulations. These simulations are implemented in a commercial software (*COMSOL Multiphysics 5.4* with *solid mechanics*, *magnetic fields*, and *electrostatics* physics). For increased computation speed and to prevent meshing problems due to the high aspect ratio, we increased the active layer thicknesses to 20 μm. To approximately compensate for this active layer increase, the substrate thickness is decreased to 300 μm. The materials and their respective parameters were taken directly from the built-in material library in *COMSOL Multiphysics 5.4*, with modified Young's modulus (150 GPa) and Poisson's ratio (0.3) of the magnetostrictive layer according to previous measurements.[16,25] The bottom surface of the piezoelectric layer is grounded. The induced electric potential at the top surface is calculated for different excitation coil positions and different frequencies. There are no additional electrode layers or materials defined in the model. The utilized mesh is a combination of a fine hexahedral mesh with higher resolution for the sensor layers and a coarser, tetrahedral mesh with lower resolution for the remaining geometry of the coil and air box.

The ME sensor used in the measurements is a magnetoelectric composite fabricated by bulk-micromachining. A 350 μm thick and double-side polished silicon wafer is used as a substrate. This wafer thickness is based on the available standard silicon wafers in manufacturing and has a direct influence on the resonance frequency. While the resonance frequency can be tuned for specific applications and frequency ranges by using frequency conversion, this concept is not a focus of this work.[26,27] At the piezoelectric phase, the layer stack Ta 20/Pt 150/AlN 2000/Cr 20/Au 100 [thicknesses in nm] is deposited on one side of the substrate. A pulsed-DC sputter deposition method is applied for the AlN deposition.[28] The magnetostrictive phase is a 2 μm thick magnetostrictive layer $[(Fe_{90}Co_{10})_{78}Si_{12}B_{10}]$ deposited by magnetron sputtering on a 20 nm Ta seed layer on the other side of the substrate. Structuring of electrodes and functional layers is conducted by a combination of dry and wet etching techniques. Using a wafer dicing saw, ME

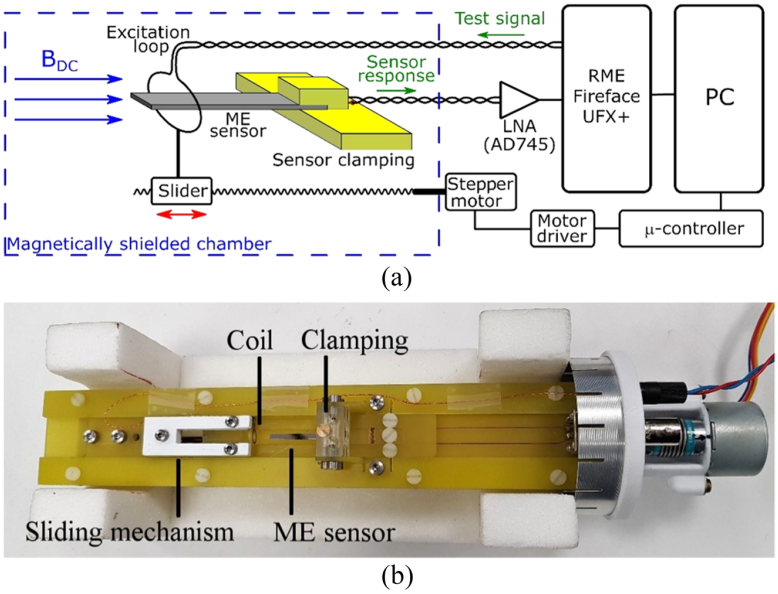

FIG. 2. (a) Configuration of the measurement setup for the cantilever ME sensor includes a sensor holder with an excitation loop driven by a stepper motor, low noise amplifier, A/D converter (RME Fireface UFX+), stepper motor driver with a micro-controller, magnetically shielded box, and PC. (b) The custom-made sensor holder setup consists of a clamping mechanism to fix the cantilever and a sliding mechanism connected to a stepper motor to adjust the position of the excitation loop along the sensor longitudinal axis.

AIP Advances ARTICLE scitation.org/journal/adv

cantilevers are fabricated. The lateral dimensions of the sensor are given in Table I. The substrate and piezoelectric layers are 2.9 mm long for clamping. The magnetostrictive layer is shorter than the other layers and does not extend to the clamping area. A post-deposition annealing is performed at 250 °C in the presence of a magnetic field H_{anneal} = 2000 Oe in order to align the unidirectional magnetic anisotropy perpendicular to the long cantilever axis.

The experimental characterization setup is shown in Fig. 2. It includes the sensor holder assembly with clamping and sliding mechanisms for fixing the cantilever and moving the excitation loop along the sensor. The slider is moved by the stepping motor, which is controlled by using a microcontroller and a motor driver. Due to the physical limitation of the measurement setup, only coil positions between 1.7 mm and 29.0 mm distances from the fixed end are measured. During the measurement, the sensor holder is located in a small magnetically shielded chamber (the magnetic noise level at 824 Hz is less than 100 fT) to avoid the influence of the magnetic interference. The required magnetic DC field (B_{DC} = 0.34 mT) is generated by a DC coil (not shown) for biasing the ME sensor. The test signals in the form of a one second long fixed-frequency sine wave coming from the professional sound card (RME Fireface UFX+) generate the local AC field inside the excitation loop fixed on the slider. The sensor signals are amplified by the low noise amplifier AD745 and digitalized by the analog-to-digital converter of the sound card for further signal processing, consisting of fast Fourier transform for filtering out the wanted frequency component in the sensor response.

Figure 3 shows the simulation and experimental results. For the simulated data, the averaged and normalized electric potential on the surface of the piezoelectric layer without any other additional circuitry is plotted. The averaging occurs since the entire geometry of this layer acts as the top electrode of the device and our model does not consider separate electrode geometries. Additionally, this potential is normalized in order to provide comparability to the measurement data due to significant differences in absolute amplitude, which are introduced by the measurement setup. For the measured data, the normalized magnetoelectric voltage (including amplifiers and loss mechanisms) is given. In simulations, the cantilever has an eigenfrequency of 848 Hz for the first mode. Experimentally, a resonance frequency of 824 Hz is observed. In both simulations and experiments, 600 Hz and 1200 Hz were chosen as frequencies below and above resonance for the study. The first important result observed in both simulations and experiments is the highly position-dependent and frequency-dependent sensitivity of the ME sensor. Both give similar results, showing the same distinctive sensitivity behavior. Both show a maximum sensitivity close to the fixed end of the cantilever. In the simulations, the maximum is approximately at a distance of 3.7 mm from the coil to the fixed end, while it is at 4.8 mm distance from the clamping in the measured data. The voltage decreases as the coil moves toward the fixed or free end. If the frequency is well above resonance at 1200 Hz, a different behavior is observed. There is a maximum voltage at the same coil position; however, with the increase in the distance of approximately 16 mm between the coil position and fixed end, the voltage decreases to a value of approximately zero due to phase change and superposition effects.[29] This superposition effect is the combined result of a local deformation of the magnetostrictive material and local induced electric potential based on the coil position and an

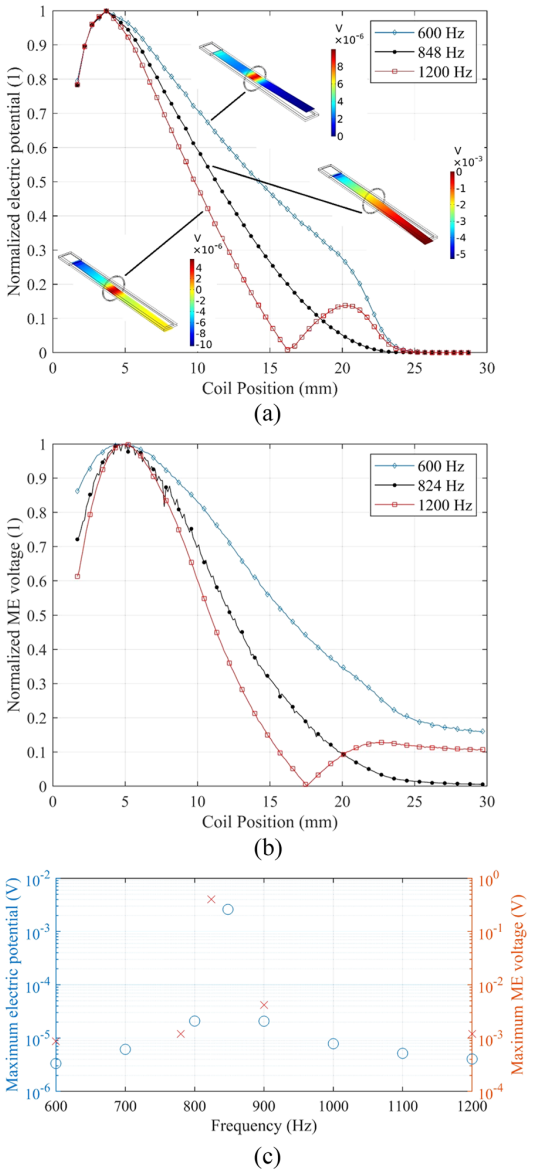

FIG. 3. (a) Averaged and normalized mean electric potential on the surface of the piezoelectric layer from simulations as a function of the coil position along the longitudinal sensor axis. The maximum induced potential is observed for positioning the excitation coil at ~3.7 mm from the fixed end for all frequencies. The insets show the induced electric potential distribution at the surface of the piezoelectric layer without a top electrode at the fixed coil position of 10.07 mm for all three excitation frequencies. (b) Normalized ME voltage from measurements as a function of the coil position. The maximum induced potential is observed for positioning the excitation coil at ~4.8 mm from the fixed end. (Note that there are 225 measurement points; for clarity, a reduced number of markers is shown on the graphs.) (c) Simulated maximum mean electric potential on the surface of the piezoelectric layer (blue) and measured maximum ME voltage (red) as a function of the excitation frequency.

AIP Advances ARTICLE scitation.org/journal/adv

induced electric potential due to the global vibration of the cantilever. Furthermore, increasing the distance results in an increased potential, leading to a secondary maximum, and again a drop as the coil position approaches the free end of the cantilever. This behavior is attributed to a destructive interference effect of local excitation and resonance effects. The insets in Fig. 3(a) further illustrate the differences in the local potential along the surface of the piezoelectric layer for the three excitation frequencies, as well as the phase change upon passing the resonance frequency.

The slight differences in the resonance frequency and position of the maximum may be attributed to the thicker active layers in the simulation as well as the imperfect clamping of the sensor in the experiment with a metal clamp locked by screws. Simulated and measured data are in good agreement for the range between 3 mm and 20 mm coil positions, while the curves show a discrepancy at both ends of the cantilever for frequencies that are below or above the resonance frequency. This behavior can be explained by the difference between the maximum and minimum signal values. While in resonance, the sensitivity of the cantilever is increased greatly;[23,30,31] at frequencies that are not close to the resonance frequency, the sensitivity and, thus, the generated signal are significantly lower. In this interval, the measured data are simply a noise effect that is strong enough to be visible in the normalized voltage curves' off resonance, but too low for a significant contribution for the resonant voltage curve. The voltage curve for the resonant case in Fig. 3(b) exhibits measurement noise over the entire range of coil positions. However, the effect is small compared to the measured signal amplitude and does not fundamentally change the behavior of the sensor. Due to the limited number of measurements possible with the unique sensor, a statistical error evaluation was not conducted.

Figure 3(c) illustrates the simulated absolute values for the maximum mean electric potential on the surface of the piezoelectric layer and maximum ME voltages obtained by measurement as functions of different excitation frequencies. The maximum value in this scenario is obtained by comparing each possible excitation coil position for the given frequency. For the simulated sensor, a distinct peak of ~2.6 mV maximum mean potential is observed at the resonance frequency of 848 Hz, dropping to ~3.3 μV at 600 Hz and ~4.0 μV at 1200 Hz. Here, the peak ME voltage of ~401 mV occurs at a resonance frequency of 824 Hz, with drops to ~0.9 mV at 600 Hz and ~1.2 mV at 1200 Hz. This behavior is due to the effect of increased sensitivity at resonance.[11]

In conclusion, we have demonstrated that cantilever magnetoelectric sensors exhibit a highly position-dependent sensitivity for operation on resonance. This is in addition to previously analyzed direction-dependent sensitivity.[3] Therefore, a detailed setup of the transfer function of a magnetoelectric sensor is necessary for applications with inhomogeneous excitation fields. If a simple point-sensor approximation is desired, our results show that the most sensitive point is located close to the fixed end of the cantilever. Therefore, this point should be taken as the point of the measurement value. In addition, for operation off resonance, additional interference effects are observed that need further investigation for operation in this frequency regime. The presented insights allow more precise modeling and measurements in the future, as opposed to assuming that the highest sensitivity is in the center of the sensor.

Funding by the German Research Foundation (Deutsche Forschungsgemeinschaft DFG) through the Collaborative Research Center SFB 1261 "Magnetoelectric Sensors: From Composite Materials to Biomagnetic Diagnostics" is gratefully acknowledged.

APPENDIX: MATERIAL PARAMETERS

The material parameters used in this sensor model are obtained from experimental studies and listed in Refs. 20 and 30. In addition to the values from the literature, the following modifications were made for Metglas based on in-house estimations and experimental results:

$$\nu_{Metglas} = 0.3, \tag{A1}$$

$$E_{Metglas} = 150 \times 10^{9}\ \text{Pa}, \tag{A2}$$

$$\mu_{Metglas} = 1569 \times 10^{-6}\ \text{H/m}, \tag{A3}$$

$$\varepsilon_{Metglas} = 8.854 \times 10^{-6}\ \text{H/m}. \tag{A4}$$

For aluminum nitride, the material parameters in the simulations contain the following adjustment:

$$\rho_{\text{AlN}} = 3300\ \text{kg/m}^3. \tag{A5}$$

For silicon, following values are modified:

$$\nu_{Si} = 0.28, \tag{A6}$$

$$E_{Si} = 170 \times 10^{9}\ \text{Pa}, \tag{A7}$$

$$\varepsilon_{Si} = 104 \times 10^{-12}\ \text{F/m}. \tag{A8}$$

The remaining material parameters used are identical to the parameters given in Ref. 20.

REFERENCES

[1] D. R. Baselt, G. U. Lee, M. Natesan, S. W. Metzger, P. E. Sheehan, and R. J. Colton, "A biosensor based on magnetoresistance technology. 1. This paper was awarded the biosensors and bioelectronics award for the most original contribution to the Congress.1," Biosens. Bioelectron. **13**(7–8), 731–739 (1998).
[2] P. A. Besse, G. Boero, M. Demierre, V. Pott, and R. Popovic, "Detection of a single magnetic microbead using a miniaturized silicon Hall sensor," Appl. Phys. Lett. **80**(22), 4199–4201 (2002).
[3] F. Blanc-Béguin, S. Nabily, J. Gieraltowski, A. Turzo, S. Querellou, and P. Y. Salaun, "Cytotoxicity and GMI bio-sensor detection of maghemite nanoparticles internalized into cells," J. Magn. Magn. Mater. **321**(3), 192–197 (2009).
[4] M. M. Miller, G. A. Prinz, S. F. Cheng, and S. Bounnak, "Detection of a micron-sized magnetic sphere using a ring-shaped anisotropic magnetoresistance-based sensor: A model for a magnetoresistance-based biosensor," Appl. Phys. Lett. **81**(12), 2211–2213 (2002).
[5] H. A. Ferreira, D. L. Graham, P. P. Freitas, and J. M. S. Cabral, "Biodetection using magnetically labeled biomolecules and arrays of spin valve sensors (invited)," J. Appl. Phys. **93**(10), 7281–7286 (2003).
[6] G. V. Kurlyandskaya, V. Fal Miyar, A. Saad, E. Asua, and J. Rodriguez, "Giant magnetoimpedance: A label-free option for surface effect monitoring," J. Appl. Phys. **101**(5), 054505 (2007).
[7] C. A. Grimes *et al.*, "Wireless magnetoelastic resonance sensors: A critical review," Sensors **2**(7), 294–313 (2002).
[8] H. Brückl *et al.*, "Magnetoresistive logic and biochip," J. Magn. Magn. Mater. **282**(1–3), 219–224 (2004).

[9]T. Uchiyama, K. Mohri, Y. Honkura, and L. V. Panina, "Recent advances of pico-tesla resolution magneto-impedance sensor based on amorphous wire CMOS IC MI sensor," IEEE Trans. Magn. **48**(11), 3833–3839 (2012).
[10]K. Mohri, T. Uchiyama, L. V. Panina, M. Yamamoto, and K. Bushida, "Recent advances of amorphous wire CMOS IC magneto-impedance sensors: Innovative high-performance micromagnetic sensor chip," J. Sens. **2015**, 1.
[11]C. Kirchhof *et al.*, "Giant magnetoelectric effect in vacuum," Appl. Phys. Lett. **102**(23), 232905 (2013).
[12]D. Viehland, M. Wuttig, J. McCord, and E. Quandt, "Magnetoelectric magnetic field sensors," MRS Bull. **43**(11), 834–840 (2018).
[13]A. Kittmann *et al.*, "Wide band low noise love wave magnetic field sensor system," Sci. Rep. **8**(1), 278 (2018).
[14]R. Jahns *et al.*, "Giant magnetoelectric effect in thin-film composites," J. Am. Ceram. Soc. **96**(6), 1673–1681 (2013).
[15]T. Nan, Y. Hui, M. Rinaldi, and N. X. Sun, "Self-biased 215 MHz magnetoelectric NEMS resonator for ultra-sensitive DC magnetic field detection," Sci. Rep. **3**, 1985 (2013).
[16]P. Zhao *et al.*, "Fabrication and characterization of all-thin-film magnetoelectric sensors," Appl. Phys. Lett. **94**(24), 10–13 (2009).
[17]R. Jahns *et al.*, "Microelectromechanical magnetic field sensor based on ΔE effect," Appl. Phys. Lett. **105**(5), 052414 (2014).
[18]S. Zabel, C. Kirchhof, E. Yarar, D. Meyners, E. Quandt, and F. Faupel, "Phase modulated magnetoelectric delta-E effect sensor for sub-nano tesla magnetic fields," Appl. Phys. Lett. **107**(15), 152402 (2015).
[19]B. Spetzler *et al.*, "Influence of the quality factor on the signal to noise ratio of magnetoelectric sensors based on the delta-E effect," Appl. Phys. Lett. **114**(18), 183504 (2019).
[20]J. L. Gugat, J. Schmalz, M. C. Krantz, and M. Gerken, "Magnetic flux concentration effects in cantilever magnetoelectric sensors," IEEE Trans. Magn. **52**(5), 1–8 (2016).
[21]J. L. Gugat, M. C. Krantz, J. Schmalz, and M. Gerken, "Signal-to-noise ratio in cantilever magnetoelectric sensors," IEEE Trans. Magn. **52**(9), 1–5 (2016).
[22]J. F. Blackburn, M. Vopsaroiu, and M. G. Cain, "Verified finite element simulation of multiferroic structures: Solutions for conducting and insulating systems," J. Appl. Phys. **104**(7), 074104 (2008).
[23]M. Guo and S. Dong, "A resonance-bending mode magnetoelectric-coupling equivalent circuit," IEEE Trans. Ultrason., Ferroelectr. Freq. Control **56**(11), 2578 (2009).
[24]V. M. Petrov, G. Srinivasan, M. I. Bichurin, and T. A. Galkina, "Theory of magnetoelectric effect for bending modes in magnetostrictive-piezoelectric bilayers," J. Appl. Phys. **105**(6), 063911 (2009).
[25]D. Hasanyan *et al.*, "Theoretical and experimental investigation of magnetoelectric effect for bending-tension coupled modes in magnetostrictive-piezoelectric layered composites," J. Appl. Phys. **112**(1), 013908 (2012).
[26]R. Jahns, H. Greve, E. Woltermann, E. Quandt, and R. Knöchel, "Sensitivity enhancement of magnetoelectric sensors through frequency-conversion," Sens. Actuators, A **183**, 16–21 (2012).
[27]P. Hayes *et al.*, "Electrically modulated magnetoelectric sensors," Appl. Phys. Lett. **108**(18), 182902 (2016).
[28]E. Yarar, V. Hrkac, C. Zamponi, A. Piorra, L. Kienle, and E. Quandt, "Low temperature aluminum nitride thin films for sensory applications," AIP Adv. **6**(7), 075115 (2016).
[29]M. Gerken, "Resonance line shape, strain and electric potential distributions of composite magnetoelectric sensors," AIP Adv. **3**(6), 062115 (2013).
[30]I. Bichurin, A. Filippov, M. Petrov, M. Laletsin, N. Paddubnaya, and G. Srinivasan, "Resonance magnetoelectric effects in layered magnetostrictive-piezoelectric composites," Phys. Rev. B **68**(13), 132408 (2003).
[31]S. Dong, J. Cheng, J. F. Li, and D. Viehland, "Enhanced magnetoelectric effects in laminate composites of terfenol-D/Pb(Zr, Ti)O_3 under resonant drive," Appl. Phys. Lett. **83**(23), 4812 (2003).

4.2 Key Findings and Scientific Implications

- ME-sensors exhibit a highly position-dependent sensitivity for operation at the investigated frequencies at, below, and above the resonance frequency. This applies for the demonstrated highly localized and inhomogeneous magnetic excitation field applied to the device.
- Additional interference effects are observed at frequencies off-resonance, which require further investigation if the sensor is utilized above or below resonance.
- For a simple point-sensor approximation (e.g., in localization algorithms), a position near the clamped end should be chosen in calculations and algorithms assuming a point of maximum sensitivity relative to the source location, based on the demonstrated results.
- The new insights resulting from this work allow for more precise models and algorithms for detection and localization applications, which previously assumed the maximum sensitivity in the geometric center of the ME sensor.
- Theoretical and experimental results are in good agreement regarding the sensitivity behavior of the sensor.
- Further theoretical investigations and validation through experimental measurements with inhomogeneous excitation fields are recommended to study the ME sensor response.

Chapter 5

A Combined Magnetoelectric Sensor and Human Head Model for Biomagnetic FEM Simulations

5.1 Published Article

Reference: *Mesut-Ömür Özden, Julius Schmalz, and Martina Gerken. "A Combined Magnetoelectric Sensor and Human Head Model for Biomagnetic FEM Simulation". IEEE Sensors Journal, vol. 23, no. 24, pp. 30259–30270, 2023, doi:10.1109/JSEN.2023.3329579.*

Statement about own contribution:

For this work I developed the modeling concept, set up the FEM model, and conducted the simulations. Furthermore, I evaluated the results and wrote the manuscript.

Conceptualization	Planning	Implementation	Manuscript preparation
High	High	High	High

IEEE Sensors Council IEEE SENSORS JOURNAL, VOL. 23, NO. 24, 15 DECEMBER 2023 30259

A Combined Magnetoelectric Sensor and Human Head Model for Biomagnetic FEM Simulations

Mesut-Ömür Özden, Julius Schmalz, and Martina Gerken, *Senior Member, IEEE*

***Abstract*—We investigate a coupled multiscale 3-D finite-element model consisting of an orthogonal array of thin-film cantilever magnetoelectric (ME) magnetic field sensors and a simplified human head model. Electric point dipole sources are placed inside the head to generate an electromagnetic field. This field propagates through the tissue layers and outside of the head, where it reaches the sensor array. The investigated sensors are based on a 300-μm-thick silicon substrate layer of 26.25 mm length and 2.45 mm width, with a 20-μm-thick aluminum nitride (AlN) layer and a 20-μm-thick FeCoSiB layer as piezoelectric (PE) and magnetostrictive materials, respectively, located on opposite sides of the substrate. We position three sensors orthogonally to obtain a vector field sensor. The head model is based on the three-shell approach and consists of concentric spheres representing white matter, skull, and skin. All three layers are assigned specific conductivity and relative permittivity values from the literature, aiming to approximate the propagation of electromagnetic fields through different tissue types. We observe the propagation of an electric field generated by the dipole source and subsequent induction of a magnetic field inside the head structure, propagating outwards to the sensor array, where the generated voltage in the PE layer is evaluated for different ME sensor array and source positions and orientations. We show different behaviors of the sensors for a dipole source inside the head tissue versus a simple air environment, highlighting the benefits in accuracy and specificity of a combined head and sensor model with realistic material parameters.**

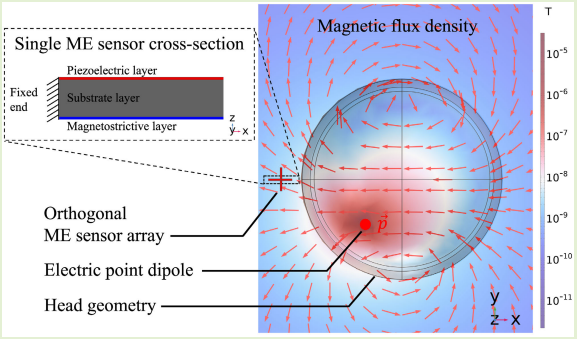

***Index Terms*— Biomagnetic sensing, finite-element method (FEM), human head model, magnetic field measurement, magnetoelectric (ME) effects, magnetostrictive (MS) device, multiferroic, multiscale model.**

I. Introduction

MEASURING biomagnetic signals, such as in magnetocardiography (MCG), magnetoencephalography (MEG), or magnetomyography (MMG) applications, has become increasingly important in medical diagnostics and patient care. Researchers have demonstrated several viable approaches to measure biomagnetic fields, such as fluxgate sensors [1], [2], optically pumped magnetometers (OPMs) [3], or superconducting quantum interference device (SQUID)-based sensor systems [4]. While each of these technologies has its own unique operation principle, each one also has specific drawbacks, such as the limitation of SQUID-based systems to require cooling with liquid helium or limitations of OPM sensors to be sensitive to ambient background magnetic fields. In this work, we consider strain-coupled composite magnetoelectric (ME) magnetic field sensors as a promising technology for conducting such measurements in clinical environments. As opposed to existing measurement systems such as OPMs, fluxgate sensors, or SQUID-based sensor systems, ME sensors offer highly sensitive measurements of biomagnetic fields in the pT/Hz$^{1/2}$ range, while enabling passive, uncooled, and unshielded operation [5], [6]. Recent investigations characterized resonant ME sensor systems with a signal-to-noise ratio of -90 dB, an application-specific capacity of 9.8×10^{-7} dB·Hz, and a limit-of-detection of 22 pT, while the inherent noise for the sensor itself (i.e., without readout electronics) is given as $\approx$4 pT/$\sqrt{\text{Hz}}$ at 7.684 kHz at room temperature [6]. Research into ME devices also includes studies with devices such as novel ME antennas that can be used for energy harvesting and magnetic field sensing purposes simultaneously, including energy harvesting experiments on mice brain tissue and simu-

Manuscript received 29 September 2023; accepted 25 October 2023. Date of publication 8 November 2023; date of current version 14 December 2023. This work was supported by the German Research Foundation (Deutsche Forschungsgemeinschaft, DFG) through the Collaborative Research Center (CRC) 1261 "Magnetoelectric Sensors: From Composite Materials to Biomagnetic Diagnostics." The associate editor coordinating the review of this article and approving it for publication was Prof. Kai Wu. *(Corresponding author: Mesut-Ömür Özden.)*

The authors are with the Chair for Integrated Systems and Photonics, Department of Electrical and Information Engineering, Kiel University, 24143 Kiel, Germany (e-mail: omoz@tf.uni-kiel.de; jusc@tf.uni-kiel.de; mge@tf.uni-kiel.de).

Digital Object Identifier 10.1109/JSEN.2023.3329579

lation of the magnetic field and tissue interactions [7]. Experts in the mathematical and medical fields have been studying the relationship between electric sources inside the human brain and the resulting electric potential on the scalp for many years. This article has led to numerous important findings and the development of highly detailed and precise so-called electroencephalography (EEG) forward models. Publications in this field cover many regions of interest, such as the efficient computation of EEG forward models [8], the effects of forward model errors on EEG source localization [9], or improved forward head models for specific applications such as ear-EEG [10]. Although this work uses a simplified three-shell approach for the head geometry, which is already well-known in the literature regarding the EEG forward problem, the novel approach we present here is to include a fully coupled ME sensor model in combination with the simplified head model. With this strategy, we can focus on the behavior of ME sensors in the presence of a head model with reduced complexity that is less computationally taxing and offers readily available literature for validation, while the combined model retains the potential to be increased in complexity for further investigations, e.g., with realistic MRI data. While, in past studies, the performance characterization of ME sensors has often been conducted under simplified homogeneous magnetic field excitation, this work focuses on investigating sensor behavior under the influence of inhomogeneous magnetic fields in order to more accurately model sensor behavior in application-oriented scenarios. Our theoretical investigation is based on the approach of 3-D finite-element method (FEM) simulations and introduces a combined simplified three-shell human head and an array of three orthogonal ME sensors in a single FEM model [11], [12], [13]. The ME sensor array is positioned inside an air volume surrounding the human head, which in turn contains one or multiple electric point dipole sources. Depending on the position and orientation of the point dipole inside the head, a different magnetic field propagation through the head tissue and the surrounding air volume is observed and propagates outwards and into the ME sensors. Previous studies show strong directionality of the sensor response depending on incident angle of the magnetic field relative to the cantilever's long axis [14], [15], [16]. By using this approach, we can calculate the inhomogeneous magnetic flux reaching the sensors and the subsequent electric sensor response based on the interaction of one or multiple electric sources inside of the biological tissue, the propagation of fields through the tissue, and surrounding air environment. This novel approach of a combined model offers new insights into the behavior of ME sensors, but it also requires a careful modeling setup due to the difficulties of combining very small structures, such as the sensor's 20-μm-thin layers, with comparatively large geometries such as the head. We will describe this work in detail in the following sections. In Section II, we will give a detailed overview of the methodology used in our FEM simulation models. This section will first illustrate the ME sensor model and the head model separately and then describe the combined sensor and head model. Relevant material and geometry parameters, as well as equations for the FEM calculations, are also given. Section III covers the results of our investigation. These include the electric and magnetic fields created inside the head domain and the surrounding air environment, as well as the sensor response to the propagation of the magnetic field outwards from the head into the sensor array. We conclude our findings in Section IV, emphasizing the benefits of using a combined ME sensor and head model with realistic material parameters.

II. Methodology

We implement the joint model and calculate the sensor behavior with 3-D FEM simulations utilizing the commercial software COMSOL Multiphysics 6.1 including the physics packages solid mechanics, magnetic fields, and electrostatics. We perform the simulations with the frequency-domain study and an excitation frequency of 848 Hz, corresponding to the cantilever sensor's previously established resonance frequency for operation in direct detection mode [13]. Sections II-A–II-C will briefly describe the modeling process from the separate models used for the ME sensors and the human head, leading to the setup for our combined sensor and head model. The complexity of this combined model gave rise to some difficulties that we encountered during the stages of our investigation. We will also use this section to describe the problems that these difficulties lead to, as well as the simplifications and solution strategies that were necessary to achieve reliable results.

A. ME Sensor Model

Each of the three modeled ME sensors consists of three materials: the substrate layer, magnetostrictive (MS) layer, and piezoelectric (PE) layer. These layers form a composite with slipless and ideal interfaces. The coupled system is described in detail in previous works based on the constitutive equations given in [17], [18], [19], [20], [21], and [22], while this work utilizes the built-in physics interfaces of COMSOL Multiphysics. The solid mechanics interface governs the mechanical behavior of our model and is used to solve the equations of motions together with a constitutive model for solid materials. The following equations define the mechanical behavior of our model:

$$-\rho\omega^2\boldsymbol{u} = \nabla \cdot S \tag{1}$$

$$S = \boldsymbol{C} : \varepsilon \tag{2}$$

$$\varepsilon = \frac{1}{2}\left[(\nabla\boldsymbol{u})^{\mathrm{T}} + \nabla\boldsymbol{u}\right] \tag{3}$$

$$\boldsymbol{C} = \boldsymbol{C}(E, \nu). \tag{4}$$

In the linear elastic material node, S and ε stand for the stress and strain, respectively, $\boldsymbol{u}$ is the displacement vector, ω is the angular frequency, and ρ is the density. $\boldsymbol{C}$ describes the coupling between stress and strain for the silicon substrate and is a function of its Young modulus and Poisson's ratio. The MS material node contains the relation between stress, strain, magnetic field, and magnetic flux density in the stress-magnetization form

$$S = c_{\mathrm{H}} : \varepsilon - \boldsymbol{H} \cdot e_{\mathrm{HS}} \tag{5}$$

$$\boldsymbol{B} = \mu_{0,\mathrm{vac}}\mu_{\mathrm{rS}}\boldsymbol{H} + e_{\mathrm{HS}} : \varepsilon. \tag{6}$$

Here, c_H and e_{HS} are the elasticity matrix and coupling matrix (Voigt notation), respectively, $\boldsymbol{B}$ and $\boldsymbol{H}$ are the magnetic field and magnetic flux density, respectively, and μ_{rS} is the relative permeability. The PE material node of our model includes equations determining the coupling between the mechanical and electric properties of the sensors

$$\nabla \cdot \boldsymbol{D} = \rho_v \tag{7}$$

$$S = c_E : \varepsilon - \boldsymbol{E} \cdot e_{ES} \tag{8}$$

$$\boldsymbol{D} = \varepsilon_{0,vac}\varepsilon_{rS}\boldsymbol{E} + e_{ES} : \varepsilon. \tag{9}$$

$\boldsymbol{D}$ is the electric displacement field and ρ_v is the volume charge density according to Gauss's law. c_E and e_{ES} denote the elasticity matrix and coupling matrix (Voigt notation) in the stress-charge form, respectively. $\boldsymbol{E}$ and ε_{rS} represent the electric field and the relative permittivity, respectively. In conjunction with solid mechanics described in (1)–(9), our model utilizes the interfaces of magnetic fields and electrostatics. While the first interface uses Maxwell's equations to primarily solve for the vector potential with (10)–(12), the latter utilizes Gauss' law and solves for the electric potential related to (13) and (14)

$$\nabla \times \boldsymbol{H} = \sigma \boldsymbol{E} + j\omega \boldsymbol{D} \tag{10}$$

$$\boldsymbol{B} = \nabla \times \boldsymbol{A} \tag{11}$$

$$\boldsymbol{E} = -j\omega \boldsymbol{A} \tag{12}$$

$$\boldsymbol{E} = -\nabla V \tag{13}$$

$$\boldsymbol{D} = \varepsilon_0 \boldsymbol{E} + \boldsymbol{P}. \tag{14}$$

Here, σ refers to the specific conductivity, $\boldsymbol{A}$ is the magnetic vector potential, V is the electric potential, and $\boldsymbol{P}$ is the polarization. Equations (10)–(14) combined with the mechanical interrelations in (1)–(9) allow us to simulate MS and PE coupling and enable us to model the physical effects that govern the functioning principle of ME sensors. Fig. 1(a) shows a schematic of a single ME sensor. The cantilever structure's substrate layer has a total length of 26.25 mm, out of which 3 mm consists of a fixed structure to enable resonant bending modes along the long axis in a fixed-free setup. The width of the substrate layer is 2.45 mm and its thickness is 0.3 mm. The red layer on the top of the substrate illustrates the PE layer with a length of 25.6 mm, width of 1.6 mm, and thickness of 20 μm. On the opposite side of the substrate, the MS layer is located with a length of 22.9 mm, width of 1.8 mm, and thickness of 20 μm. Fig. 1(b) illustrates the array consisting of three orthogonal ME sensors. Fig. 1(c) shows a cross section of the sensor with the layer thicknesses to scale. The geometry of this sensor is based on a fabricated ME sensor, which was computationally and experimentally characterized in [13]. Lastly, we illustrate moving from previous studies based on homogeneous magnetic excitation fields in Fig. 1(d) toward ME sensors in inhomogeneous magnetic fields, such as those propagating outwards from a source inside the human head depicted in Fig. 1(e). Due to the strong directionality of the sensor and the definition of the materials parameters in our setup, the elasticity and coupling tensors for the PE and MS layers must be rotated according to the orientation of the respective cantilever in the coordinate system. We perform this tensor rotation within COMSOL Multiphysics by defining additional base vector systems and assigning the MS and PE properties of each sensor to the corresponding coordinate system, based on the sensor's orientation in the modeling space. The material parameters for the nonrotated base vector system (which corresponds to the sensor oriented in x-direction) are given in the Appendix and used to implement and compute the sensor behavior. The dimensions and material types of the sensors are given in Table I. The material used for the substrate layer is silicon. The PE layer consists of aluminum nitride (AlN) [17]. Lastly, the MS material of choice is the compound material FeCoSiB, commercially known as Metglas [17]. The sensor model does not consider any additional layers such as electrode layers.

TABLE I
LAYER GEOMETRY AND MATERIALS OF THE INVESTIGATED ME SENSOR

Layer	Length (mm)	Width (mm)	Height (μm)	Material
Substrate	26.25	2.45	300.00	Silicon
Piezoelectric	25.60	1.60	20.00	Aluminum Nitride
Magnetostrictive	22.90	1.80	20.00	Metglas

TABLE II
TISSUE TYPES OF THE HEAD WITH THEIR RESPECTIVE RADII AND ELECTRIC PARAMETERS ACCORDING TO THE LITERATURE

Tissue type	Radius (mm) [22]	Specific conductivity (S/m) [22], [23]	Relative permittivity [24]
White matter	88	0.43	30,000,000
Skull	92	0.05	40,000-1,000,000
Skin	100	1.0	1,200,000

B. Human Head Model

The implemented simplified head for this study is a basic three-shell head model [11], [12]. It consists of three concentric spheres of different radii representing the tissue types of the head: skin, skull, and white matter (from outermost to innermost sphere). Fig. 2 illustrates the layer structure of the head in a cross section of the xy plane. The three tissue types with their radii 88, 92, and 100 mm are assigned material parameters for their relative permittivity and specific conductivity according to the literature [23], [24], [25], with our white matter layer encompassing the geometry for separate cortex and fluid layers from other related investigations [23]. The relevant geometry parameters and electric properties of the head are given in Table II.

C. Combined Model

Following the individual design of the sensor model and head model, we combine both geometries in a joint model. The center of the head is placed in the origin of the coordinate

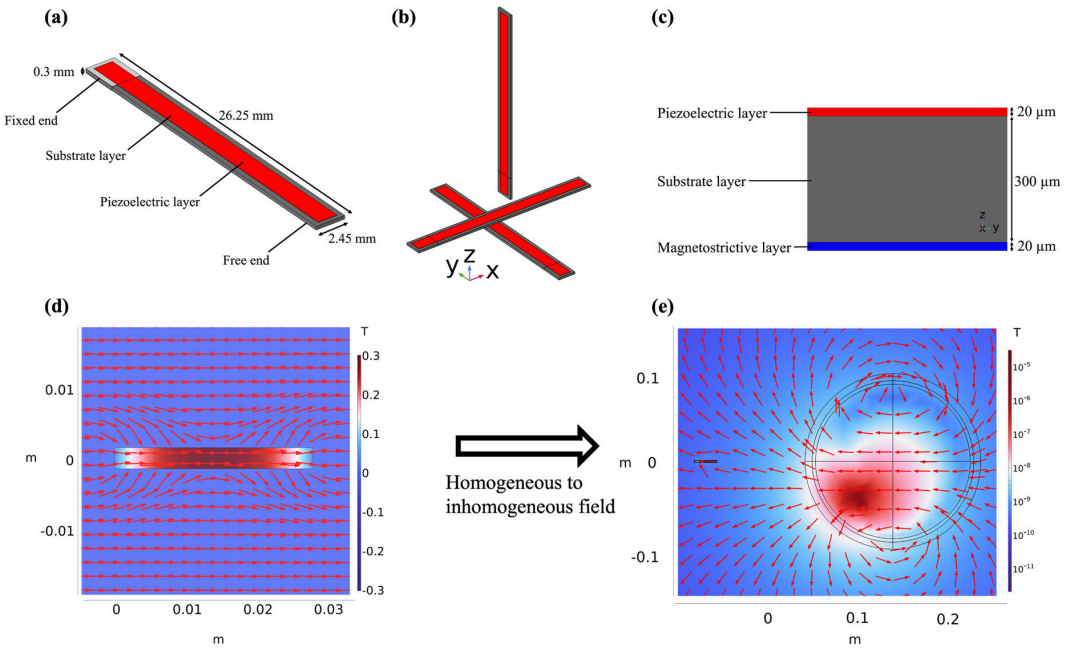

Fig. 1. (a) Schematic of a single ME sensor with given length, width, and thickness of the substrate layer (gray) and view of PE layer on the top surface of the substrate (red). (b) Sensor array with three orthogonal ME sensors oriented in *x*-, *y*-, and *z*-directions to form a vector sensor array. (c) Cross section of ME sensor with relative layer *z*-thicknesses to scale (but not the *y*-widths). Shown are the PE layer (red) on the top surface and the MS layer (blue) on the bottom surface of the substrate layer (gray). (d) Magnetic flux density norm and logarithmically scaled vector field for an ME sensor inside a homogeneous magnetic field parallel to the long axis of the sensor as an example for past investigations. (e) The aim of this work is to study the behavior of ME sensors inside inhomogeneous magnetic fields, such as those propagating outwards from a source inside of a human head, in a combined ME sensor and human head model.

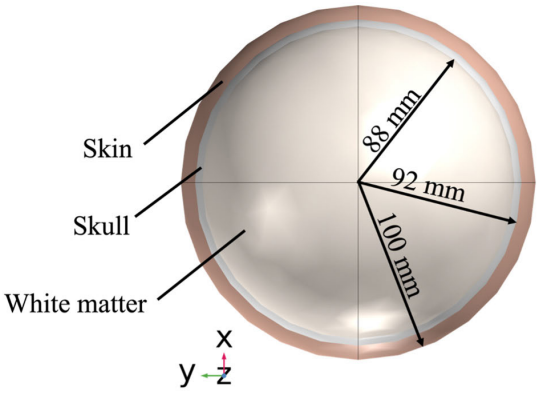

Fig. 2. Cross section of the simplified human head based on the three-shell model. Three tissue types are represented with concentric spheres: skin, skull, and white matter (from outermost to innermost sphere). The radii are 88 mm for the white matter layer, 92 mm for the skull layer, and 100 mm for the skin layer. The relative permittivity and specific conductivity are assigned to the tissue types according to the literature.

system, and the sensor array can be positioned at arbitrary locations around the head. This setup allows us to investigate the behavior of each of the three orthogonal sensors for different positions in space, relative to the source inside the head. Fig. 3(a) shows a cross section of the head model with its three tissue layers skin, skull, and white matter, as well as the ME sensor and an electric point dipole source located in the white matter domain. Fig. 3(a) illustrates the method of positioning the ME sensor in proximity of the head and calculating its response for various positions inside the air surrounding, e.g., performing a position sweep in the 3-D space around the head. The electric point dipole can be positioned at arbitrary locations inside the head geometry to study the effects of its position in the material frame on the propagation of electric and magnetic fields inside and outside of the head. It is also possible to have multiple active dipole sources, and the model is compatible with different source configurations altogether, e.g., deep brain stimulation (DBS) electrodes.

One of the challenges in combining both the sensor and head in a joint 3-D FEM model is that different geometries can have vastly different aspect ratios. While the simplified human head typically has a circumference in the cm-range, depending on the tissue compartment, the ME sensor's material layers have thicknesses in the μm-range, i.e., up to four orders of magnitude smaller. In order to calculate both relatively large and substantially smaller geometries in the same model, the 3-D mesh must be designed carefully. Therefore, the mesh elements constituting the head geometry are chosen to be small enough to achieve sufficiently accurate results, while avoiding sizes so small that they would lead to excessive computational load. Fig. 4(a)–(c) shows the mesh setup for the head, airbox, and ME sensor with their differently sized and structured tetrahedral mesh elements, respectively. The mesh is divided

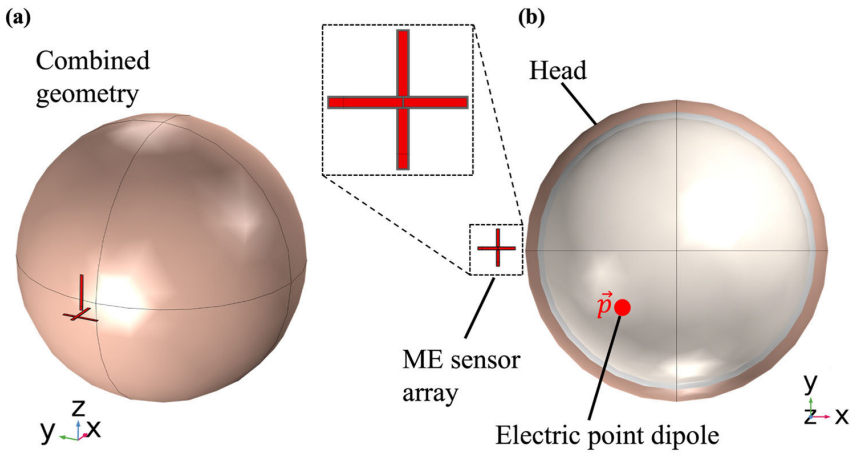

Fig. 3. (a) Overview of model geometry for the entire combined head and sensor model. A rectangular air surrounding (not depicted) contains the head model with its three tissue layers, as well as the sensor array with three orthogonally positioned sensors. (b) Cross section of the head model with adjacent ME sensor array. The concentric spheres represent human tissue layers of skin, skull, and white matter (innermost to outermost layer). Inside the head geometry, an electric dipole source can be placed at arbitrary positions and with variable excitation parameters, such as frequency and amplitude.

into three separate areas, with one area representing the head, one for the sensor array, and one for the air environment. The mesh for the sensor array has an extremely fine element size, where the head and airbox geometries have comparatively smaller amounts of mesh elements which are also larger in size and include a higher maximum element growth rate and slightly smaller resolution of narrow regions. With this setup, the volume between the head and sensor array can be very finely meshed in order to enable a progression from the head geometry to the much finer sensor geometry, while the sections of less interest further away from the head and sensor array can be meshed with much larger elements. The mesh always extends between the head and ME sensor array continuously through the surrounding air environment. Over the course of our mesh optimization, however, we achieved the best results using a physics-controlled mesh that was automatically generated by COMSOL Multiphysics and slightly adjusting mesh parameters maximum element size, minimum element size (i.e., longest edge of tetrahedral mesh element), and maximum element growth rate for specific regions. This way, we were able to optimize the mesh settings while keeping the computational load as low as possible. The number of degrees of freedom solved for is $\sim$19.4 $\times$ 10^6. Table III gives an overview of the mesh parameters used for different regions of the model. The surrounding air environment has the dimensions of ($W \times D \times H$) 65.63 $\times$ 65.63 $\times$ 65.63 cm (corresponding to 25-times substrate length) and is shown in Fig. 4(b). This size was determined through a parameter sweep and found to be a good compromise between computational efficiency and the effect of the boundary condition (magnetic isolation) of the air domain on the magnetic field inside of it. An essential numerical limitation of this combined model is the large range of values for certain material parameters, such as the specific conductivity value. While this value can be in the range of 1–0.05 S/m for the tissues of the head as stated in Table II, it is close to 0 S/m for the surrounding air. In FEM

TABLE III
MESH PARAMETERS USED FOR THE SENSOR, HEAD, AND SURROUNDING AIR ENVIRONMENT

Region	Head & airbox	Sensor (substrate)	Sensor (remaining)
Max. element size (m)	2E-2	1E-3	5e-4
Min. element size (m)	3E-4	1E-4	9e-5
Max. element growth rate	5	3	3
Resolution of narrow regions	2	3	3
Curvature factor	0.3	0.3	0.3

modeling, and specifically 3-D models, these high contrasts of material parameters can lead to numerical stability problems, potentially resulting in random high-amplitude maxima in the magnetic field propagating through the air environment or nonconverging solutions (this was confirmed by COMSOL) [26]. These instabilities also occurred in this work, and to combat these effects, we set the electrical conductivity of air to a much greater value, using 1 mS/m for the simulations in this work. We speak of this artificial medium as "high-conductivity air."

III. Results and Discussion

A. Electrical Excitation and Propagation of Electromagnetic Fields

To test functionality and stability, we compute several studies on electric and magnetic field propagation through the entire modeling domain and repeatedly validate results against a homogeneous high-conductivity air environment.

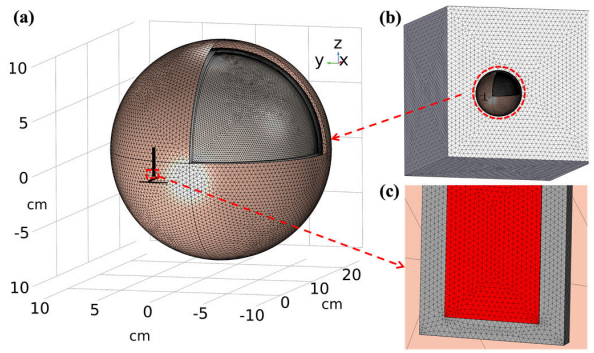

Fig. 4. Model geometry with overlaid mesh elements: (a) zoomed-in view of head geometry with the sensor array positioned in front of it and a cross section of the skin and skull tissue layers; (b) full scale of the head and sensor with the surrounding rectangular air volume. This air volume has the dimensions of ($W \times D \times H$) 65.63 × 65.63 × 65.63 cm; and (c) magnified view of the base of the ME sensor in z-orientation. A fine tetrahedral mesh is chosen for the sensor and its thin, high aspect ratio layer structure. The head and the surrounding air volume with their comparatively large structures and lower aspect ratios utilize a successively coarser tetrahedral mesh to reduce computational load. The dimensions of the sensor and head are listed in Tables I and II, respectively.

An electric point dipole is placed inside the head geometry with an arbitrary dipole direction and magnitude. Based on the electromagnetic coupling in the model, this dipole introduces an electric field and a current density inside the head geometry, leading to the creation and propagation of a magnetic field. Fig. 5 shows a comparison of the electric current density norm, electric field density norm, and magnetic flux density norm based on electromagnetic field propagation from a dipole source inside the head. As a validation step, Fig. 5(a)–(c) demonstrates the results for a case in which all three layers of the head have their material parameters set to those of high-conductivity air, while Fig. 5(d)–(f) shows the results with the material parameters for the head structure described in Table II. Fig. 5(a) and (d) illustrates the computed electric current density norm inside the head with an electric point dipole as the source. In this case, the electric point dipole is oriented in the y-direction and has a magnitude of 1 mA·m. For reference, a current amplitude of 1 mA at a standard tissue amplitude range is described as falling within the therapeutic range of DBS, and similar magnitudes within head models are described in [24] and [27]. Furthermore, magnetic flux density measurements with fluxgate magnetometers obtained magnitudes in the nT and pT ranges for monopolar and bipolar DBS stimulations, respectively, validating a range of excitation amplitudes for our calculations [28]. Due to the linear behavior, the simulated excitation source can be scaled in amplitude to investigate different excitation sources, such as various DBS electrode configurations or brain activity during epileptic seizures. The dipole is placed at distances of $x = y = -4$ cm and $z = +2$ cm from the center of the head geometry. To increase the numerical stability of the solution in setups with highly symmetrical source positions, an additional dipole source with the same direction and a magnitude of 1 μA·m was placed at coordinates $x = z = 0$ and $y = 1$ mm in the center of the white matter region. Furthermore, the logarithmically scaled arrows represent the current density norm vector inside different tissue types of the head. This illustrates how the current is guided by the shape of the head geometry and the tissue layers' conductivity and permittivity parameters. Because of the geometry- and material-based field propagation inside the head, the difference in propagation of the electric field density norm is apparent in Fig. 5(b) and (e), while the propagating magnetic flux density for the two cases can be compared in Fig. 5(c) and (f). The magnetic flux density is computed based on Ampere's law in the entire model domain and couples the electric field propagation with the material parameters and geometries to calculate the propagation of a magnetic field in the modeling space. The magnetic field that propagates through the high-conductivity air environment and ultimately reaches the sensor array dictates its behavior. Fig. 5 illustrate how the magnetic flux density is dependent on the head geometry through the electric material parameters, even though constant vacuum permeability for white matter, skull, and skin is assumed [6], [29].

B. Sensor Response and Array Behavior

After computing and analyzing the propagation of the magnetic field originating from the point dipole source through the head and high-conductivity air environment, we calculate the magnetic field arriving at the sensor array. The sensor's Metglas layer exhibits a deformation based on the MS effect, and via the mechanical coupling of the composite layers, a PE potential is generated between the AlN layer's top and bottom surfaces, which defines the sensor's electric output signal. The voltage between these surfaces is the transduced electric response for a given magnetic excitation field. The ME exhibits frequency- and angle-dependent responses regarding the incident external magnetic field. To visualize these dependencies within our combined sensor and head model, we performed a frequency sweep with varying excitation frequencies for the dipole inside the head and the full combined model. Fig. 6(a) shows the frequency characteristic for the sensor in the x-direction and excitation frequencies between 825 and 875 Hz. The blue line corresponds to the mean absolute potential generated over the PE layer of the sensor and shows a distinct peak at the first resonant bending mode at 848 Hz. The black line corresponds to the mean magnetic flux density norm inside the volume of the MS layer when this layer's material parameters are set to air. This configuration confirms that the magnetic flux density propagating through the air volume and into the sensor geometry is constant over the excitation frequencies and no frequency-dependent influence from the head's tissue layers is affecting the sensor's frequency characteristics. Important to note is that the sensor model in this work does not include damping effects due to sensor materials or the surrounding air volume. Previous investigations on damping effects reveal relevant contributors such as viscoelastic, molecular, and thermoelastic damping and compare sensor performance for air damping under atmospheric pressure and vacuum [30]. It is also possible to implement experimentally obtained quality factors in postprocessing of the simulation results and to prescribe arbitrary damping coefficients based

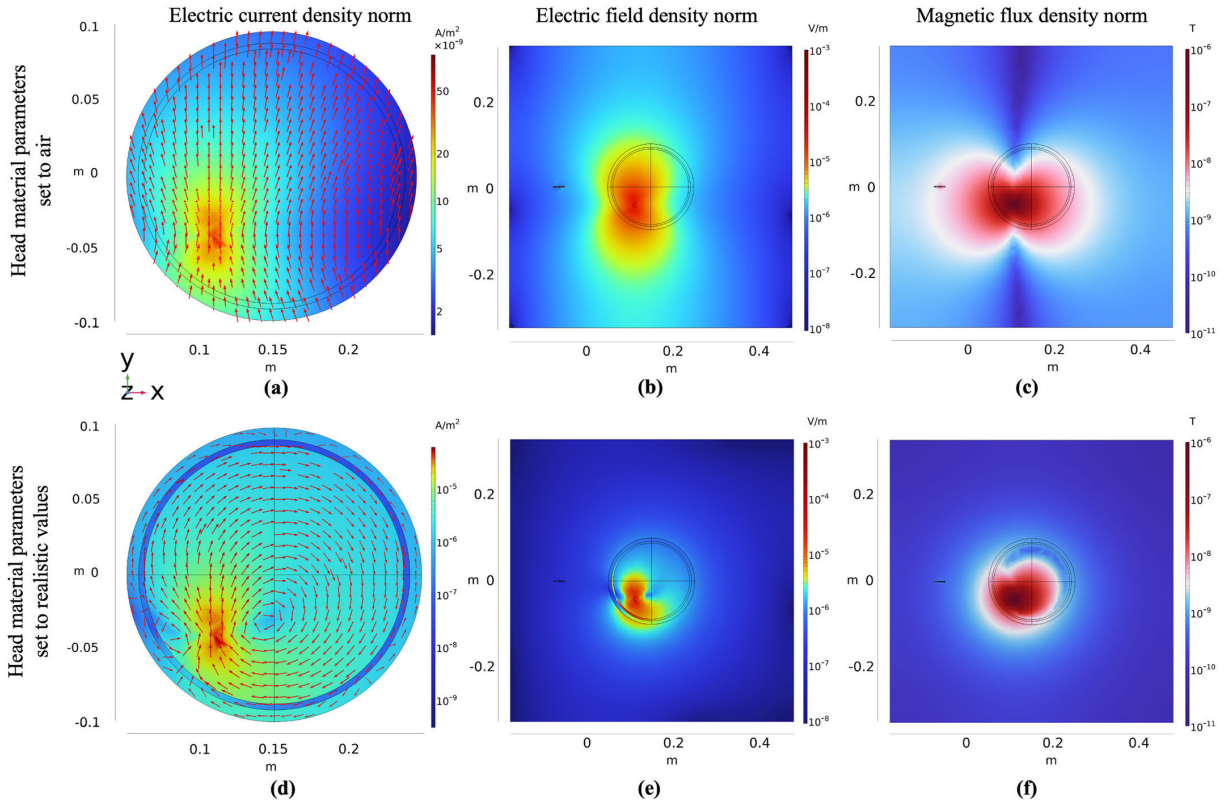

Fig. 5. Computed electric current density norm, electric field density norm, and magnetic flux density norm for an electric point dipole source at coordinates $x = y = -4$ cm and $z = +2$ cm in the white matter domain. The dipole moment is oriented in y-direction and has a magnitude of 1 mA·m. (a) and (d) Electric current density norm inside the head geometry for the head material parameters set to air with a conductivity of 1 mS/m and realistic tissue values, respectively. The red arrows represent logarithmically scaled current density vectors (tangential components) in the xy plane and illustrate that the current density is strongly dependent on head geometry and electric material properties. (b) and (e) Resulting electric field norm and (c) and (f) magnetic flux density norm inside and outside of the head. The figures highlight the dependence of the magnetic flux density on the head geometry through the electric material parameters.

on the Fano resonance profile of the sensor frequency characteristic. This enables dynamic investigations of different sensor damping configurations and calculating ME coefficients after running the FEM simulation [31], [32]. This work omits damping effects and calculating the ME coefficient, as our focus is to highlight the relative behavior of the ME sensors in the orthogonal array for different dipole orientations and positions and investigate the position adaptability of the magnetic field detection in highly inhomogeneous fields. In Fig. 6(b), we show the angular dependence of the normalized PE voltage of a single sensor in the x-direction obtained in a homogeneous magnetic field with varying angle of incidence relative to the x- (azimuthal angle) and z-axes (polar angle). We observe a strong sinusoidal dependence for both azimuthal and polar angles of incidence and a maximum sensor response for incident angles parallel to the long axis of the sensor in the x-direction. Computing the total magnetic flux density in the MS layer and the potential across the PE layer geometry can be performed for arbitrary combinations of dipole positions and orientations, as well as ME sensor positions around the head. Fig. 7 illustrates the previously discussed dipole setup and the electric behavior of the three orthogonal ME sensors for two different positions of the array relative to the source inside the head. Fig. 7(a) shows the tangential component of the magnetic flux density in the xy plane at the location of the MS layer for the sensor oriented in the y-direction at approximately 10 cm distance to the surface of the head. Red arrows (logarithmically scaled) illustrate the vector field of the magnetic flux density. The ME sensor array is positioned at $y = -4$ cm (position marked as "A"). Fig. 7(b) shows the same setup as in Fig. 7(a), but with the sensor array positioned at $y = +5$ cm (position marked as "B").

The plot of the magnetic flux density in the xy plane visualizes its inhomogeneity. Depending on their position along the y-axis, the sensors are exposed to different compositions of parallel and orthogonal magnetic flux vector components, relative to the long axis of the cantilever. As an example, we take a closer look at the sensor in y-direction. In cases of strongly orthogonal components, such as in position A, the sensor's MS layer exhibits low magnetic flux densities. At position B, the vector field has increasing parallel components leading to an enhanced magnetic flux density inside the MS layer, which ultimately leads to a stronger sensor response. This effect can be extended and analyzed for different sensor

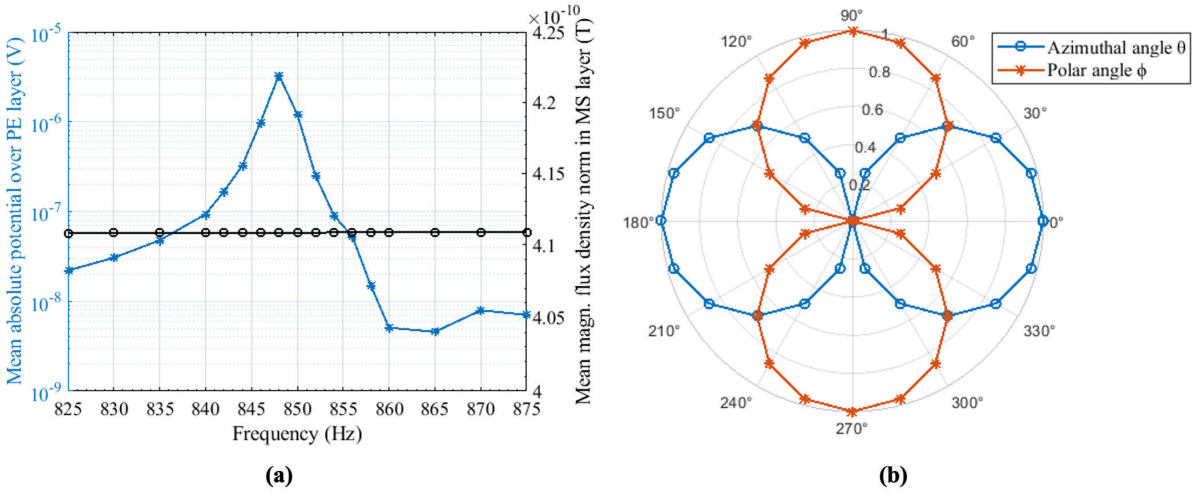

Fig. 6. (a) Frequency characteristics of the sensor oriented in x-direction. The blue line corresponds to the mean absolute potential over the PE layer generated at different frequencies with a maximum at the first resonant bending mode at 848 Hz. The black line illustrates the resulting mean magnetic flux density norm inside the volume of the MS layer of the sensor with material parameters set to air, demonstrating that no variation in magnetic flux occurs based on the magnetic field propagation through tissue and air at different frequencies. (b) Angular dependence of the normalized PE voltage for a sensor in the x-direction in a homogeneous magnetic excitation field of incident azimuthal angle θ and polar angle ϕ. A strong sinusoidal dependence is observed with maximum sensor response at incident field angles parallel to the sensor's long axis.

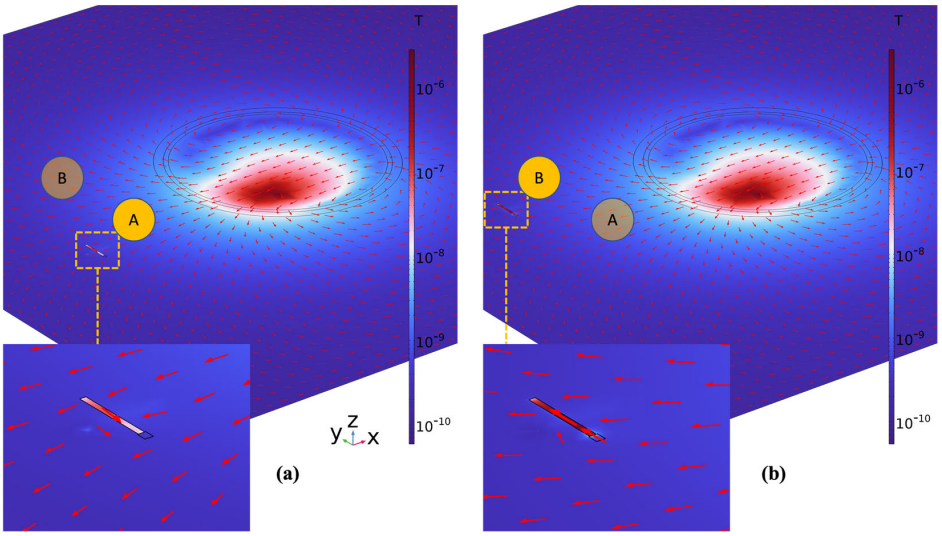

Fig. 7. Magnetic flux density norm and logarithmically scaled vector field (tangential component) for the excitation with an electric point dipole in y-orientation. Shown is the xy plane with a cross section through the head with a dipole source and the MS layer of the sensor in y-orientation. (a) Sensor is located at $y = -4$ cm on the y-axis, annotated by the position marker "A." The inset in (a) shows the magnetic vector field propagating orthogonally to the long axis of the sensor, resulting in a minimal magnetic flux density and therefore electric response of the sensor. (b) Sensor is located at $y = +5$ cm on the y-axis, annotated by the position marker "B." The inset in (b) shows the magnetic vector field propagating with a smaller angle relative to the long axis and therefore a larger parallel component. This leads to a higher magnetic flux density and therefore electric response of the sensor, compared to the case in (a).

locations and all sensors in the array, as shown in Fig. 8. Here, we demonstrate the strong location-dependent behavior of the three sensors, including the sensor in y-orientation (red line) with its minimum at $y = -4$ cm and maximum at $y = +5$ cm, corresponding to the respective locations "A" and "B" highlighted in Fig. 7. With increasing position in positive y-direction, this effect is counteracted by the growing distance to the dipole source. Note that the sensors in x- and z-orientations show similarly constant behavior as opposed to distinct extrema, while the latter exhibits the strongest magnetic flux density, due to the dominant z-component of the magnetic field in this dipole configuration (the arrows in Fig. 7 only depict the tangential component of the magnetic flux density to exemplary highlight the behavior of the sensor in the y-direction). The increased magnetic flux density leads to a higher PE potential in the PE layer

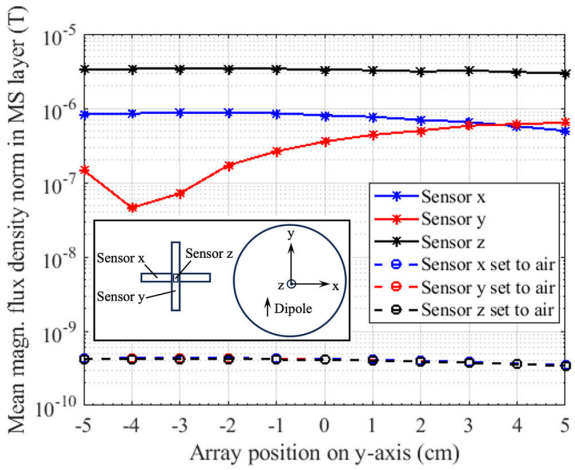

Fig. 8. Simulation results for integrated magnetic flux density in the MS layers for the ME sensor array and a dipole in y-orientation. The dipole is located at coordinates $x = y = -4$ cm and $z = +2$ cm in the white matter domain and oriented in the y-direction. The solid lines show the integrated magnetic flux density norm inside each individual sensor for the variable position of the sensor array on the y-axis. The dashed lines show the integrated magnetic flux density norm inside the air volume previously occupied by the sensor geometry, without any sensor material present. The graphs represent the directional behavior of the three orthogonal sensors based on their position in the magnetic vector field surrounding the head in the interval between $y = -5$ and $+5$ cm and the anisotropy of the PE and MS couplings.

through the ME effect and, ultimately, a stronger sensor response.

To verify that this effect is explained by the interaction of the sensors' behavior and the head model, as opposed to solely the propagation of the magnetic field through the head and air environment, we perform a validation step. We replace the entire sensor array geometry with the same volume of air and compute the magnetic flux density norm in the air volumes previously corresponding to the three MS layers. The results for these air volumes are displayed as the dotted lines in Fig. 8, whereas the magnetic flux density norm inside of the actual MS layers corresponds to the solid lines. These results confirm that all three air volumes, without any sensor material present, have near identical magnetic flux density norms, with the difference being slight distance variations to the source due to the orthogonal sensor positioning. In contrast to that, the simulations containing the sensor model with MS layers show distinct behavior based on the orientation of each sensor. We conclude that each of the three sensors is exposed to a very similar external magnetic field, but exhibits vastly different results based on its previously described directionally dependent behavior [14], [15], [16].

In order to perform another validation step to confirm the directional dependence of the ME sensors, as well as the dependence of the propagated magnetic field on the electric parameters of the head, we execute the same simulation with a variable y-position sweep of the sensor array (as shown in Fig. 8) in combination with setting the material parameters of the head structure to the properties of high-conductivity air [analogous to the setup described in Fig. 5(a)–(c)]. The resulting plots are shown in Fig. 9 where each of the three sensors is compared for both cases of the head material parameters set to tissue values according to Table II (solid lines) or high-conductivity air (dashed lines) for the setup with an electric point dipole source oriented in the y-direction and the integrated absolute potential over the PE layer is given for each array position. The behavior for the sensor in x-orientation is shown in Fig. 9(a) and is close in both cases, with a slightly higher potential generated for the case of the head geometry set to air material parameters. Fig. 9(b) shows the plot for the sensor oriented in y-direction. The influence of the material parameters of the tissue on the propagation of the magnetic field leads to the curves showing significant differences. In the case of the head geometry consisting of air, the sensor shows a steadily declining potential for the location sweep in a positive y-direction. In the case of the head geometry with assigned tissue parameters, the previously discussed behavior for the y-sensor becomes apparent again based on the effects of the electrical properties of the tissue on the magnetic field propagation. Due to the dominant z-component of the magnetic field, the integrated absolute potential over the PE layer is highest in Fig. 9(c) in both cases compared to the other sensors, with the dipole in the air environment generating a potential which is roughly one order of magnitude higher.

After the validation, a synoptic overview with all three sensors in the array combined with three different excitation dipole orientations is given in Fig. 10. Here, the effects on each orthogonal sensor for the dipole excitation with x-, y-, and z-orientations are given in Fig. 10(a)–(c), respectively. The different reactions of the sensors based on the dipole orientation are apparent, e.g., the minima for the sensors in x-, and y-orientations for different dipole moment directions, or the dominating potential of the sensor in z-direction in Fig. 10(a) and (b) compared to its near constant and minimal values in Fig. 10(c). We can pinpoint the differences in behavior seen in Fig. 10 on the strong anisotropy in the coupling parameters of the PE and MS layers. The materials' coupling is at its maximum when the incident magnetic field is parallel to the long axis of the cantilever, while it is minimal for angles of incidence that are perpendicular to it. Fig. 10 emphasizes the importance of analyzing the sources and sensors in a combined model, as slightly different dipole configurations can already lead to strong variation in the resulting sensor signals, based on the position and orientation of the sensor array relative to the source and the electric parameters of the head's tissues. Although only a limited number of examples can be presented in this work, theoretical investigations of different positions and orientations of the sensors, as well as a wide array of source configurations, can be modeled.

IV. Conclusion

In conclusion, we have demonstrated a combined multiscale 3-D FEM model consisting of an array of three orthogonal ME sensors and a simplified human head. Using electric point dipole sources located inside the head, we have simulated the excitation and propagation of electric and magnetic fields inside white matter, skull, and skin tissue domains, through the surrounding air environment, and into the ME sensor

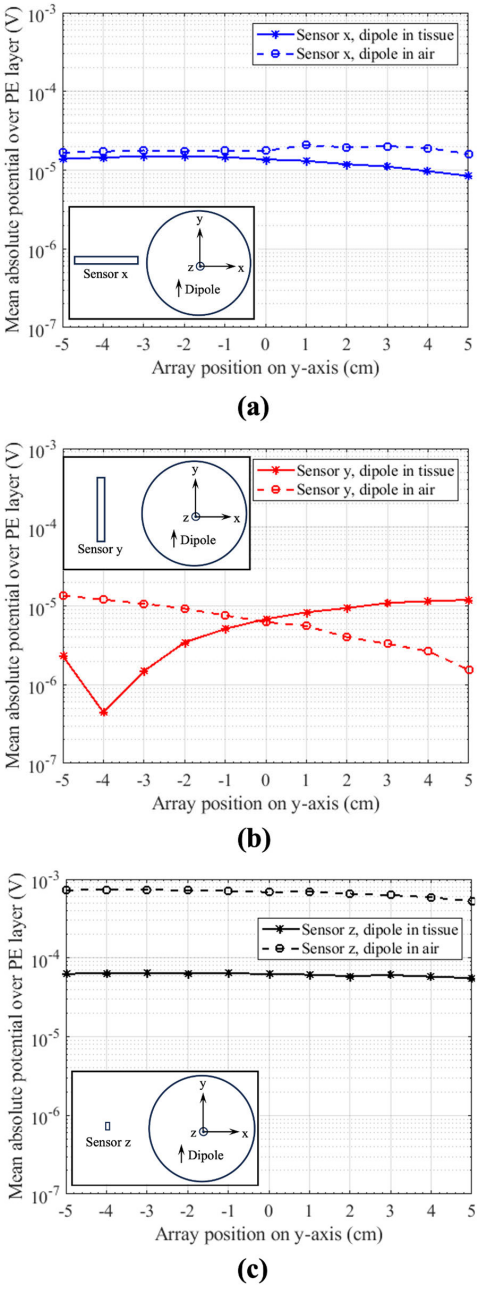

Fig. 9. Simulation results for the integrated absolute value of electric potential in the PE layers of each individual sensor and different material parameters for the head. The dipole is located at coordinates $x = y = -4$ cm and $z = +2$ cm and is oriented in y-direction. Plots with solid lines represent results for the head geometry with material parameters given in Table II, while the dashed lines show results for the head geometry set to material parameters of air. The graphs represent the directional behavior of the sensors oriented in: (a) x-direction; (b) y-direction; and (c) z-direction based on their position relative to the source inside of the head.

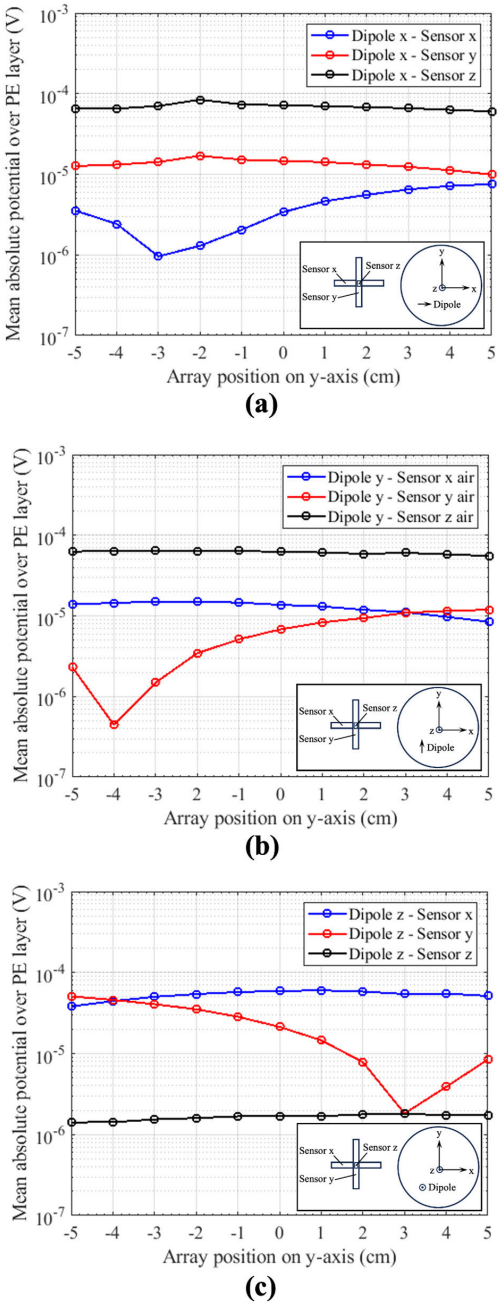

Fig. 10. Simulation results for the integrated absolute value of electric potential in the PE layers for the ME sensor array and three dipole configurations. The dipole is located at coordinates $x = y = -4$ cm and $z = +2$ cm in the white matter domain. The orientation for this dipole is: (a) in x-direction; (b) in y-direction; and (c) in z-direction. Distinct sensor responses for different cases are visible, including distinct minima at specific locations based on the angle of incidence between the magnetic vector field and the ME sensors.

array. Inside the sensor layers, we have evaluated the influx of magnetic field, as well as the resulting electric potential in the PE layer, based on the ME effect, for different ME sensor and dipole source positions and orientations. This comprehensive investigation allows us to study how the head geometry with its three tissue types and corresponding material parameters influences the propagation of the electromagnetic

field through the tissues and outside into the air environment, where it is picked up by the ME sensor array. In addition to that, we can compare sensor behavior for different sensor positions and orientations relative to the source inside the head and observe different responses. Furthermore, validation studies with the electric parameters of the head or sensor geometries set to high-conductivity air demonstrate the importance of modeling the ME sensor array in conjunction with the appropriate head geometry and material properties to achieve distinct and realistic sensor responses, as opposed to using simplified homogeneous excitation fields or relying on simple air environments. The ability to analyze both sensor behavior and the influence of the source configuration in a single comprehensive model should be a key aspect of future theoretical studies. Comparing the responses of differently oriented sensors for arbitrary source configurations holds the potential to optimize localization applications with arrays of ME sensors, such as DBS electrode localization [33] or ultrasound head localization [34]. Our setup also allows future investigations to take a closer look at the coupling between sensors in the array in order to optimize array geometries by minimizing crosstalk between sensors. A crucial question for upcoming investigations with the combined model is whether there is an interaction between ME sensors and the electromagnetic field inside the head. Combining sensor physics with the head model, follow-up investigations with a more advanced head geometry could, for example, answer the question whether the presence of the ME sensor introduces secondary effects, such as volumetric currents inside certain areas of the brain or modulation of the surrounding magnetic flux based on phenomena like sensor crosstalk or the magnetoelastic effect. Using different sensor geometries and the approach of frequency modulation, sensor systems that operate at relevant frequencies for their respective medical applications (e.g., MCG) could be modeled and further investigated with our approach. Finally, it is possible to utilize specialized head phantoms in measurement setups with corresponding FEM models to experimentally validate theoretical results [28], [35], which is a priority goal for further investigations.

Appendix
Material Parameters

We use material parameters for Si, AlN, and FeCoSiB (Metglas) from experimental studies and previous work to implement the ME sensor model [17], [36], [37], [38]

$$c_{\mathrm{E,AlN}} = \begin{pmatrix} 41 & 14.9 & 9.9 & 0 & 0 & 0 \\ 14.9 & 41 & 9.9 & 0 & 0 & 0 \\ 9.9 & 9.9 & 38.9 & 0 & 0 & 0 \\ 0 & 0 & 0 & 12.5 & 0 & 0 \\ 0 & 0 & 0 & 0 & 12.5 & 0 \\ 0 & 0 & 0 & 0 & 0 & 12.5 \end{pmatrix} \times 10^{10}\ \mathrm{Pa} \tag{A1}$$

$$e_{\mathrm{ES,AlN}} = \begin{pmatrix} 0 & 0 & 0 & 0 & -0.48 & 0 \\ 0 & 0 & 0 & -0.48 & 0 & 0 \\ 9.9 & 9.9 & 38.9 & 0 & 0 & 0 \\ -0.58 & -0.58 & 1.55 & 0 & 0 & 0 \end{pmatrix} \times \mathrm{C/m^2} \tag{A2}$$

$$\rho_{\mathrm{AlN}} = 3300\ \mathrm{kg/m^3} \tag{A3}$$

$$\varepsilon_{\mathrm{r,AlN}} = 8 \times 10^{-11}\ \mathrm{F/m} \tag{A4}$$

$$\mu_{\mathrm{r,AlN}} = 4\pi \times 10^{-7}\ \mathrm{H/m} \tag{A5}$$

$$c_{\mathrm{H,FeCoSiB}} = \begin{pmatrix} 150 & 45 & 45 & 0 & 0 & 0 \\ 45 & 150 & 45 & 0 & 0 & 0 \\ 45 & 45 & 150 & 0 & 0 & 0 \\ 0 & 0 & 0 & 40 & 0 & 0 \\ 0 & 0 & 0 & 0 & 40 & 0 \\ 0 & 0 & 0 & 0 & 0 & 40 \end{pmatrix} \times 10^{10}\ \mathrm{Pa} \tag{A6}$$

$$e_{\mathrm{HS,FeCoSiB}} = \begin{pmatrix} 8500 & -2833.3 & -2833.3 & 0 & 0 & 0 \\ 0 & 0 & 0 & 0 & 0 & 0 \\ 0 & 0 & 0 & 0 & 0 & 0 \end{pmatrix} \times \mathrm{N/Am} \tag{A7}$$

$$\rho_{\mathrm{FeCoSiB}} = 7250\ \mathrm{kg/m^3} \tag{A8}$$

$$\varepsilon_{\mathrm{r,FeCoSiB}} = 8.85 \times 10^{-12}\ \mathrm{F/m} \tag{A9}$$

$$\mu_{\mathrm{rS,FeCoSiB}} = 1.13 \times 10^{-3}\ \mathrm{H/m} \tag{A10}$$

$$E_{\mathrm{Si}} = 170 \times 10^{9}\ \mathrm{Pa} \tag{A11}$$

$$\nu_{\mathrm{Si}} = 0.28 \tag{A12}$$

$$\rho_{\mathrm{Si}} = 2329\ \mathrm{kg/m^3} \tag{A13}$$

$$\varepsilon_{\mathrm{r,Si}} = 11.7 \tag{A14}$$

$$\mu_{\mathrm{r,Si}} = 1. \tag{A15}$$

References

[1] F. Primdahl, "The fluxgate magnetometer," *J. Phys. E, Sci. Instrum.*, vol. 12, no. 4, pp. 241–253, Apr. 1979, doi: 10.1088/0022-3735/12/4/001.

[2] H. U. Auster et al., "The THEMIS fluxgate magnetometer," *Space Sci. Rev.*, vol. 141, nos. 1–4, pp. 235–264, Dec. 2008, doi: 10.1007/s11214-008-9365-9.

[3] A. Jodko-Władzińska, K. Wildner, T. Pałko, and M. Władziński, "Compensation system for biomagnetic measurements with optically pumped magnetometers inside a magnetically shielded room," *Sensors*, vol. 20, no. 16, p. 4563, Aug. 2020, doi: 10.3390/s20164563.

[4] J. P. Wikswo, "SQUID magnetometers for biomagnetism and nondestructive testing: Important questions and initial answers," *IEEE Trans. Appiled Supercond.*, vol. 5, no. 2, pp. 74–120, Jun. 1995, doi: 10.1109/77.402511.

[5] D. Viehland, M. Wuttig, J. McCord, and E. Quandt, "Magnetoelectric magnetic field sensors," *MRS Bull.*, vol. 43, no. 11, pp. 834–840, Nov. 2018, doi: 10.1557/mrs.2018.261.

[6] E. Elzenheimer et al., "Quantitative evaluation for magnetoelectric sensor systems in biomagnetic diagnostics," *Sensors*, vol. 22, no. 3, p. 1018, Jan. 2022, doi: 10.3390/s22031018.

[7] M. Zaeimbashi et al., "Ultra-compact dual-band smart NEMS magnetoelectric antennas for simultaneous wireless energy harvesting and magnetic field sensing," *Nature Commun.*, vol. 12, no. 1, p. 3141, May 2021, doi: 10.1038/s41467-021-23256-z.

[8] J. J. Ermer, J. C. Mosher, S. Baillet, and R. M. Leahy, "Rapidly recomputable EEG forward models for realistic head shapes," *Phys. Med. Biol.*, vol. 46, no. 4, pp. 1265–1281, Apr. 2001, doi: 10.1088/0031-9155/46/4/324.

[9] Z. A. Acar and S. Makeig, "Effects of forward model errors on EEG source localization," *Brain Topography*, vol. 26, no. 3, pp. 378–396, Jul. 2013, doi: 10.1007/s10548-012-0274-6.

[10] S. L. Kappel, S. Makeig, and P. Kidmose, "Ear-EEG forward models: Improved head-models for ear-EEG," *Frontiers Neurosci.*, vol. 13, p. 943, Sep. 2019, doi: 10.3389/fnins.2019.00943.

[11] H. A. Haque, T. Musha, and M. Nakajima, "Three-shell head model constructed from scalp geometry for electroencephalogram dipole localization," *Frontiers Med. Biol. Eng., Int. J. Jpn. Soc. Med. Electron. Biol. Eng.*, vol. 9, no. 4, pp. 295–304, 1999.

[12] G. Crevecoeur, H. Hallez, P. Van Hese, Y. D'Asseler, L. Dupré, and R. Van de Walle, "A hybrid algorithm for solving the EEG inverse problem from spatio-temporal EEG data," *Med. Biol. Eng. Comput.*, vol. 46, no. 8, pp. 767–777, Aug. 2008, doi: 10.1007/s11517-008-0341-z.

[13] M.-Ö. Özden, A. Teplyuk, Ö. Gümüs, D. Meyners, M. Höft, and M. Gerken, "Magnetoelectric cantilever sensors under inhomogeneous magnetic field excitation," *AIP Adv.*, vol. 10, no. 2, Feb. 2020, Art. no. 025132, doi: 10.1063/1.5136239.

[14] F. Blanc-Béguin, S. Nabily, J. Gieraltowski, A. Turzo, S. Querellou, and P. Y. Salaun, "Cytotoxicity and GMI bio-sensor detection of maghemite nanoparticles internalized into cells," *J. Magn. Magn. Mater.*, vol. 321, no. 3, pp. 192–197, Feb. 2009, doi: 10.1016/j.jmmm.2008.08.104.

[15] R. Jahns et al., "Giant magnetoelectric effect in thin-film composites," *J. Amer. Ceram. Soc.*, vol. 96, no. 6, pp. 1673–1681, Jun. 2013, doi: 10.1111/jace.12400.

[16] E. Lage, "Magnetoelektrische dünnschichtkomposite mit integriertem exchange bias," Ph.D. dissertation, Dept. Mater. Sci., Chair Inorganic Funct. Mater., Kiel Univ., Kiel, Germany, 2014.

[17] J. L. Gugat, J. Schmalz, M. C. Krantz, and M. Gerken, "Magnetic flux concentration effects in cantilever magnetoelectric sensors," *IEEE Trans. Magn.*, vol. 52, no. 5, pp. 1–8, May 2016, doi: 10.1109/TMAG.2015.2509948.

[18] J. L. Gugat, M. C. Krantz, J. Schmalz, and M. Gerken, "Signal-to-noise ratio in cantilever magnetoelectric sensors," *IEEE Trans. Magn.*, vol. 52, no. 9, pp. 1–5, Sep. 2016, doi: 10.1109/TMAG.2016.2557305.

[19] J. F. Blackburn, M. Vopsaroiu, and M. G. Cain, "Verified finite element simulation of multiferroic structures: Solutions for conducting and insulating systems," *J. Appl. Phys.*, vol. 104, no. 7, Oct. 2008, Art. no. 074104, doi: 10.1063/1.2988183.

[20] M. Guo and S. Dong, "A resonance-bending mode magnetoelectric-coupling equivalent circuit," *IEEE Trans. Ultrason., Ferroelectr., Freq. Control*, vol. 56, no. 11, pp. 2578–2586, Nov. 2009, doi: 10.1109/TUFFC.2009.1346.

[21] V. M. Petrov, G. Srinivasan, M. I. Bichurin, and T. A. Galkina, "Theory of magnetoelectric effect for bending modes in magnetostrictive-piezoelectric bilayers," *J. Appl. Phys.*, vol. 105, no. 6, Mar. 2009, Art. no. 063911, doi: 10.1063/1.3087766.

[22] D. Hasanyan et al., "Theoretical and experimental investigation of magnetoelectric effect for bending-tension coupled modes in magnetostrictive-piezoelectric layered composites," *J. Appl. Phys.*, vol. 112, no. 1, Jul. 2012, Art. no. 013908, doi: 10.1063/1.4732130.

[23] M. J. Peters and J. C. de Munck, "The influence of model parameters on the inverse solution based on MEGs and EEGs," *Acta Oto-Laryngologica*, vol. 111, no. 491, pp. 61–69, Jan. 1991, doi: 10.3109/00016489109136782.

[24] R. Van Uitert, D. Weinstein, and C. Johnson, "Volume currents in forward and inverse magnetoencephalographic simulations using realistic head models," *Ann. Biomed. Eng.*, vol. 31, no. 1, pp. 21–31, Jan. 2003, doi: 10.1114/1.1535412.

[25] D. Miklavčić, N. Pavšelj, and F. X. Hart, "Electric properties of tissues," in *Wiley Encyclopedia of Biomedical Engineering*, M. Akay, Ed. Hoboken, NJ, USA: Wiley, 2006, doi: 10.1002/9780471740360.ebs0403.

[26] *COMSOL Multiphysics Support, Private Communication*, COMSOL, Burlington, MA, USA, Jun. 2023.

[27] J. Volkmann, J. Herzog, F. Kopper, and G. Deuschl, "Introduction to the programming of deep brain stimulators," *Movement Disorders*, vol. 17, no. S3, pp. S181–S187, Mar. 2002, doi: 10.1002/mds.10162.

[28] M. Yalaz, A. Teplyuk, M. Muthuraman, G. Deuschl, and M. Höft, "The magnetic properties of electrical pulses delivered by deep-brain stimulation systems," *IEEE Trans. Instrum. Meas.*, vol. 69, no. 7, pp. 4303–4313, Jul. 2020, doi: 10.1109/TIM.2019.2945744.

[29] H. Koch, "Recent advances in magnetocardiography," *J. Electrocardiol.*, vol. 37, pp. 117–122, Oct. 2004, doi: 10.1016/j.jelectrocard.2004.08.035.

[30] C. Kirchhof et al., "Giant magnetoelectric effect in vacuum," *Appl. Phys. Lett.*, vol. 102, no. 23, Jun. 2013, Art. no. 232905, doi: 10.1063/1.4810750.

[31] M. Gerken, "Resonance line shape, strain and electric potential distributions of composite magnetoelectric sensors," *AIP Adv.*, vol. 3, no. 6, Jun. 2013, Art. no. 062115, doi: 10.1063/1.4811369.

[32] J. L. Gugat, "Entwurf, analyse und optimierung magnetoelektrischer sensoren mit hilfe der finite-elemente-methode," Ph.D. dissertation, Dept. Elect. Inf. Eng., Chair Integr. Syst. Photon., Kiel Univ., Kiel, Germany, 2016.

[33] M. Yalaz, A. Teplyuk, G. Deuschl, and M. Höft, "Dipole fit localization of the deep brain stimulation electrode using 3D magnetic field measurements," *IEEE Sensors J.*, vol. 20, no. 16, pp. 9550–9557, Aug. 2020, doi: 10.1109/JSEN.2020.2988067.

[34] C. Bald, R. Bergholz, and G. Schmidt, "Automatic localization of an ultrasound probe with the help of magnetic sensors," *Current Directions Biomed. Eng.*, vol. 8, no. 2, pp. 317–320, Sep. 2022, doi: 10.1515/cdbme-2022-1081.

[35] M. Yalaz, G. Deuschl, M. Butz, A. Schnitzler, A.-K. Helmers, and M. Höft, "Investigation of magnetoelectric sensor requirements for deep brain stimulation electrode localization and rotational orientation detection," *Sensors*, vol. 21, no. 7, p. 2527, Apr. 2021, doi: 10.3390/s21072527.

[36] A. Piorra et al., "Magnetoelectric thin film composites with interdigital electrodes," *Appl. Phys. Lett.*, vol. 103, no. 3, Jul. 2013, Art. no. 032902, doi: 10.1063/1.4812706.

[37] J. L. Gugat, M. C. Krantz, and M. Gerken, "Two-dimensional versus three-dimensional finite-element method simulations of cantilever magnetoelectric sensors," *IEEE Trans. Magn.*, vol. 49, no. 10, pp. 5287–5293, Oct. 2013, doi: 10.1109/TMAG.2013.2260346.

[38] A. Ludwig and E. Quandt, "Optimization of the ΔE-effect in thin films and multilayers by magnetic field annealing," in *Proc. IEEE Int. Magn. Conf.*, Amsterdam, The Netherlands, Apr./May 2002, p. AE2, doi: 10.1109/INTMAG.2002.1000626.

Mesut-Ömür Özden received the B.Sc. and M.Sc. degrees in electrical engineering and business administration from Kiel University, Kiel, Germany, in 2015 and 2016, respectively, where he is currently pursuing the Ph.D. degree with the Chair for Integrated Systems and Photonics and the Chair for Computational Electromagnetics.

His research interests include magnetic field simulation, the modeling of sensor systems, and finite-element method computation.

Julius Schmalz received the M.Sc. and Ph.D. degrees in electrical engineering from the University of Kiel, Kiel, Germany, in 2014 and 2021, respectively.

He has been with the Integrated Systems and Photonics Group, University of Kiel, since 2014.

Martina Gerken (Senior Member, IEEE) received the Dipl.-Ing. degree in electrical engineering from the University of Karlsruhe, Karlsruhe, Germany, in 1998, and the Ph.D. degree in electrical engineering from Stanford University, Stanford, CA, USA, in 2003.

From 2003 to 2008, she was an Assistant Professor with the University of Karlsruhe. In 2008, she was appointed as a Full Professor of Electrical Engineering and the Head of the Chair of Integrated Systems and Photonics, Kiel University, Kiel, Germany.

5.2 Key Findings and Scientific Implications

- The combined ME sensor and human head FEM model allows investigations on how sources placed inside of the head geometry with its respective tissues' electric properties affect the induction and propagation of a magnetic field and the ME sensor response to it.
- Depending on the orientation of the dipole source and orthogonal ME sensors, the sensor response can strongly vary due to the sinusoidal directional sensitivity of the sensors, distance from the source, location of the source, and geometry of the head.
- Propagation of the magnetic field from source to sensor array is influenced by the electric material parameters and geometry of the head, even though constant vacuum permittivity is assumed for the skin, skull, and white matter regions.
- Simulating the head and sensors in a combined model offers important insights on sensor behavior compared to simple homogeneous or inhomogeneous excitation methods.
- The sensor and head models can be individually modified, enabling different array configurations or sensor types, as well as more advanced head geometries or application-specific combined models (e.g., DBS electrodes) for direct comparison with experimental measurements.

Chapter 6

A Combined Magnetoelectric Sensor Array and MRI-Based Human Head Model for Biomagnetic FEM Simulation and Sensor Crosstalk Analysis

6.1 Published Article

Reference: *Mesut-Ömür Özden, Giuseppe Barbieri, and Martina Gerken. "A Combined Magnetoelectric Sensor Array and MRI-Based Human Head Model for Biomagnetic FEM Simulation and Sensor Crosstalk Analysis". MDPI Sensors, vol. 24, issue 4, no. 1186, 2024, doi:10.3390/s24041186.*

Statement about own contribution:

For this work I developed the modeling concept, set up the FEM model, and conducted the simulations. Furthermore, I evaluated the results and wrote the manuscript.

Conceptualization	Planning	Implementation	Manuscript preparation
High	High	High	High

sensors

MDPI

Article

A Combined Magnetoelectric Sensor Array and MRI-Based Human Head Model for Biomagnetic FEM Simulation and Sensor Crosstalk Analysis

Mesut-Ömür Özden *, Giuseppe Barbieri and Martina Gerken *

Integrated Systems and Photonics, Department of Electrical and Information Engineering, Kiel University, Kaiserstraße 2, 24143 Kiel, Germany; giba@tf.uni-kiel.de

* Correspondence: omoz@tf.uni-kiel.de (M.-Ö.Ö.); mge@tf.uni-kiel.de (M.G.); Tel.: +49-431-880-6250 (M.G.)

Abstract: Magnetoelectric (ME) magnetic field sensors are novel sensing devices of great interest in the field of biomagnetic measurements. We investigate the influence of magnetic crosstalk and the linearity of the response of ME sensors in different array and excitation configurations. To achieve this aim, we introduce a combined multiscale 3D finite-element method (FEM) model consisting of an array of 15 ME sensors and an MRI-based human head model with three approximated compartments of biological tissues for skin, skull, and white matter. A linearized material model at the small-signal working point is assumed. We apply homogeneous magnetic fields and perform inhomogeneous magnetic field excitation for the ME sensors by placing an electric point dipole source inside the head. Our findings indicate significant magnetic crosstalk between adjacent sensors leading down to a 15.6% lower magnetic response at a close distance of 5 mm and an increasing sensor response with diminishing crosstalk effects at increasing distances up to 5 cm. The outermost sensors in the array exhibit significantly less crosstalk than the sensors located in the center of the array, and the vertically adjacent sensors exhibit a stronger crosstalk effect than the horizontally adjacent ones. Furthermore, we calculate the ratio between the electric and magnetic sensor responses as the sensitivity value and find near-constant sensitivities for each sensor, confirming a linear relationship despite magnetic crosstalk and the potential to simulate excitation sources and sensor responses independently.

Keywords: biomagnetic sensor; crosstalk; finite-element method (FEM); human head model; magnetic fields; magnetoelectric effect; MRI data; multiferroic device; multiscale model; sensor array

Citation: Özden, M.-Ö.; Barbieri, G.; Gerken, M. A Combined Magnetoelectric Sensor Array and MRI-Based Human Head Model for Biomagnetic FEM Simulation and Sensor Crosstalk Analysis. *Sensors* **2024**, *24*, 1186. https://doi.org/10.3390/s24041186

Academic Editor: José Machado Da Silva

Received: 23 December 2023
Revised: 7 February 2024
Accepted: 7 February 2024
Published: 11 February 2024

1. Introduction

In the field of medical diagnostics, bioelectric measurements are commonly performed on patients to investigate possible pathological disorders. Well-known applications of this kind are the electrocardiogram (ECG) and the electroencephalogram (EEG), which measure and evaluate the electric activities of the human heart and brain, respectively. To perform them, electrodes are applied directly on the patient's body and the electric potential generated by the heart or brain activity is measured on the surface of the skin. While electrical measurements such as ECG and EEG are of the utmost importance and allow physicians to gather valuable vital information on a patient's health with cost-effective and widely available machines and with high temporal resolution, they do have drawbacks as well, leading to increasing interest in measurement applications based on the magnetic sensing of biological signals. As an alternative or complementary measurement technique to bioelectric signals [1], biomagnetic signals can also be measured with appropriate sensing devices such as fluxgate magnetometers [2,3], optically pumped magnetometers [4], SQUID systems [5], and magnetoelectric (ME) magnetic field sensors [6–9].

In current clinical and research applications, SQUID sensors are used as the gold standard for magnetic measurements down to the femtotesla (fT) range, enabling their use in applications such as magnetoencephalography (MEG) [5,10]. Multi-channel SQUID

magnetometers with helmet-shaped dewars have the ability to cover several head regions and reduce measurement times simultaneously [5], and state-of-the-art devices achieve a noise spectral density of approximately 3 $fT/Hz^{1/2}$ [11], allowing their efficient and precise application in MEG.

While SQUIDs are still the sensing device of choice for many applications due to their extremely high sensitivity, ME sensors were recently shown to be promising in highly versatile and novel applications ranging from automatic real-time magnetic localization of an ultrasound probe [12], to magnetic detection of positions and orientations of deep brain stimulation (DBS) electrodes in patients [13], to magnetic motion analysis for swallowing detection in individuals suffering from dysphagia [14]. Crucially, measurements in the operation room or even wearable solutions could be possible with ME sensors for applications such as the detection and orientation of DBS electrodes or swallowing detection, which are currently not feasible with SQUID systems.

Even outside the scope of biomagnetic sensing, ME devices have the potential for a variety of applications, such as energy-efficient memory [15,16], antennas and energy harvesting [17,18], electric current sensing [19], and automotive applications [20]. Lastly, as opposed to many other magnetic sensing systems, ME sensors also offer the potential for room-temperature, passive and unshielded operation [9,21]. In this work, we demonstrate a combined multiscale 3D finite-element method (FEM) model including several ME sensors in different array configurations and a detailed anatomical human head model based on MRI data. Previous investigations report simplified spherical or realistic anatomical head models and magnetic field calculations for specific applications such as the EEG or MEG forward problem. Extremely detailed models on EEG and MEG applications exist, which even consider how the movement of the brain inside the cerebrospinal fluid relative to the inner skull due to subjects' changing body position can affect mesh generation [22,23]. However, the respective sensor systems for such applications are often not jointly evaluated at all, or simplified to point [24] or circular magnetometers [25]. However, ME sensors are not of a negligible size and their geometry plays a role in the sensitivity of measurements [26]. Therefore, the study framework presented in this work is necessary to simulate sensors and the head or throat in a single FEM model. In this case, we focus on the head, as the simulation framework is known from previous MEG cases, and we significantly extend this framework by integrating the sensors in the simulation. The key novelty of this approach is the complete integration of an MRI-based head model with a fully coupled ME sensor array model and its physical properties. This enables us to evaluate the mechanical, electrical, and magnetic behavior of the magnetoelectric sensing devices in a variable array configuration. Additionally, the inclusion of further components such as operation instruments could be added to the simulation framework.

With this extensive model, we aim to investigate the response of ME sensors to different excitation mechanisms such as homogeneously applied external magnetic fields and a dipole source inside the human head. We also evaluate the concept of magnetic crosstalk between adjacent ME sensors in the different array configurations, which is based on the high-permeability material utilized in the magnetostrictive layers of the devices. This crosstalk can lead to adverse sensing performance based on the location of each sensor inside the array, the distance to adjacent sensors and the excitation source, and the method of excitation (i.e., homogeneous vs. inhomogeneous excitation). Lastly, we calculate the ratio between electric sensor response and the magnetic flux density for each individual sensor in order to determine whether the separability of effects is visible in our combined FEM simulation, as expected for a linear model. While the inclusion of nonlinear effects due to magnetic material properties or secondary currents induced in the head requires a combined model, determining a simple linear relationship between the magnetic sensor excitation and the electric response justifies the investigation of excitation sources and sensor responses in separate models. This greatly reduces computational requirements, allows for higher resolution meshing, and enables arbitrary combinations of separately developed source and sensor models.

Sensors **2024**, *24*, 1186

Figure 1 visualizes the concept of the simulations presented in this work. In (a), we illustrate a clipped view of the head model with its tissue regions of skin, skull, and white matter, as well as the point dipole located in the latter region. (b) demonstrates an electric current point dipole source inside the head inducing the propagation of an inhomogeneous magnetic field. This magnetic field propagates through the head, into the surrounding air environment, and becomes the excitation source for the ME sensor array. The individual sensors within the array can display vastly different responses to this excitation based on the previously mentioned parameters, which we aim to systematically investigate and discuss throughout this work.

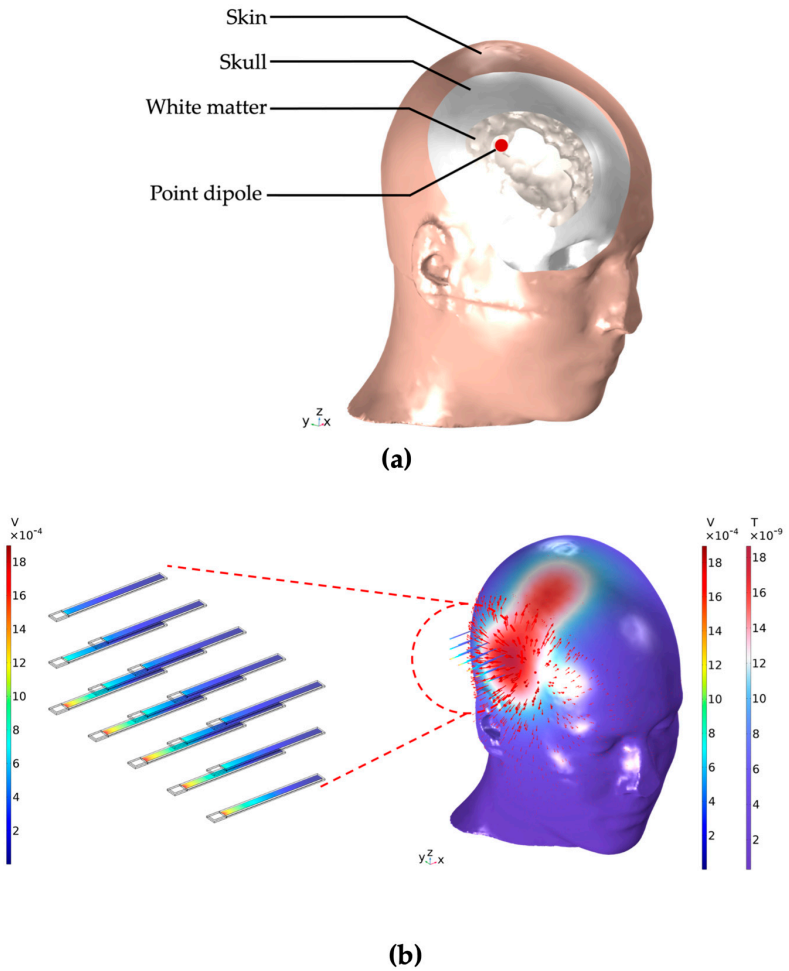

Figure 1. (**a**) Clipped view of the human head with its tissue regions of skin, skull, and white matter. The white matter region contains an electric current point dipole source—as would be obtained with a deep-brain stimulation electrode—which creates an electromagnetic field. This field propagates through the tissues of the head, through the air environment, and into the ME sensor array. Shown in (**b**) are the magnetic flux density norm on the head's surface with corresponding vector arrows and, based on this propagating magnetic field as the method of excitation, the electric response of an adjacent ME sensor array with 15 sensors. The sensors are located at a distance of 1.5 cm from the head and a distance of 1 cm between neighboring sensors. The resulting absolute potential on the surface of each individual piezoelectric layer is shown.

Our study is divided into the following sections. Section 2 offers insights into the setup and geometries of the separate ME sensor and human head models and their merging into a joint multiscale 3D FEM model. We also describe our simulation method and variations

Sensors **2024**, *24*, 1186

within the model that are relevant to our investigation, as well as the process of obtaining the head model from raw MRI data. In Section 3, we showcase the results of magnetic field excitation and propagation, as well as the ME sensor array behavior for different excitation and array configurations. We highlight the magnetic and electric effects of the sensor response and investigate the magnetic crosstalk between adjacent sensors based on their position in the array and the relationship between electric response and magnetic excitation of the ME sensors. Lastly, Section 4 includes important discussion points of the obtained results and concludes our work with an emphasis on major insights gained by this study, as well as important implications for future research in the field of magnetoelectric sensors.

2. Models and Methods

The MRI-based human head model, the single ME sensor model, and the ME sensor array model were developed and combined using COMSOL Multiphysics 6.1 with its built-in *solid mechanics*, *magnetic fields*, and *electrostatics* interfaces. The software was used to set up and perform 3D FEM simulations in the frequency domain with magnetic excitation at the cantilever sensor's physical resonance frequency of 848 Hz. The software pipeline to process medical MRI data into the segmented 3D human head model, as well as the working principle, geometry, and physical properties of the ME sensors, will be explained in the following subsections. Lastly, we will describe the integration of both components into the combined multiscale head and sensor model before moving on to the results section of our study. We performed the simulations shown in this work using an Intel Xeon E5-2697A v4 CPU with 64 cores at 2.60 GHz, 503.8 GiB RAM and Ubuntu OS 22.04.3.

2.1. MRI-Based Human Head Model

In order to create an approximation of the head and improve the previous spherical model [27], MRI-based medical images were processed into a 3D FEM model of the human head for this investigation. In the literature, there are now many open- and closed-source databases from which to extract these types of medical raw data. The specific model considered in this study is derived from the NY Head Model constructed by the Parra Lab group at the City University of New York [28]. The segmentation data were obtained by averaging three different MRI sources for various tissues: the brain is acquired from the symmetric ICBM-152 v2009, non-brain tissues are extrapolated from the symmetric ICBM-152 v6, and the lower portion of the head from [28]. The general model was based and validated on four individual heads, whereby a precise FEM model was built for each of them [29]. The final segmentation files after the averaging operation involve the symmetric geometry of the entire head. This was taken into consideration due to the symmetric properties exhibited by objects imported into COMSOL Multiphysics, which can significantly reduce the computational cost of any simulations.

The provided dataset from [28] was processed and tissue regions for the skin, skull, and brain were extracted. To process the *.nifti* segmentation files, two software programs were used: *MATLAB* R2023b for creating closed and volumetric 3D objects, and *3D Slicer* 5.2.2 for refining geometry operations. In particular, the *iso2mesh* 3D library in *MATLAB*, which provides excellent computational capabilities for binary and grayscale volumetric images such as segmented MRI/CT scans, was utilized.

The *.nifti* files for each of the three tissues were loaded, opened, and converted into binary logical values to identify each grayscale level of the segmented geometry. Subsequently, a closing operation was performed on each geometry to obtain a final closed water-tight object, thus avoiding "holes" that could introduce discontinuities in the final mesh. Utilizing the *fillholes3d.m* function with a gap size of 55 for each of the three tissues resulted in the creation of the three objects. The gap size is a crucial parameter, representing the size of the hole to be filled in the geometry. In this case, a trade-off was sought, as large gap sizes would lead to a geometry significantly different from the original, especially for the brain, while very small values would introduce an almost negligible approximation in the geometry.

Sensors **2024**, *24*, 1186

Subsequently, the 3D binary image was converted into an actual volume using the *imedge3d.m* function which extracts contour voxels from a binary image. Finally, the object was reconverted into the *.nifti* format and exported.

For the final processing, *3D Slicer* was used. The three objects were imported into the software after being processed in *MATLAB*. Due to the reduced complexity of the geometry after the previous closing operation, the 3D representation of the object was obtained using the Otsu thresholding method. Subsequently, cutting operations were performed in *3D Slicer*, allowing for the manual removal of small volumes from the object. These volumes are considered undesirable for the final purpose, as they would provide extra material for meshing without a specific purpose. Additionally, the lower part of the skull (including the first vertebrae of the spine) was partially removed, as this part of the head is negligible for the simulations.

After the cutting operation, some of the modified surfaces underwent shape changes. To address this, classic morphological opening and closing operations were applied to remove small extrusions remaining in the geometry and fill small residual holes. Finally, a smoothing operation was performed; more specifically, Gaussian smoothing was used.

Moreover, only for the skull, a "grow" operation was carried out using the *margin operation* tool to give it a thickness of about 3 mm. The uniform thickness of the skull adds a high degree of homogeneity to the final mesh but represents a strong approximation of the skull, while the real thickness of the skull is not uniform along the skullcap. The last step in 3D Slicer was to export the geometry in *.stl* format, ready to be imported into COMSOL Multiphysics 6.1. Figure 2 illustrates the resulting geometry and mesh of the three tissue regions of the head.

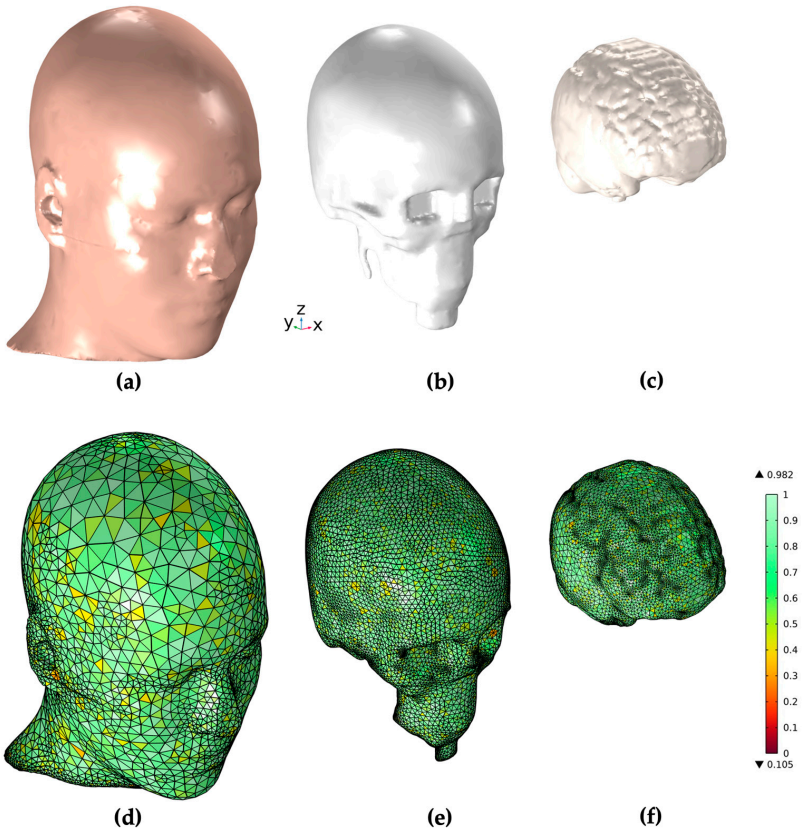

Figure 2. COMSOL Multiphysics geometry and mesh generation of the three tissue regions of the head. (**a**–**c**) show the geometry of the skin, skull, and white matter region, while (**d**–**f**) illustrate the meshed geometries for those regions in the stand-alone head model.

Sensors **2024**, *24*, 1186

In order to perform simulations including the electromagnetic properties of the human head, each region was assigned a specific conductivity and relative permittivity value taken from the literature [30–32]. Table 1 gives an overview of the utilized values.

Table 1. The regions of the human head model with their respective specific conductivity and relative permittivity taken from literature.

Region	Specific Conductivity [30,31]	Relative Permittivity [32]
Skin	1.00 S/m	1,200,000
Skull	0.05 S/m	40,000–1,000,000
White Matter	0.43 S/m	30,000,000

2.2. ME Sensor Model

We designed and implemented the ME sensor based on the ME sensor models from our previous work [26,27]. Each sensor consisted of a substrate layer of silicon with 26.25 mm length, 2.45 mm width, and 300 µm thickness, a magnetostrictive layer of FeCoSiB with 22.90 mm length, 1.80 mm width, and 20 µm thickness, and a piezoelectric layer of aluminum nitride (AlN) with 25.60 mm length, 1.60 mm width, and 20 µm thickness. The AlN is polycrystalline, and both the magnetostrictive and piezoelectric layer can be produced for experimental measurements via an in-house magnetron sputtering process [33]. The magnetostrictive and piezoelectric layers were located on the opposite sides of the substrate layer. The thickness of the active layers was chosen at a factor of 10 times higher than that typically used in experimental sensors at Kiel University to reduce the computation time. The sensor operated in resonant bending mode and fixed-free configuration at a resonance frequency of 848 Hz. Figure 3 gives an overview of the ME sensor geometry.

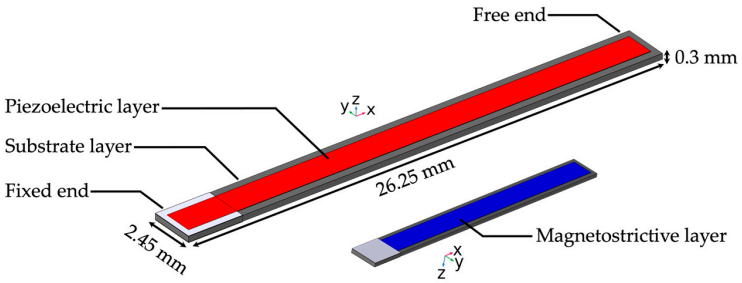

Figure 3. The ME sensor model. The cantilever sensor is shown with substrate layer in grey and the piezoelectric layer on the surface in red. The left end of the sensor is clamped, while the right end is free, resulting in the fixed-free bending mode operation. The smaller inset shows the opposite side of the substrate with the magnetostrictive layer on top in blue. The length, width, and thickness for the substrate layer are given in mm.

Table 2 gives an overview of the three layers forming the composite ME sensor. The magnetostrictive layer, piezoelectric layer, and substrate layer each have their unique material parameters which are given in Appendix A. A linearized material model was used at the sensor's small-signal working point. Details of the applied boundary conditions and physical properties of the three layers are described in our previous work [26,27].

Table 2. The layers of the ME sensor model with their materials, length, width, and height.

Layer	Material	Length	Width	Height
Magnetostrictive	FeCoSiB	22.90 mm	1.80 mm	20.00 µm
Piezoelectric	AlN	25.60 mm	1.60 mm	20.00 µm
Substrate	Si	26.25 mm	2.45 mm	300.00 µm

The mathematical model and physical properties of cantilever ME sensors consisting of ideal and slipless composite layers are governed by systems of differential and constitutive equations which are characterized in detail in previous studies [30,34–38]. The equations that we discuss below define our 3D-FEM model and are utilized in three built-in physics interfaces in COMSOL Multiphysics 6.1: the *solid mechanics*, *magnetic fields*, and *electrostatics* interfaces. This set of equations was also utilized and described in our previous work containing ME sensors and a simplified human head model [12]. It is repeated here for easy access. Beginning with *solid mechanics*, this interface describes a set of equations that couples the mechanical, electrical, and magnetic properties of the ME sensor and contains specific terms for each layer.

$$-\rho\omega^2\boldsymbol{u} = \nabla \cdot S \tag{1}$$

$$S = \boldsymbol{C} : \varepsilon \tag{2}$$

$$\varepsilon = \frac{1}{2}\left[(\nabla \boldsymbol{u})^{\mathrm{T}} + \nabla \boldsymbol{u}\right] \tag{3}$$

$$\boldsymbol{C} = \boldsymbol{C}(E, \nu). \tag{4}$$

The first set of Equations (1)–(4) corresponds to the *linear elastic material* node which covers the general mechanical properties of the model and includes S and ε for stress and strain, u as the displacement vector, the density ρ and the angular frequency ω. For the silicon substrate specifically, the coupling between stress and strain is a function of its Young's modulus and Poisson's ratio and is described by C in Equation (2).

The magnetostrictive and piezoelectric layers have separate physics nodes discussed below, starting with the *magnetostrictive material* node:

$$S = c_H : \varepsilon - \boldsymbol{H} \cdot e_{HS} \tag{5}$$

$$\boldsymbol{B} = \mu_0\, \mu_{\mathrm{r}S}\boldsymbol{H} + e_{HS} : \varepsilon. \tag{6}$$

Equations (5) and (6) include the coupling matrix in Voigt notation e_{HS} and the elasticity matrix c_H. This node also governs the relation between the magnetic flux density vector $\boldsymbol{B}$, the magnetic field vector $\boldsymbol{H}$, and the relative permeability $\mu_{\mathrm{r}S}$ of the material. Analogous to the *magnetostrictive material* node, the *piezoelectric material* node has a specific set of equations that describe its properties, including the coupling of the ME sensor's electric and elastic properties:

$$\nabla \cdot \boldsymbol{D} = \rho_{\mathrm{v}} \tag{7}$$

$$S = c_E : \varepsilon - \boldsymbol{E} \cdot e_{ES} \tag{8}$$

$$\boldsymbol{D} = \varepsilon_0\, \varepsilon_{\mathrm{r}S}\boldsymbol{E} + e_{ES} : \varepsilon. \tag{9}$$

In Equation (7), Gauss's law for the relation between the electric displacement field $\boldsymbol{D}$ and the volume charge density is applied to the model. Equations (8) and (9) include the coupling matrix in Voigt notation e_{ES} and the elasticity matrix c_E, as well as $\boldsymbol{E}$ for the electric field vector and $\varepsilon_{\mathrm{r}S}$ for the relative permittivity. We used the stress-magnetization and the stress-charge form for the magnetostrictive and piezoelectric material nodes, respectively. The Equations (1)–(9) that we described so far are applied in the *solid mechanics* physics node of our model and include elastic material properties, as well as coupling between the sensor layers. The electric and magnetic behavior of our model is governed in the *magnetic fields* and *electrostatics physics* nodes of our model given in Equations (10)–(12):

$$\nabla \times \boldsymbol{H} = \sigma\boldsymbol{E} + j\omega\boldsymbol{D} \tag{10}$$

$$\boldsymbol{B} = \nabla \times \boldsymbol{A} \tag{11}$$

$$\boldsymbol{E} = -\nabla V - j\omega\boldsymbol{A} \tag{12}$$

$$\boldsymbol{D} = \varepsilon_0\, \varepsilon_{\mathrm{r}}\boldsymbol{E} \tag{13}$$

$$\boldsymbol{B} = \mu_0\, \mu_{\mathrm{r}}\boldsymbol{H}. \tag{14}$$

Sensors **2024**, *24*, 1186

With Equations (10)–(12) we utilized Maxwell's equation and related electric and magnetic fields to the magnetic vector potential $\boldsymbol{A}$. The equation for the electric field strength used in the model is given in (12). Equations (13) and (14) apply via the boundary condition *Ampère's law* in the *magnetic fields* physics interface to the silicon substrate. Additionally, this boundary condition defines the general constitutive relations of $\boldsymbol{D}$ and $\boldsymbol{E}$ for the magnetostrictive material, as well as $\boldsymbol{B}$ and $\boldsymbol{H}$ for the piezoelectric material, in instances where no more specific physical properties are assigned, i.e., no magnetostriction for the piezoelectric material or piezoelectricity for the magnetostrictive material. With the set of equations given in (1)–(14), our multiscale combined ME sensor and human head model can be simulated with different electric and magnetic excitation methods, and full magnetoelectric coupling of the sensor layers.

2.3. ME Sensor Array Model

The aim of this work is to combine 15 individual ME sensors into a sensor array and investigate the response of each individual sensor based on its relative position in the array and distance from the neighboring sensors for different types of magnetic excitation. To achieve this goal, we organized the sensors into a 3×5 grid to form an array with three rows and five columns of adjacent sensors. The long axis of the sensors was parallel to the x-axis and the piezoelectric layer faced upwards in z-direction. The distances between the sensors in the array varied from 5 mm up to 5 cm in the vertical and horizontal directions simultaneously. Figure 4 illustrates the array configuration with the distance between neighboring sensors set to 5 mm. An array of these or similar dimensions was chosen due to in-house fabrication approaches at Kiel University and the possibility of using the array in an operation room, as a smaller array with variable positioning would potentially allow surgical procedures without covering the entire head.

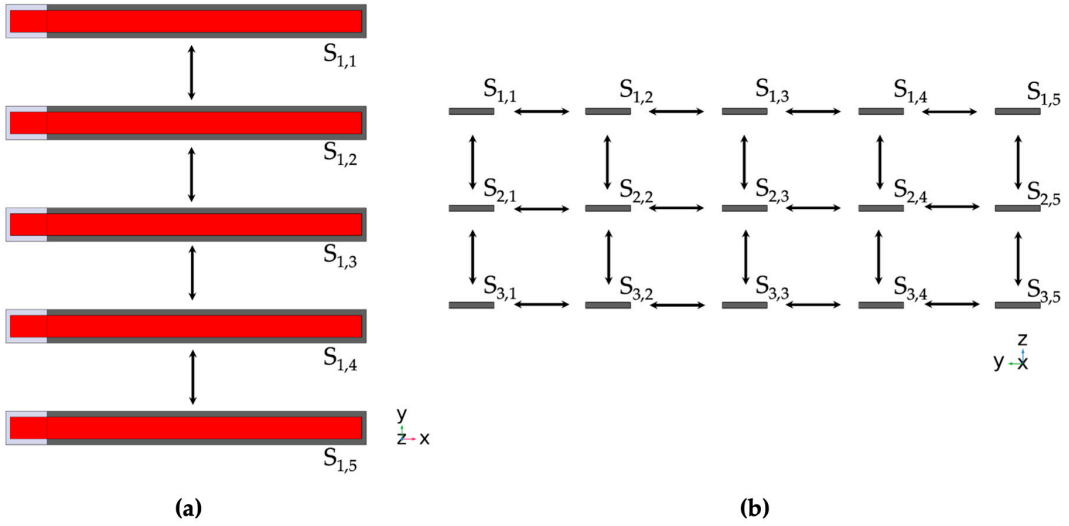

Figure 4. (**a**) Top-down view and (**b**) frontal view (on fixed end) of the 15-sensor array. Between each adjacent sensor is a variable distance between 1 mm and 5 cm. This figure shows equidistant sensor placement with 5 mm between the neighbors in both vertical and horizontal direction. The variable distance allowed us to investigate the magnetic crosstalk between sensors and analyze the influence of the magnetostrictive layers on nearby ME sensors.

2.4. Combined MRI-Based Human Head and ME Sensor Array Model

After establishing the human head and ME sensor array models separately, we combined both parts into the joint multiscale model. The sensors in the array can be located at arbitrary positions in space and distances both from the head and adjacent sensors. The challenge to be overcome was to combine both the anatomical head model, as well

as the ME sensor array model with 15 sensors, into one combined multiscale and multiphysics model. A core consideration for this was the differences in dimensions between the different model domains. While the sensors' PE and MS layers had a thickness of only 20 µm, the diameter of the head was approximately 20 cm. This translated to a vastly different size and resolution of mesh elements for the differently sized domains, because the mesh is designed such that extremely thin layers are of a sufficiently small size, while larger domains are modeled with larges element sizes to reduce the computational load. The number of degrees of freedom (DOF) solved for in a combined model with three ME sensors demonstrated in previous work [27] is approximately 25 million, while the number increases to approximately 70 million DOF when including 15 ME sensors in the array. The number of DOF is determined by the amount of mesh elements, as well as the utilized physics in the model, and is an important figure of merit for the computational requirements to solve a given FEM model. Details on the mesh parameters for all structures in a model with three ME sensors are given in Appendix B, with sizes referring to the longest edge of tetrahedral mesh elements.

Increasing the number of sensors from three to 15 posed a challenge in terms of computation time and hardware requirements for the computer running our simulations, since the number of DOF almost tripled in the combined model with a larger array and full mechanical, magnetic and electric coupling. Using the mesh parameters given in Appendix B, we were not able to achieve a successful simulation run with a converged solution. In order to achieve a solution, we iteratively adjusted some parts of the mesh to be coarser than in the previous study [27], while keeping the mesh resolution as high as possible for the sensor geometry. The adjusted mesh parameters for this investigation step included the head geometry, the air environment, and the substrate layer of the ME sensors. The magnetostrictive and piezoelectric layers remained unchanged. The mesh parameters for the combined model with 15 sensors are given in Appendix C. Inspecting the mesh yielded some elements of low quality for the figure of merit skewness, but no significant number of elements of poor quality (defined by skewness under 0.1 according to COMSOL's guidelines). The coarser mesh might have adversely impacted the accuracy of the solutions provided in the results section, but was necessary to enable our simulations to finish successfully.

Due to challenges with the numerical stability of our solutions, two simplifying conditions had to be applied to our model. Firstly, based on communications with COMSOL employees, calculating 3D FEM models with very high differences in material parameters such as the specific conductivity may result in a failure to find a converged solution [39]. In this case, this affects the near-zero specific conductivity of air which fills most of the modelling space. A recommended solution for this is to artificially increase the specific conductivity of the material in question sufficiently; thus, we set the conductivity of our air domain to 1×10^{-6} S/m. Secondly, we increased the numerical stability of our simulations with dipole excitation by positioning a second dipole with the same orientation and a magnitude 1 µA·m at a distance of 2 mm directly below the main excitation dipole of magnitude 1 mA·m. Due to the factor of a thousand between dipole magnitudes, the contribution of the secondary dipole to the overall electromagnetic field is considered negligible, while empirically improving the convergence of the utilized indirect solver we used. The application of similar conditions to improve numerical stability was also discussed in our previous work [27].

3. Results

The results in this section are categorized into two different types of magnetic field excitation. First, we looked at the array's response in a constant, homogeneous magnetic field, which is applied to the entire model volume. Following that, we replaced the homogeneous magnetic field excitation with a single electric current point dipole source inside the white matter region of the head model. For the investigation of the crosstalk effect, the distance between adjacent sensors in both the horizontal and vertical directions

Sensors **2024**, *24*, 1186

was varied in four steps within an interval between 5 mm and 5 cm. As the distance between neighboring sensors changes, the magnetic flux between them changes direction and is guided inside the highly permeable magnetostrictive layers of the sensors. For each sensor distance, a simulation with either homogeneous or dipole excitation was performed and the response for each sensor in the array was evaluated. Different distances between sensors result in different sensor responses depending on the position inside the array, as the following sections will demonstrate.

3.1. Homogeneous Excitation

We performed magnetic excitation of the ME sensor array using a homogeneous magnetic field strength of 1 A/m in x-direction applied to the entire model environment. The aim of this study step was to establish and validate the basic sensor response to a simple excitation field and investigate potential crosstalk effects independently of influences of inhomogeneous field effects. Before each array simulation, validation steps were conducted for homogeneous and dipole excitation, i.e., the sensor material parameters were set to those of the air environment in order to eliminate geometric or numeric inconsistencies and validate the magnetic flux density inside the model domain without the presence of high-permeability sensor material. Figure 5a shows a schematic of the full array and highlights the five sensors of the middle row, namely sensors $S_{2,1}$, $S_{2,2}$, $S_{2,3}$, $S_{2,4}$, and $S_{2,5}$. We further highlight the exemplary behavior of these five sensors in Figure 5b, where we display the sensors in a homogeneous excitation magnetic field in x-direction and the corresponding magnetic flux density inside the magnetostrictive layer for each sensor. The distance between adjacent sensors was 1 cm. The outermost sensors $S_{2,1}$ and $S_{2,5}$ exhibited the highest magnetic flux density, followed by sensors $S_{2,2}$ and $S_{2,4}$. The central sensor, $S_{2,3}$, exhibited the lowest magnetic flux density out of all sensors in the array due to its central position and the resulting crosstalk with its adjacent sensors. Finally, Figure 5c gives a plot of the magnetic flux density norm inside every sensor of the full array with 15 sensors for different distances between adjacent sensors. The previously observed behavior of high crosstalk between adjacent sensors at low distances is clearly visible, while the closer a sensor is to the center of the array, the stronger the effect. At a distance of 5 cm between the sensors, the crosstalk effect is negligible, and all sensors exhibit approximately the same response. At each individual distance between adjacent sensors, the sensor with the lowest magnetic flux density was the middle sensor ($S_{2,3}$), while the highest flux density was shared between the four corner sensors ($S_{1,1}$, $S_{1,5}$, $S_{3,1}$, $S_{3,5}$). At the lowest distance of 5 mm, the flux density in the corner sensors was 7.9% higher than in the middle sensor. For the central sensor ($S_{2,3}$), the magnetic flux density was 15.6% lower at a distance of 5 mm compared to a distance of 5 cm to its neighbors. Notably, the crosstalk effect was significantly stronger with up to 11% for sensors with closely vertically adjacent sensors, compared to horizontally adjacent sensors, based on simulations considering exclusively horizontally or vertically adjacent sensors. For the electric potential, Figure 5d offers similar general behavior for the crosstalk effect based on the electric behavior. Here, while the values converge for all sensors at a distance of 5 cm between neighbors for the magnetic flux density, the electric potential still sees a difference of approximately 4% between the highest (S_{33}) and lowest (S_{12}) at that distance. We expect numerical error to this degree based on the calculation of the fully coupled magnetoelectric effect between the layers as a possibility for the slightly diverging behavior of the electric response of the sensors.

3.2. Dipole Excitation

After evaluation of the behavior of the ME sensor array in homogeneous magnetic field excitation, we moved towards a specific inhomogeneous excitation mechanism. An electric current point dipole was placed at coordinates $x = 30$ mm, $y = -20$ mm, and $z = 30$ mm inside the white matter compartment of the head geometry, within the approximated right cerebral hemisphere. This configuration serves as a representative of a deep-brain stimulation scenario. The dipole moment, combined with the electric properties of the head,

Sensors **2024**, *24*, 1186

results in an induced magnetic field propagating through the head and the air environment into the ME sensor array, enabling us to evaluate its response and gain further insights into the behavior of the individual sensors in inhomogeneous excitation.

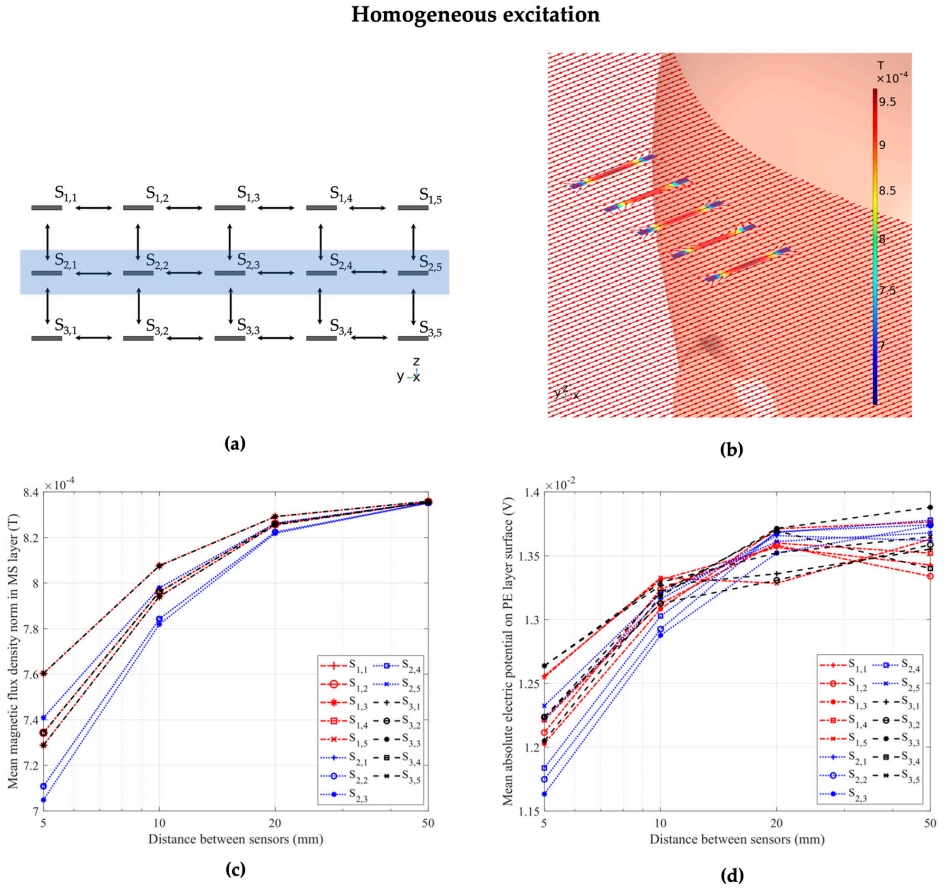

Figure 5. (**a**) Schematic of the 15-sensor array in top-down and frontal view. The blue rectangle marks the second row of five sensors, which we used to visualize the crosstalk effects between sensors. The distance between sensors in this schematic is 5 mm. (**b**) The 15-sensor array in a homogeneous magnetic field. The magnetic field strength is 1 A/m and is applied in x-direction. The highlighted middle row of five sensors within the array, namely the sensors $S_{2,1}$, $S_{2,2}$, $S_{2,3}$, $S_{2,4}$, and $S_{2,5}$, is shown, with clear crosstalk effects between sensors. The distance between the sensors is 1 cm in this exemplary position. (**c**) The magnetic flux density inside the MS layers and (**d**) the electric potential on the surface of the PE layer of each of the 15 sensors of the array at different distances from adjacent sensors, showcasing crosstalk at small distances between the sensors and increased effects in the central sensors.

Based on the orientation of the dipole and the ME sensor, the sensor response can be vastly different due to its directional sensitivity, as we showed in our previous work with an array of orthogonally oriented ME sensors and different dipole orientations [27]. For this work, we exemplarily investigated only one dipole orientation (y-direction) and one sensor orientation for each sensor in the array (x-direction), but modifications to this model with arbitrary configurations for arrays and sources are possible for further analysis. The dipole can be configured with an arbitrary dipole moment direction, amplitude, and location in the head. We chose an exemplary dipole moment of 1 mA·m in y-direction. The chosen dipole amplitude is in agreement with studies on deep brain stimulation (DBS) and head models from the literature [32,40]. As seen in previous investigations, it is not trivial to predict the behavior of the sensor array when excited by an inhomogeneous magnetic field.

Sensors **2024**, *24*, 1186

As seen in Figure 6, the individual sensors' magnetic and electric behavior does not follow specific patterns with increasing distance to neighbors. Some indicators can partly predict the behavior; for example, the fact that in the vertical array configuration, the bottom row of sensors exhibits a higher magnetic flux density based on proximity to the human head and the magnetic field propagation through the tissue. In this case, all five sensors in the bottom row of sensors ($S_{3,1}$–$S_{3,5}$) exhibited the highest magnetic and electric response at distances of between 5 mm and 1 cm between adjacent sensors. Similarly, four out of the five sensors ($S_{3,1}$–$S_{3,4}$) and three out of the four sensors ($S_{3,2}$–$S_{3,4}$) with the highest magnetic flux density and electric potential at distances of 2 cm and 5 cm from their neighbors, respectively, are sensors from the bottom row of the array.

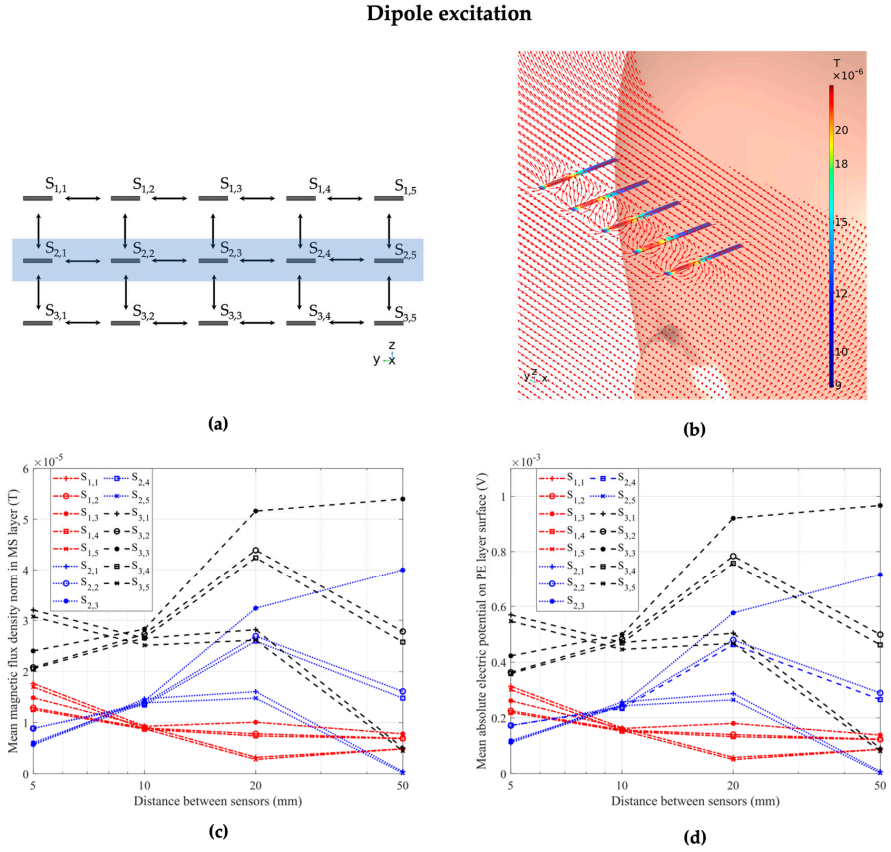

Figure 6. (**a**) Schematic of the 15-sensor array in top-down and frontal view. The blue rectangle marks the second row of five sensors, which we used to visualize the crosstalk effects between sensors. The distance between sensors in this schematic is 5 mm. (**b**) The 15-sensor array in a dipole magnetic field. The dipole moment is 1 mA·m in magnitude and oriented in y-direction. The highlighted middle row of five sensors within the array, namely the sensors $S_{2,1}$, $S_{2,2}$, $S_{2,3}$, $S_{2,4}$, and $S_{2,5}$, is shown, with possible crosstalk and flux concentration effects between sensors. The distance between the sensors is 1 cm in these exemplary positions. (**c**) The magnetic flux density inside the MS layers and (**d**) the electric potential on the surface of the PE layer of each of the 15 sensors of the array at different distances from adjacent sensors, showcasing an increased sensor response in the bottom row of sensors in the array ($S_{3,1}$–$S_{3,5}$), but inconsistent behavior with increasing sensor distance.

4. Discussion

Magnetic crosstalk effects between the adjacent ME sensors are clearly observed for the homogeneous excitation case in Figure 5; they are more challenging to visualize for the inhomogeneous case in Figure 6 with a strong spatial variation of the magnetic field strength and direction. To gain a better understanding of the observed results, we

investigated the sensor sensitivity. As the ME sensor has a previously demonstrated directional sensitivity [27], we investigated the effect of the x-component of the magnetic field, which is parallel to the cantilever's long axis. We calculated two ratios between important model parameters in order to discuss the presented sensor behavior in both homogeneous and inhomogeneous excitation cases. The first ratio was between the mean absolute B_x component of the magnetic flux density inside the MS layer of the sensor, and the same layer with its material parameters set to those of air. The second ratio was between the mean absolute electric potential as the electric sensor response and the B_x component of the magnetic flux density inside the magnetostrictive layer of each sensor. Figure 7a,b demonstrate the results for the ratios between sensor and air magnetic flux densities, while Figure 7c,d visualize the ratios between electric potential and sensor magnetic flux density for both excitation cases and each individual sensor inside the array. Here, the horizontal axis determines the sensor number with horizontally adjacent sensor columns ($S_{1,n}$–$S_{1,n}$), while the markers differentiate between the vertically adjacent rows of sensors ($S_{m,1}$–$S_{m,3}$), as illustrated in Figures 5a and 6a. The four different colors represent the different distances between adjacent sensors, with distances of 5 mm, 1 cm, 2 cm, and 5 cm in the horizontal and vertical directions, respectively. The results show that, while we observe magnetic flux densities and piezoelectric voltages that are highly dependent on the sensor position and distance to its neighbors in both homogeneous and inhomogeneous excitation, the ratio between electric response and excitation field was near constant for each excitation case.

As seen in Figure 7a,b, the ratio between the magnetic flux densities inside the sensor geometry and the corresponding air volumes were not constant with up to two orders of magnitude in the homogeneous and four orders of magnitude in the inhomogeneous case between the ratios at different sensor positions. This large spread showcases the field concentration effect of the magnetostrictive material and highly position-dependent behavior of the sensors. Contrary to the highly variable ratios between the magnetic flux densities, Figure 7c illustrates a narrow range of values between 16.0 and 16.6 for the ratio between electric potential and magnetic flux density for the homogeneous excitation case and any sensor at the investigated array positions and distances. For the inhomogeneous case, Figure 7d shows different behavior between the middle row of sensors (Row 2, $S_{2,1}$–$S_{2,5}$) at a distance of 5 mm between adjacent sensors and every other configuration. A factor between 17.4 and 18.0 was calculated for every sensor position, with outliers for the first and last sensor in the second row ($S_{2,1}$ and $S_{2,5}$) at a distance of 5 cm exhibiting a factor of approximately 19.0.

The entire second row of sensors ($S_{2,1}$–$S_{2,5}$) at the minimum distance of 5 mm between sensors exhibited a factor between 19.5 and 19.7. Despite the outlying row of sensors in the inhomogeneous case, all 15 sensors in either homogeneous or dipole excitation fields exhibited similar, near-constant ratios between the electric response and the magnetic excitation. Considering the clear crosstalk effects demonstrated for the homogeneous case in Figure 5 and the seemingly inconsistent behavior in dipole excitation seen in Figure 6, with up to two orders of magnitude difference in magnetic flux density between different sensor positions in Figure 6c, these near-constant ratios demonstrated a highly linear relation between the excitation magnetic field and the electric sensor response, including potential crosstalk and flux concentration effects. Therefore, the change in the electric sensor response may be attributed to the change in the magnetic field in the sensor.

Sensors **2024**, *24*, 1186

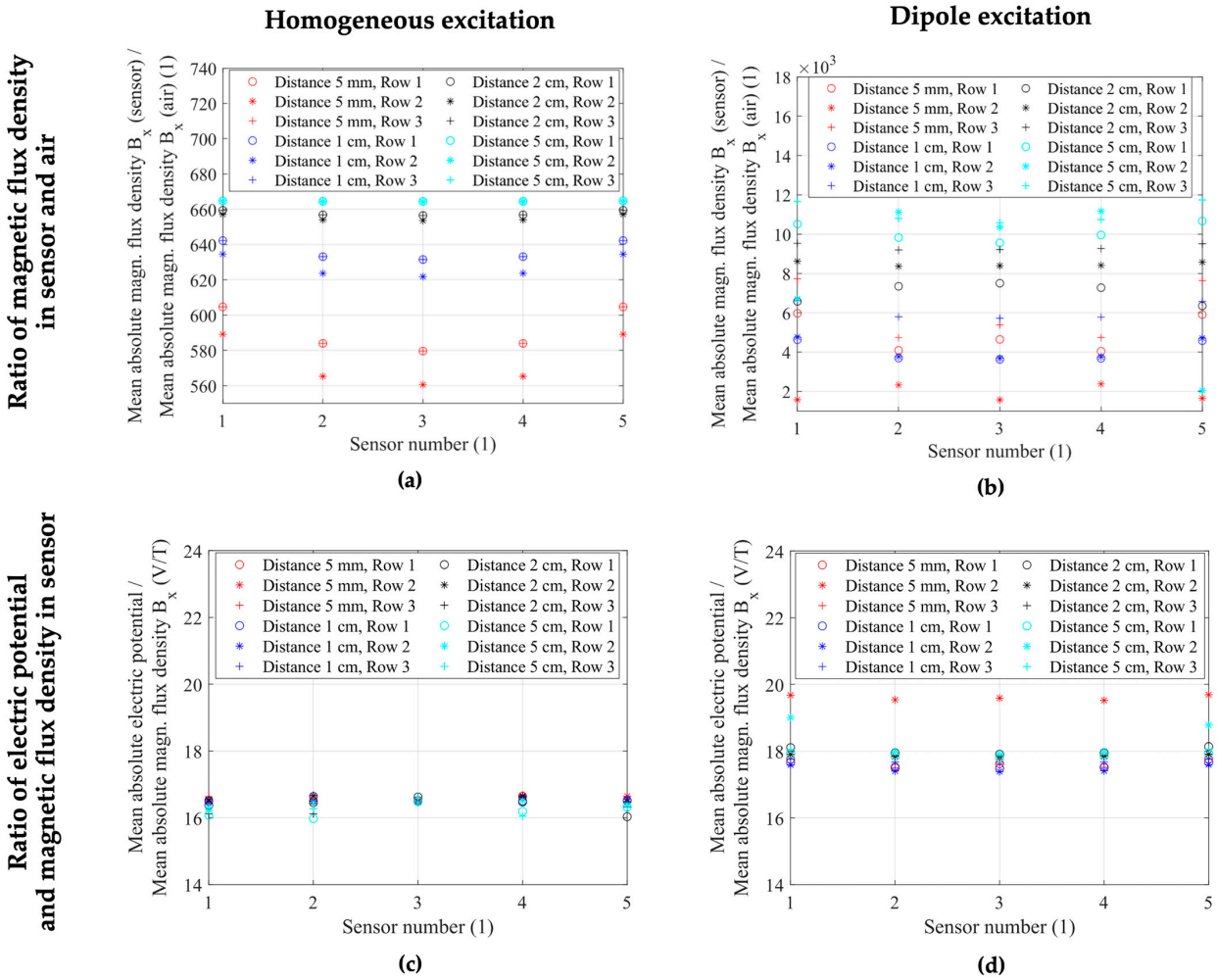

Figure 7. (**a**,**b**)The ratio between the mean absolute x-component of the magnetic flux density inside the MS layer geometry for sensor material parameters and sensor material parameters set to air in (**a**) homogeneous and (**b**) dipole excitation cases. This ratio is a measure of the field concentration and depends on the sensor position in the array. (**c**,**d**) The ratio between the mean absolute electric potential over the PE layer and the mean absolute magnetic flux density component in *x*-direction in each sensor of the array and for different distances between adjacent sensors. (**c**) illustrates the near-constant factors between 16.0 and 16.6 for the ratio for each sensor and each position within the array in homogeneous excitation. (**d**) shows a factor between 17.4 and 18.0 for most sensors, with the outlying second row of sensors ($S_{2,1}$–$S_{2,5}$) at the minimum distance of 5 mm between adjacent sensors exhibiting a factor between 19.5 and 19.7.

5. Conclusions

We have shown a combined ME sensor array and MRI-based human head model for joint biomagnetic field simulations and analysis of ME sensor behavior. The combined model allowed us to place an electric dipole source inside the head and simulate the excitation and propagation of an electromagnetic field through the head's tissue regions, the air environment, and into the array of ME sensors. As an alternative study step to the dipole excitation, a homogeneous excitation field was also applied to the entire simulation environment and the sensor responses were evaluated.

The results that we presented offer insights on the response of individual ME sensors within an array configuration to different excitation mechanisms. For an array of 15 ME

sensors in a homogeneous magnetic excitation field, a magnetic crosstalk effect between adjacent sensors is clearly visible in Figure 5. The magnitude of this effect decreases with increasing distance between adjacent sensors and becomes negligible at a distance of 5 cm. In the case of inhomogeneous excitation, a strong change in the sensor response is obtained as seen in Figure 6 due to the position-dependent magnetic field strength and direction. The sensor response, in this case, depends on the position and orientation of the array relative to the source inside the head, as well as the propagation of the electromagnetic field through the head based on the electric tissue properties and geometry of the head [27]. In excitation fields that have large vector components in directions other than the sensitive direction of the ME sensor, differences between sensor positions may be more pronounced, as opposed to a homogeneous excitation field in a sensitive direction, which is demonstrated in this study. Another effect that has to be considered is the inverse magnetostrictive effect, which is caused by strain in the magnetostrictive layer and can lead to superimposing local fields on top of the excitation field [34]. This effect could have a varying degree of influence on the behavior of adjacent sensors, particularly in inhomogeneous magnetic fields.

To investigate whether the linear relation between the excitation magnetic field and the electric sensor response is maintained, we calculated the ratio of these quantities for each individual ME sensor in both excitation setups and four different distances between adjacent sensors inside of the array. We demonstrated that even with large differences up to factors of two orders of magnitude in the magnetic and electric sensor responses between sensors in various combinations of array geometry and magnetic field sources, the ratio between the electric potential and magnetic flux density inside the sensors was near-constant in homogeneous (16.0–16.6) and inhomogeneous (17.4–19.7) excitation. This result is shown in Figure 7 and confirms that the behavior of each ME sensor was linear as expected for the linear model, even though a highly position-dependent field concentration is demonstrated. Therefore, for the linear approximation, a separation of the excitation source and sensor model in both homogeneous and inhomogeneous excitation configurations is possible. In the next step, the FEM model can be extended to investigate nonlinear effects due to nonlinear material properties as well as effects due to nonlinear secondary currents induced inside the head.

In summary, this work contains insights into the response of ME sensors within different array configurations for homogeneous and inhomogeneous dipole magnetic field excitation for the small-signal linearized case. The sensor response strongly depends on the excitation vector field and confirms the influence of magnetic crosstalk between sensors. Further research may include additional simulations with different array configurations in inhomogeneous fields to evaluate the near-constant sensitivity of the sensors. Additionally, results could be compared between separately evaluated source and sensor simulations and the sensor response in combined models such as the one presented in this work. Future excitation models could also evolve the head geometry demonstrated in this work to contain more tissue regions in higher resolution, as well as different biological or artificial excitation sources such as implanted DBS electrodes, giving rise to potential localization and orientation investigations with patient- or application-specific head and ME sensor models.

Author Contributions: Conceptualization, M.-Ö.Ö. and M.G.; methodology, M.-Ö.Ö., G.B. and M.G.; validation, M.-Ö.Ö.; investigation, M.-Ö.Ö.; writing—original draft preparation, M.-Ö.Ö.; writing—review and editing, M.-Ö.Ö., G.B. and M.G.; visualization, M.-Ö.Ö. and G.B.; supervision, M.G.; funding acquisition, M.G. All authors have read and agreed to the published version of the manuscript.

Funding: This work was funded by the German Research Foundation (Deutsche Forschungsgemeinschaft, DFG) via the collaborative research center CRC 1261 "Magnetoelectric Sensors: From Composite Materials to Biomagnetic Diagnostics".

Data Availability Statement: The data that the findings of this work are based on are available from the corresponding authors upon reasonable request.

Conflicts of Interest: The authors declare no conflict of interest. The funders had no role in the design of the study; in the collection, analyses, or interpretation of data; in the writing of the manuscript; or in the decision to publish the results.

Appendix A. Material Parameters

The material parameters of AlN, FeCoSiB, and silicon at the working point used for the ME sensor are based on literature and in-house characterization and are given in this section [35,41–43].

AlN:

$$c_{E,\mathrm{AlN}} = \begin{pmatrix} 41 & 14.9 & 9.9 & 0 & 0 & 0 \\ 14.9 & 41 & 9.9 & 0 & 0 & 0 \\ 9.9 & 9.9 & 38.9 & 0 & 0 & 0 \\ 0 & 0 & 0 & 12.5 & 0 & 0 \\ 0 & 0 & 0 & 0 & 12.5 & 0 \\ 0 & 0 & 0 & 0 & 0 & 12.5 \end{pmatrix} \times 10^{10}\ \mathrm{Pa} \tag{A1}$$

$$e_{ES,\mathrm{AlN}} = \begin{pmatrix} 0 & 0 & 0 & 0 & -0.48 & 0 \\ 0 & 0 & 0 & -0.48 & 0 & 0 \\ 9.9 & 9.9 & 38.9 & 0 & 0 & 0 \\ -0.58 & -0.58 & 1.55 & 0 & 0 & 0 \end{pmatrix} \times \mathrm{C/m^2} \tag{A2}$$

$$\rho_{\mathrm{AlN}} = 3300\ \mathrm{kg/m^3} \tag{A3}$$

$$\varepsilon_{\mathrm{AlN}} = 80 \times 10^{-12}\ \mathrm{F/m} \tag{A4}$$

$$\mu_{\mathrm{AlN}} = 0.4\pi \times 10^{-6}\ \mathrm{H/m} \tag{A5}$$

FeCoSiB:

$$c_{H,\mathrm{FeCoSiB}} = \begin{pmatrix} 150 & 45 & 45 & 0 & 0 & 0 \\ 45 & 150 & 45 & 0 & 0 & 0 \\ 45 & 45 & 150 & 0 & 0 & 0 \\ 0 & 0 & 0 & 40 & 0 & 0 \\ 0 & 0 & 0 & 0 & 40 & 0 \\ 0 & 0 & 0 & 0 & 0 & 40 \end{pmatrix} \times 10^{10}\ \mathrm{Pa} \tag{A6}$$

$$e_{HS,\mathrm{FeCoSiB}} = \begin{pmatrix} 8500 & -2833.3 & -2833.3 & 0 & 0 & 0 \\ 0 & 0 & 0 & 0 & 0 & 0 \\ 0 & 0 & 0 & 0 & 0 & 0 \\ 0 & 0 & 0 & 0 & 0 & 0 \end{pmatrix} \times \mathrm{N/(Am)} \tag{A7}$$

$$\rho_{\mathrm{FeCoSiB}} = 7250\ \mathrm{kg/m^3} \tag{A8}$$

$$\varepsilon_{\mathrm{FeCoSiB}} = 8.85 \times 10^{-12}\ \mathrm{F/m} \tag{A9}$$

$$\mu_{\mathrm{FeCoSiB}} = 1.13 \times 10^{-3}\ \mathrm{H/m} \tag{A10}$$

Silicon:

$$E_{\mathrm{Si}} = 170 \times 10^{9}\ \mathrm{Pa} \tag{A11}$$

$$\nu_{\mathrm{Si}} = 0.28 \tag{A12}$$

$$\rho_{\mathrm{Si}} = 2329\ \mathrm{kg/m^3} \tag{A13}$$

$$\varepsilon_{\mathrm{Si}} = 103.59 \times 10^{-12}\ \mathrm{F/m} \tag{A14}$$

$$\mu_{\mathrm{Si}} = 0.4\pi \times 10^{-6}\ \mathrm{H/m} \tag{A15}$$

Appendix B. Mesh Parameters for Original 3-Sensor Array Model

Head and sensor model geometry parameters for a model with 3 ME sensors [27]. The mesh is designed so that extremely thin layers of PE and MS material are of a suffi-

ciently small size, while larger structures such as the head and airbox are allowed larger element sizes to decrease the total number of degrees of freedom and therefore the computational load for the simulations. Values given are for the longest edges of tetrahedral mesh elements.

Mesh Parameter	PE and MS Layer	Substrate Layer	Skin	Skull	White Matter	Airbox
Max. element size	5.00×10^{-4} m	1.00×10^{-3} m	5.25×10^{-2} m	5.25×10^{-2} m	5.25×10^{-2} m	3.61×10^{-2} m
Min. element size	9.00×10^{-5} m	1.00×10^{-4} m	1.00×10^{-3} m	1.00×10^{-3} m	1.00×10^{-3} m	1.00×10^{-3} m
Max. element growth rate	3	3	1.45	1.45	1.45	1.4
Curvature factor	0.3	0.3	0.5	0.5	0.5	0.4
Resolution of narrow regions	3	3	0.6	0.6	0.6	0.7

Appendix C. Mesh Parameters for Modified 15-Sensor Array Model

In order to be able to run simulations with the computationally highly demanding 15-sensor array model on our hardware, modifications to the mesh parameters given in Appendix B had to be made. The following table includes the modified minimum element sizes for the substrate layer, the head geometry, and the surrounding air volume. The sensors' piezoelectric and magnetostrictive layers remain unchanged.

Mesh Parameter	PE and MS Layer	Substrate Layer	Skin	Skull	White Matter	Airbox
Max. element size	5.00×10^{-4} m	1.00×10^{-3} m	5.25×10^{-2} m	5.25×10^{-2} m	5.25×10^{-2} m	3.61×10^{-2} m
Min. element size	9.00×10^{-5} m	3.00×10^{-4} m	6.56×10^{-3} m	6.56×10^{-3} m	6.56×10^{-3} m	2.63×10^{-3} m
Max. element growth rate	3	3	1.45	1.45	1.45	1.4
Curvature factor	0.3	0.3	0.5	0.5	0.5	0.4
Resolution of narrow regions	3	3	0.6	0.6	0.6	0.7

References

1. Muthuraman, M.; Moliadze, V.; Mideksa, K.G.; Anwar, A.R.; Stephani, U.; Deuschl, G.; Freitag, C.M.; Siniatchkin, M. EEG-MEG Integration Enhances the Characterization of Functional and Effective Connectivity in the Resting State Network. *PLoS ONE* **2015**, *10*, e0140832. [CrossRef]
2. Primdahl, F. The fluxgate magnetometer. *J. Phys. E* **1979**, *12*, 241–253. [CrossRef]
3. Auster, H.U.; Glassmeier, K.H.; Magnes, W.; Aydogar, O.; Baumjohann, W.; Constantinescu, D.; Fischer, D.; Fornacon, K.H.; Georgescu, E.; Harvey, P.; et al. The THEMIS Fluxgate Magnetometer. *Space Sci. Rev.* **2008**, *141*, 235–264. [CrossRef]
4. Jodko-Władzińska, A.; Wildner, K.; Pałko, T.; Władziński, M. Compensation System for Biomagnetic Measurements with Optically Pumped Magnetometers inside a Magnetically Shielded Room. *Sensors* **2020**, *20*, 4563. [CrossRef] [PubMed]
5. Wikswo, J.P. SQUID magnetometers for biomagnetism and nondestructive testing: Important questions and initial answers. *IEEE Trans. Appl. Supercond.* **1995**, *5*, 74–120. [CrossRef]
6. Galopin, N.; Mininger, X.; Bouillault, F.; Daniel, L. Finite Element Modeling of Magnetoelectric Sensors. *IEEE Trans. Magn.* **2008**, *44*, 834–837. [CrossRef]
7. Reermann, J.; Durdaut, P.; Salzer, S.; Demming, T.; Piorra, A.; Quandt, E.; Frey, N.; Höft, M.; Schmidt, G. Evaluation of magnetoelectric sensor systems for cardiological applications. *Measurement* **2018**, *116*, 230–238. [CrossRef]
8. Zuo, S.; Schmalz, J.; Ozden, M.-O.; Gerken, M.; Su, J.; Niekiel, F.; Lofink, F.; Nazarpour, K.; Heidari, H. Ultrasensitive Magnetoelectric Sensing System for Pico-Tesla MagnetoMyoGraphy. *IEEE Trans. Biomed. Circuits Syst.* **2020**, *14*, 971–984. [CrossRef]
9. Elzenheimer, E.; Bald, C.; Engelhardt, E.; Hoffmann, J.; Hayes, P.; Arbustini, J.; Bahr, A.; Quandt, E.; Höft, M.; Schmidt, G. Quantitative Evaluation for Magnetoelectric Sensor Systems in Biomagnetic Diagnostics. *Sensors* **2022**, *22*, 1018. [CrossRef]
10. Mandal, P.K.; Banerjee, A.; Tripathi, M.; Sharma, A. A Comprehensive Review of Magnetoencephalography (MEG) Studies for Brain Functionality in Healthy Aging and Alzheimer's Disease (AD). *Front. Comput. Neurosci.* **2018**, *12*, 60. [CrossRef]
11. Yalaz, M.; Noor, M.S.; McIntyre, C.C.; Butz, M.; Schnitzler, A.; Deuschl, G.; Höft, M. DBS electrode localization and rotational orientation detection using SQUID-based magnetoencephalography. *J. Neural Eng.* **2021**, *18*, 026021. [CrossRef]
12. Bald, C.; Bergholz, R.; Schmidt, G. Automatic Localization of an Ultrasound Probe with the Help of Magnetic Sensors. *Curr. Dir. Biomed. Eng.* **2022**, *8*, 317–320. [CrossRef]

13. Yalaz, M.; Maling, N.; Deuschl, G.; Juárez-Paz, L.M.; Butz, M.; Schnitzler, A.; Helmers, A.-K.; Höft, M. MaDoPO: Magnetic Detection of Positions and Orientations of Segmented Deep Brain Stimulation Electrodes: A Radiation-Free Method Based on Magnetoencephalography. *Brain Sci.* **2022**, *12*, 86. [CrossRef] [PubMed]
14. Hoffmann, J.; Roldan-Vasco, S.; Krüger, K.; Niekiel, F.; Hansen, C.; Maetzler, W.; Orozco-Arroyave, J.R.; Schmidt, G. Pilot Study: Magnetic Motion Analysis for Swallowing Detection Using MEMS Cantilever Actuators. *Sensors* **2023**, *23*, 3594. [CrossRef]
15. Bibes, M.; Barthélémy, A. Towards a magnetoelectric memory. *Nat. Mater.* **2008**, *7*, 425–426. [CrossRef] [PubMed]
16. Garten, L.M.; Staruch, M.L.; Bussmann, K.; Wollmershauser, J.; Finkel, P. Enhancing Converse Magnetoelectric Coupling Through Strain Engineering in Artificial Multiferroic Heterostructures. *ACS Appl. Mater. Interfaces* **2022**, *14*, 25701–25709. [CrossRef]
17. Liang, X.; Chen, H.; Sun, N.; Luo, B.; Golubeva, E.; Müller, C.; Mahat, S.; Wei, Y.; Dong, C.; Zaeimbashi, M.; et al. Mechanically Driven Solidly Mounted Resonator-Based Nanoelectromechanical Systems Magnetoelectric Antennas. *Adv. Eng. Mater.* **2023**, *25*, 2300425. [CrossRef]
18. Zaeimbashi, M.; Nasrollahpour, M.; Khalifa, A.; Romano, A.; Liang, X.; Chen, H.; Sun, N.; Matyushov, A.; Lin, H.; Dong, C.; et al. Ultra-compact dual-band smart NEMS magnetoelectric antennas for simultaneous wireless energy harvesting and magnetic field sensing. *Nat. Commun.* **2021**, *12*, 3141. [CrossRef]
19. Bichurin, M.; Petrov, R.; Leontiev, V.; Semenov, G.; Sokolov, O. Magnetoelectric Current Sensors. *Sensors* **2017**, *17*, 1271. [CrossRef]
20. Petrov, R.; Leontiev, V.; Sokolov, O.; Bichurin, M.; Bozhkov, S.; Milenov, I.; Bozhkov, P. A Magnetoelectric Automotive Crankshaft Position Sensor. *Sensors* **2020**, *20*, 5494. [CrossRef]
21. Viehland, D.; Wuttig, M.; McCord, J.; Quandt, E. Magnetoelectric magnetic field sensors. *MRS Bull.* **2018**, *43*, 834–840. [CrossRef]
22. Rice, J.K.; Rorden, C.; Little, J.S.; Parra, L.C. Subject position affects EEG magnitudes. *NeuroImage* **2013**, *64*, 476–484. [CrossRef] [PubMed]
23. Vorwerk, J.; Oostenveld, R.; Piastra, M.C.; Magyari, L.; Wolters, C.H. The FieldTrip-SimBio pipeline for EEG forward solutions. *Biomed. Eng. OnLine* **2018**, *17*, 37. [CrossRef]
24. Piastra, M.C.; Nüßing, A.; Vorwerk, J.; Bornfleth, H.; Oostenveld, R.; Engwer, C.; Wolters, C.H. The Discontinuous Galerkin Finite Element Method for Solving the MEG and the Combined MEG/EEG Forward Problem. *Front. Neurosci.* **2018**, *12*, 30. [CrossRef]
25. Huang, M.X.; Mosher, J.C.; Leahy, R.M. A sensor-weighted overlapping-sphere head model and exhaustive head model comparison for MEG. *Phys. Med. Biol.* **1999**, *44*, 423–440. [CrossRef]
26. Özden, M.-Ö.; Teplyuk, A.; Gümüs, Ö.; Meyners, D.; Höft, M.; Gerken, M. Magnetoelectric cantilever sensors under inhomogeneous magnetic field excitation. *AIP Adv.* **2020**, *10*, 025132. [CrossRef]
27. Özden, M.-Ö.; Schmalz, J.; Gerken, M. A Combined Magnetoelectric Sensor and Human Head Model for Biomagnetic FEM Simulations. *IEEE Sens. J.* **2023**, *23*, 30259–30270. [CrossRef]
28. Huang, Y.; Parra, L.C.; Haufe, S. The New York Head—A precise standardized volume conductor model for EEG source localization and tES targeting. *NeuroImage* **2016**, *140*, 150–162. [CrossRef]
29. Haufe, S.; Huang, Y.; Parra, L.C. A highly detailed FEM volume conductor model based on the ICBM152 average head template for EEG source imaging and TCS targeting. In Proceedings of the Annual International Conference of the IEEE Engineering in Medicine and Biology Society, Milan, Italy, 25–29 August 2015; pp. 5744–5747.
30. Hasanyan, D.; Gao, J.; Wang, Y.; Viswan, R.; Li, M.; Shen, Y.; Li, J.; Viehland, D. Theoretical and experimental investigation of magnetoelectric effect for bending-tension coupled modes in magnetostrictive-piezoelectric layered composites. *J. Appl. Phys.* **2012**, *112*, 013908. [CrossRef]
31. Peters, M.J.; de Munck, J.C. The Influence of Model Parameters on the Inverse Solution Based on MEGs and EEGs. *Acta Otolaryngol.* **1991**, *111*, 61–69. [CrossRef]
32. Van Uitert, R.; Weinstein, D.; Johnson, C. Volume Currents in Forward and Inverse Magnetoencephalographic Simulations Using Realistic Head Models. *Ann. Biomed. Eng.* **2003**, *31*, 21–31. [CrossRef]
33. Greve, H.; Woltermann, E.; Quenzer, H.-J.; Wagner, B.; Quandt, E. Giant magnetoelectric coefficients in (Fe90Co10)78Si12B10-AlN thin film composites. *Appl. Phys. Lett.* **2010**, *96*, 182501. [CrossRef]
34. Schmalz, J.; Spetzler, E.; McCord, J.; Gerken, M. Investigation of Unwanted Oscillations of Electrically Modulated Magnetoelectric Cantilever Sensors. *Sensors* **2023**, *23*, 5012. [CrossRef]
35. Gugat, J.L.; Schmalz, J.; Krantz, M.C.; Gerken, M. Magnetic Flux Concentration Effects in Cantilever Magnetoelectric Sensors. *IEEE Trans. Magn.* **2016**, *52*, 7403008. [CrossRef]
36. Blackburn, J.F.; Vopsaroiu, M.; Cain, M.G. Verified finite element simulation of multiferroic structures: Solutions for conducting and insulating systems. *J. Appl. Phys.* **2008**, *104*, 074104. [CrossRef]
37. Guo, M.; Dong, S. A resonance-bending mode magnetoelectric-coupling equivalent circuit. *IEEE Trans. Ultrason. Ferroelectr. Freq. Control* **2009**, *56*, 2578–2586. [CrossRef] [PubMed]
38. Petrov, V.M.; Srinivasan, G.; Bichurin, M.I.; Galkina, T.A. Theory of magnetoelectric effect for bending modes in magnetostrictive-piezoelectric bilayers. *J. Appl. Phys.* **2009**, *105*, 063911. [CrossRef]
39. COMSOL Multiphysics Support. Private Communication, 14 June 2023. Available online: https://www.comsol.de/support (accessed on 6 February 2024).
40. Volkmann, J.; Herzog, J.; Kopper, F.; Deuschl, G. Introduction to the programming of deep brain stimulators. *Mov. Disord.* **2002**, *17*, S181–S187. [CrossRef]

41. Piorra, A.; Jahns, R.; Teliban, I.; Gugat, J.L.; Gerken, M.; Knöchel, R.; Quandt, E. Magnetoelectric thin film composites with interdigital electrodes. *Appl. Phys. Lett.* **2013**, *103*, 032902. [CrossRef]
42. Gugat, J.L.; Krantz, M.C.; Gerken, M. Two-Dimensional Versus Three-Dimensional Finite-Element Method Simulations of Cantilever Magnetoelectric Sensors. *IEEE Trans. Magn.* **2013**, *49*, 5287–5293. [CrossRef]
43. Ludwig, A.; Quandt, E. Optimization of the ΔE-effect in thin films and multilayers by magnetic field annealing. In Proceedings of the IEEE International Digest of Technical Papers on Magnetics Conference, Amsterdam, The Netherlands, 28 April–2 May 2002; p. AE2. [CrossRef]

6.2 Key Findings and Scientific Implications

- ME sensor arrays and MRI-based human head models can be simulated in a combined multiscale and multiphysics FEM model.
- In an array configuration, ME sensors can exhibit significant magnetic crosstalk between adjacent sensors.
- The severity of the crosstalk depends on distance to adjacent sensors, position in the sensor array, and type of excitation field (homogeneous vs inhomogeneous).
- The crosstalk decreases with increasing distance to adjacent sensors and becomes negligible at a distance of 5 cm (corresponding to approximately 20 sensor widths) between sensors for homogeneous excitation, while the case of inhomogeneous excitation exhibits a change in sensor behavior due to the position and orientation of the array relative to the magnetic field source.
- Despite multiple orders of magnitude in difference in magnetic and electric response between sensors, the ratio of electric potential and magnetic flux density in the sensors is near-constant in homogeneous (16.0-16.6) and inhomogeneous (17.4-19.7) excitation for different array configurations.
- A separation of excitation source and sensor array model in homogeneous and inhomogeneous excitation configurations is possible for a linear approximation.
- Future research can utilize separate ME sensor array and human head models for linear approximations or combine them for investigations of nonlinear or secondary effects with application- or patient-specific models.

Chapter 7

Conclusion

This chapter finalizes the dissertation and provides three sections to conclude its content. Firstly, a summary of the key results presented in the main journal publications is given. Then, a section focusing on the discussion of the results follows, before lastly completing this work with an outlook on potential future research topics building upon the results and insights of this dissertation.

7.1 Summary

In summary, this doctoral dissertation aimed to offer a contribution to the scientific progress in the field of ME sensor modeling and simulation. After introducing the topic of this thesis, a brief overview of its fundamentals and utilized methods was given. Following these chapters, the main scientific findings were explained in-depth within three individual peer-reviewed journal articles. These findings were related to (1) the behavior of an ME sensor under localized, inhomogeneous excitation, (2) a combined 3-sensor array and simplified spherical human head model, and (3) a combined sensor and head model including fifteen individual ME sensors in array formation and an anatomically approximated, MRI-based human head. In both the spherical and MRI-based head models, the head itself contained electric point dipoles as excitation sources for magnetic field propagation throughout the tissue, surrounding air environment, and into the sensor geometry. The 3D FEM models presented in this thesis demonstrate the behavior of ME sensors under inhomogeneous magnetic field excitation and offer valuable insights into the behavior of single sensors, sensors in array configurations, and sensors in the presence of different biological tissue types with sources located within them.

In Chapter 4, the publication entitled *Magnetoelectric Cantilever Sensors Under Inhomogeneous Magnetic Field Excitation* is presented. The work showed that for a single ME sensor, which is locally excited with a small coil at different positions along its long axis, the location of maximum sensitivity is approximately 4 mm or 17% of the free length away from the fixed end of the cantilever [68]. This insight has implications for calculations that previously assumed the sensitivity to be in the geometrical center of the sensor, uniformly distributed along its length, or even the extreme approximation of the sensor behaving as a point sensor. Applying the

findings from this study to algorithms used in, for example, localization applications, an increase in accuracy could be expected when trying to obtain the precise location of an electromagnetic source.

Another key finding is the behavior of three orthogonally placed ME sensors adjacent to a simplified human head model containing an electric dipole source. The article discussing this is presented in Chapter 5 and is entitled *A Combined Magnetoelectric Sensor and Human Head Model for Biomangetic FEM Simulations*. Here, several simulations were performed, and the sensor behavior investigated for various different parameters such as sensor position and orientation, distance from the head, dipole position inside the head and dipole orientation. The investigation highlighted the strong directional sensitivity of the sensors and listed benefits in accuracy and specificity when combining a head model with three tissue types and realistic material parameters with an ME sensor model [69].

Finally, in a progressive extension of the previous model's framework, the last study entitled *A Combined Magnetoelectric Sensor Array and MRI-Based Human Head Model for Biomagnetic FEM Simulation and Sensor Crosstalk Analysis* is presented in Chapter 6. It focuses on an array of 15 ME sensors, increasing the number of simultaneously simulated sensors by a factor of 5. In addition to that, the head model evolved from a simple spherical model to an approximated anatomical model based on real MRI recordings of the human head geometry. The investigation also involved a dipole source inside the white matter region of the head, with the magnetic field propagating through the tissues of the head and into the surrounding air environment. The focus here was on the behavior of adjacent ME sensors at different horizontal and vertical distances to their neighbors. Depending on their position in the array and distance to the adjacent sensors, significant magnetic crosstalk effects of up to 15.6% lower magnetic response at a close distance of 5 mm could be reported, while the effects diminished at distances up to 5 cm within an applied homogeneous excitation field. Additionally, near-constant sensitivities for each sensor at different array positions were demonstrated in homogeneous and inhomogeneous excitation settings despite strong crosstalk effects, confirming the sensor model's linear behavior [39].

7.2 Discussion

The published works presented in Chapters 4, 5, and 6 range from studying the behavior of a single ME sensor, over arrays of ME sensors, and to the response of arrays of ME sensors in the presence of excitation sources located within multiple layers of biological tissue. Their aim is to answer the specific scientific questions posed in each work, providing novel insights into the operation of the sensing devices in inhomogeneous magnetic fields. These studies, however, are not separate investigations with drastically different models, but rather represent an evolution of models with the goal of tackling new research questions after answering the previous ones. Naturally within this process, some of the questions that emerge will require further studying and discussion in order to reach conclusive explanations.

The study presented in Chapter 4 investigates the localized excitation of a sin-

gle ME sensor with a small coil, both theoretically with an FEM model, as well as experimentally trough a laboratory measurement of a functional ME sensor [68]. The results confirmed the expected existence of a region of higher sensitivity along the long axis of the sensor. While this important observation provides novel insights into the response of ME sensors, it has the potential to be further evaluated (e.g., for different angles, distances, or number of excitation coils). Practical applications will be required to algorithmically implement the learnings of FEM simulations to create a benefit and increase measurement performance, e.g., for use in localization algorithms. Therefore, translating the theoretical findings of this work to practical implementations is key and may lead to a substantial enhancement for biomagnetic sensing applications.

For Chapter 5, the concept of inhomogeneous magnetic excitation fields and the investigation of the sensor response in such fields is further advanced [69]. Instead of a simple copper coil around the sensor as an excitation mechanism, a multi-layer spherical human head model is introduced and contains an electrical dipole source, inducing a magnetic field for sensor excitation. In addition to that, an array of three orthogonal ME sensors is evaluated for sensor directionality and dependence on dipole source orientation. This work provides important insights into the sensor response in presence of a source that is contained in biological tissue and can be detected at different positions and varying orientations within the head. While providing important insights into the response of ME sensors in inhomogeneous magnetic fields propagating from biological tissue, the head model itself is simplified and does not behave precisely the same way as a human head would. As opposed to the first publication, experimental results could not be performed in this work. However, the nature of the simplified head model could present a valuable opportunity to construct an improved multi-layer head phantom and take accompanying measurements with an array of ME sensors for validation of the simulated results, following and building upon the approach of previous experimental evaluations with simple head phantoms [70].

Chapter 6 presents the third and final published journal article contributing to this dissertation. The work detailed in this article represents a direct evolution and further development of many aspects shown in the previous publication. Most notably, the human head model used in this study advances from a simple model with three spherical compartments into a more realistic anatomical head based on MRI data. In addition to that, the number of concurrently simulated ME sensors in this model increases by a factor of 5 to now 15 total sensors in an array configuration [39]. The model described in this publication is extensive and includes multiscale simulations with several sensors in conjunction with highly complex, imported geometries. While resulting in valuable and novel theoretical insights, models such as this are challenging to reproduce in an experimental measurement setup, due to technical limitations such as the large number of ME sensors used, the variable array configurations, and the adjustable excitation source located within a complex head geometry. Experimental studies with real sensors and head phantoms of this complexity were not within the scope of this dissertation. Therefore, when discussing these results, it is advisable to keep in mind that experimental validation is valuable and should be a priority in future investigations. Confirming the simulated results with experimental studies on ME sensor

array behavior could have strong and lasting impact on clinical applications and research projects involving increasing numbers of ME sensors used in array configurations. Until such confirmation of the simulated results is achieved experimentally, the behavior of the sensor array reported in this work remains a theoretical model of the real sensor response. Based on the good agreement between simulated and measured results presented in the first publication, however, results for the simulated ME sensor responses from the successive works presented here are expected to be reliable predictions for future measurement responses in related experiments.

Overall, three key takeaways can be cemented to summarize this discussion section. Firstly, the results presented in this work provide important theoretical insights from a modeling and simulation point of view. In order to improve actual measurement results, close cooperation between theoretical investigators and application developers is required to implement learnings from simulations into measurement setups. Secondly, it is advised to continuously perform simulations and develop models for ME devices used in sensing applications, as results may vary depending on parameters such as different sensor types, materials, boundary conditions, or excitation mechanisms. It is therefore important to include not only the ME sensor alone in a model, but also perform studies considering relevant environments, such as adjacent objects like human tissue, excitation devices like DBS electrodes, or neighboring sensors in an array to evaluate their effects. Thorough modeling of multiscale systems enables evaluating effects such as linear vs non-linear behavior of its components and potential separability, e.g., between ME sensor and excitation source models. And lastly, theoretical investigations should, whenever possible, be accompanied by lab measurements to validate theoretical and experimental results continuously and bilaterally. These continuous checks and validations aid in confirming sensor behavior in models as well as measurements and enable the development of optimal sensing configurations for real-world applications.

7.3 Outlook

While the previously summarized works contain important and novel insights on the theoretical behavior of ME sensors, there are yet more investigations to conduct in future research projects. One main goal should be to verify simulated results with experimental measurements of the same setup, as discussed and underscored in the previous section. While this additional experimental validation was performed for one of the models with a good fit [68], experiments with human heads or head phantoms and functional ME sensors or arrays of ME sensors were out of scope of this dissertation. In the future, functional and robust ME sensors could be combined with custom head phantoms to compare theoretical results and practical experiments. In conjunction with a head phantom for practical ME sensor measurements, the use of DBS electrodes as excitation sources and comparison with the corresponding combined FEM model could give further insights into the behavior of different sources and sensor responses, as well as necessary validation for both theory and experiment. Another approach for future research would be expanding the sensor model to include different types

of ME sensors or operation principles, such as ΔE-effect sensors, SAW sensors, or converse resonators [71]. For clinical applications, different array configurations may be highly interesting, such as concave arrays of ME sensor that can be variably arranged in a cap or helmet structure to align with the scalp's surface. In advanced studies, even custom-designed arrays could be implemented based on patient MRI data and simulated in complement to 3D-printed cast structures for individualized sensor positioning in patient measurements [72]. The models presented in this dissertation could further be utilized to investigate effects based on nonlinear secondary currents inside the tissue regions of the head, or expand the linear model to include nonlinear material parameters and investigate possible effects related to such materials [39].

In conclusion, this dissertation contributed novel 3D FEM numerical simulation models for the theoretical investigation of ME sensors in various sensor and source configurations to its scientific field. New insights are presented regarding the localized and directional sensitivity at different excitation frequencies, the joint simulation of a human head and ME sensor array geometry with simplified and anatomical head models, and lastly, the analysis of up to 15 individual ME sensors in an array configuration, demonstrating significant magnetic crosstalk effects but near-constant sensitivity between the sensors. These investigations and their resulting insights on ME sensor behavior offer a strong foundation upon which future scientific work can be built and advanced modeling and simulation projects can be further developed.

Bibliography

[1] Emil Du Bois-Reymond. Untersuchungen über thierische Elektricität. *Annalen der Physik*, 151(11):463–464, January 1848. ISSN 0003-3804, 1521-3889. doi:10.1002/andp.18481511120. URL https://onlinelibrary.wiley.com/doi/10.1002/andp.18481511120.

[2] Jean-Baptiste Biot and Félix Savart. Note sur le magnétisme de la pile de Volta. *Ann. Chem. Phys.*, 15(222), 1820.

[3] Herman Erlichson. The experiments of Biot and Savart concerning the force exerted by a current on a magnetic needle. *American Journal of Physics*, 66(5): 385–391, May 1998. ISSN 0002-9505, 1943-2909. doi:10.1119/1.18878. URL https://pubs.aip.org/ajp/article/66/5/385/1039797/The-experiments-of-Biot-and-Savart-concerning-the.

[4] Borís Burle, Laure Spieser, Clémence Roger, Laurence Casini, Thierry Hasbroucq, and Franck Vidal. Spatial and temporal resolutions of EEG: Is it really black and white? A scalp current density view. *International Journal of Psychophysiology*, 97(3):210–220, September 2015. ISSN 01678760. doi:10.1016/j.ijpsycho.2015.05.004. URL https://linkinghub.elsevier.com/retrieve/pii/S0167876015001865.

[5] Joao Ribeiro Pinto, Jaime S. Cardoso, and Andre Lourenco. Evolution, Current Challenges, and Future Possibilities in ECG Biometrics. *IEEE Access*, 6:34746–34776, 2018. ISSN 2169-3536. doi:10.1109/ACCESS.2018.2849870. URL https://ieeexplore.ieee.org/document/8392675/.

[6] Maria Peters, John Crowe, Jean-Francois Piéri, Hendrik Quartero, Barrie Hayes-Gill, David James, Jeroen Stinstra, and Simon Shakespeare. Monitoring the fetal heart non-invasively: a review of methods. *Journal of Perinatal Medicine*, 29(5), January 2001. ISSN 0300-5577. doi:10.1515/JPM.2001.057. URL https://www.degruyter.com/document/doi/10.1515/JPM.2001.057/html.

[7] J.P. Wikswo. SQUID magnetometers for biomagnetism and nondestructive testing: important questions and initial answers. *IEEE Transactions on Appiled Superconductivity*, 5(2):74–120, June 1995. ISSN 10518223. doi:10.1109/77.402511. URL http://ieeexplore.ieee.org/document/402511/.

[8] Pravat K. Mandal, Anwesha Banerjee, Manjari Tripathi, and Ankita Sharma. A Comprehensive Review of Magnetoencephalography (MEG) Studies for Brain Functionality in Healthy Aging and Alzheimer's Disease (AD). *Fron-*

tiers in Computational Neuroscience, 12:60, August 2018. ISSN 1662-5188. doi:10.3389/fncom.2018.00060. URL https://www.frontiersin.org/article/10.3389/fncom.2018.00060/full.

[9] Mevlüt Yalaz, M Sohail Noor, Cameron C McIntyre, Markus Butz, Alfons Schnitzler, Günther Deuschl, and Michael Höft. DBS electrode localization and rotational orientation detection using SQUID-based magnetoencephalography. *Journal of Neural Engineering*, 18(2):026021, April 2021. ISSN 1741-2560, 1741-2552. doi:10.1088/1741-2552/abe099. URL https://iopscience.iop.org/article/10.1088/1741-2552/abe099.

[10] Vishal K Shah and Ronald T Wakai. A compact, high performance atomic magnetometer for biomedical applications. *Physics in Medicine and Biology*, 58(22):8153–8161, November 2013. ISSN 0031-9155, 1361-6560. doi:10.1088/0031-9155/58/22/8153. URL https://iopscience.iop.org/article/10.1088/0031-9155/58/22/8153.

[11] Tim M. Tierney, Niall Holmes, Stephanie Mellor, José David López, Gillian Roberts, Ryan M. Hill, Elena Boto, James Leggett, Vishal Shah, Matthew J. Brookes, Richard Bowtell, and Gareth R. Barnes. Optically pumped magnetometers: From quantum origins to multi-channel magnetoencephalography. *NeuroImage*, 199:598–608, October 2019. ISSN 10538119. doi:10.1016/j.neuroimage.2019.05.063. URL https://linkinghub.elsevier.com/retrieve/pii/S1053811919304550.

[12] F Primdahl. The fluxgate magnetometer. *Journal of Physics E: Scientific Instruments*, 12(4):241–253, April 1979. ISSN 0022-3735. doi:10.1088/0022-3735/12/4/001. URL https://iopscience.iop.org/article/10.1088/0022-3735/12/4/001.

[13] H. U. Auster, K. H. Glassmeier, W. Magnes, O. Aydogar, W. Baumjohann, D. Constantinescu, D. Fischer, K. H. Fornacon, E. Georgescu, P. Harvey, O. Hillenmaier, R. Kroth, M. Ludlam, Y. Narita, R. Nakamura, K. Okrafka, F. Plaschke, I. Richter, H. Schwarzl, B. Stoll, A. Valavanoglou, and M. Wiedemann. The THEMIS Fluxgate Magnetometer. *Space Science Reviews*, 141(1-4): 235–264, December 2008. ISSN 0038-6308, 1572-9672. doi:10.1007/s11214-008-9365-9. URL http://link.springer.com/10.1007/s11214-008-9365-9.

[14] Ruslan Rybalko, Jens Haueisen, and Christian Hofmann. New type of fluxgate magnetometer for the heart's magnetic fields detection. *Current Directions in Biomedical Engineering*, 1(1):22–25, September 2015. ISSN 2364-5504. doi:10.1515/cdbme-2015-0006. URL https://www.degruyter.com/document/doi/10.1515/cdbme-2015-0006/html.

[15] Dwight Viehland, Manfred Wuttig, Jeffrey McCord, and Eckhard Quandt. Magnetoelectric magnetic field sensors. *MRS Bulletin*, 43(11):834–840, November 2018. ISSN 0883-7694, 1938-1425. doi:10.1557/mrs.2018.261. URL http://link.springer.com/10.1557/mrs.2018.261.

[16] Mirza Bichurin, Roman Petrov, Oleg Sokolov, Viktor Leontiev, Viktor Kuts, Dmitry Kiselev, and Yaojin Wang. Magnetoelectric Magnetic Field Sen-

sors: A Review. *Sensors*, 21(18):6232, September 2021. ISSN 1424-8220. doi:10.3390/s21186232. URL https://www.mdpi.com/1424-8220/21/18/6232.

[17] Eric Elzenheimer, Christin Bald, Erik Engelhardt, Johannes Hoffmann, Patrick Hayes, Johan Arbustini, Andreas Bahr, Eckhard Quandt, Michael Höft, and Gerhard Schmidt. Quantitative Evaluation for Magnetoelectric Sensor Systems in Biomagnetic Diagnostics. *Sensors*, 22(3):1018, January 2022. ISSN 1424-8220. doi:10.3390/s22031018. URL https://www.mdpi.com/1424-8220/22/3/1018.

[18] Hadi Heidari and Vahid Nabaei. *Magnetic sensors for biomedical applications*. IEEE Press series on sensors. Wiley, Hoboken, New Jersey, 2020. ISBN 978-1-119-55217-8.

[19] Ludwig Bergmann, Clemens Schaefer, and Wilhelm Raith. *Elektromagnetismus*. Walter de Gruyter, August 2006. ISBN 978-3-11-018898-1. doi:10.1515/9783110199284. URL https://www.degruyter.com/document/doi/10.1515/9783110199284/html.

[20] Robert J. Cooper, David W. Prescott, Peter Matz, Karen L. Sauer, Nezih Dural, Michael V. Romalis, Elizabeth L. Foley, Thomas W. Kornack, Mark Monti, and Jeffrey Okamitsu. Atomic Magnetometer Multisensor Array for rf Interference Mitigation and Unshielded Detection of Nuclear Quadrupole Resonance. *Physical Review Applied*, 6(6):064014, December 2016. ISSN 2331-7019. doi:10.1103/PhysRevApplied.6.064014. URL https://link.aps.org/doi/10.1103/PhysRevApplied.6.064014.

[21] D. N. Astrov. The magnetoelectric effect in antiferromagnetics. *Zh. Eksperim. i Teor Fiz,* (*Engl. transl.: Sov. Phys. JETP*), 11(3):708–709, 1960.

[22] W. F. Brown, R. M. Hornreich, and S. Shtrikman. Upper Bound on the Magnetoelectric Susceptibility. *Physical Review*, 168(2):574–577, April 1968. ISSN 0031-899X. doi:10.1103/PhysRev.168.574. URL https://link.aps.org/doi/10.1103/PhysRev.168.574.

[23] John F. Blackburn, Marian Vopsaroiu, and Markys G. Cain. Verified finite element simulation of multiferroic structures: Solutions for conducting and insulating systems. *Journal of Applied Physics*, 104(7):074104, 2008. ISSN 00218979. doi:10.1063/1.2988183. URL http://scitation.aip.org/content/aip/journal/jap/104/7/10.1063/1.2988183.

[24] Manfred Fiebig. Revival of the magnetoelectric effect. *Journal of Physics D: Applied Physics*, 38(8):R123–R152, April 2005. ISSN 0022-3727, 1361-6463. doi:10.1088/0022-3727/38/8/R01. URL https://iopscience.iop.org/article/10.1088/0022-3727/38/8/R01.

[25] Nicola A. Spaldin and Manfred Fiebig. The Renaissance of Magnetoelectric Multiferroics. *Science*, 309(5733):391–392, July 2005. ISSN 0036-8075, 1095-9203. doi:10.1126/science.1113357. URL https://www.science.org/doi/10.1126/science.1113357.

[26] Robert Jahns, Reinhard Knochel, Henry Greve, Eric Woltermann, Enno Lage,

and Eckard Quandt. Magnetoelectric sensors for biomagnetic measurements. In *2011 IEEE International Symposium on Medical Measurements and Applications*, pages 107–110, Bari, Italy, May 2011. IEEE. ISBN 978-1-4244-9336-4. doi:10.1109/MeMeA.2011.5966676. URL http://ieeexplore.ieee.org/document/5966676/.

[27] Robert Jahns, Henry Greve, Eric Woltermann, Eckhard Quandt, and Reinhard Knöchel. Sensitivity enhancement of magnetoelectric sensors through frequency-conversion. *Sensors and Actuators A: Physical*, 183:16–21, August 2012. ISSN 09244247. doi:10.1016/j.sna.2012.05.049. URL https://linkinghub.elsevier.com/retrieve/pii/S0924424712003706.

[28] B. Gojdka, R. Jahns, K. Meurisch, H. Greve, R. Adelung, E. Quandt, R. Knöchel, and F. Faupel. Fully integrable magnetic field sensor based on delta-E effect. *Applied Physics Letters*, 99(22):223502, November 2011. ISSN 0003-6951, 1077-3118. doi:10.1063/1.3664135. URL https://pubs.aip.org/aip/apl/article/123243.

[29] Sebastian Zabel, Jens Reermann, Simon Fichtner, Christine Kirchhof, Eckhard Quandt, Bernhard Wagner, Gerhard Schmidt, and Franz Faupel. Multimode delta-E effect magnetic field sensors with adapted electrodes. *Applied Physics Letters*, 108(22):222401, May 2016. ISSN 0003-6951, 1077-3118. doi:10.1063/1.4952735. URL http://aip.scitation.org/doi/10.1063/1.4952735.

[30] D. Webb, D. Forester, A. Ganguly, and C. Vittoria. Applications of amorphous magnetic-layers in surface-acoustic-wave devices. *IEEE Transactions on Magnetics*, 15(6):1410–1415, November 1979. ISSN 0018-9464. doi:10.1109/TMAG.1979.1060442. URL http://ieeexplore.ieee.org/document/1060442/.

[31] Anne Kittmann, Phillip Durdaut, Sebastian Zabel, Jens Reermann, Julius Schmalz, Benjamin Spetzler, Dirk Meyners, Nian X. Sun, Jeffrey McCord, Martina Gerken, Gerhard Schmidt, Michael Höft, Reinhard Knöchel, Franz Faupel, and Eckhard Quandt. Wide Band Low Noise Love Wave Magnetic Field Sensor System. *Scientific Reports*, 8(1):278, December 2018. ISSN 2045-2322. doi:10.1038/s41598-017-18441-4. URL http://www.nature.com/articles/s41598-017-18441-4.

[32] COMSOL Multiphysics, COMSOL Inc., 2024. URL https://www.comsol.com.

[33] MATLAB, The Mathworks Inc., 2024. URL https://www.mathworks.com.

[34] Gerhard Baule and Richard McFee. Detection of the magnetic field of the heart. *American Heart Journal*, 66(1):95–96, July 1963. ISSN 00028703. doi:10.1016/0002-8703(63)90075-9. URL https://linkinghub.elsevier.com/retrieve/pii/0002870363900759.

[35] Bradley J. Roth. Biomagnetism: The First Sixty Years. *Sensors*, 23(9):4218, April 2023. ISSN 1424-8220. doi:10.3390/s23094218. URL https://www.mdpi.com/1424-8220/23/9/4218.

[36] David Cohen. Magnetic fields around the torso: production by electrical activity of the human heart. *Science*, 156(3775):652–654, 1967.

[37] Matti Hämäläinen, Riitta Hari, Risto J. Ilmoniemi, Jukka Knuutila, and Olli V. Lounasmaa. Magnetoencephalography—theory, instrumentation, and applications to noninvasive studies of the working human brain. *Reviews of Modern Physics*, 65(2):413–497, April 1993. ISSN 0034-6861, 1539-0756. doi:10.1103/RevModPhys.65.413. URL https://link.aps.org/doi/10.1103/RevModPhys.65.413.

[38] Siming Zuo, Julius Schmalz, Mesut-Ömür Özden, Martina Gerken, Jingxiang Su, Florian Niekiel, Fabian Lofink, Kianoush Nazarpour, and Hadi Heidari. Ultrasensitive Magnetoelectric Sensing System for Pico-Tesla MagnetoMyoGraphy. *IEEE Transactions on Biomedical Circuits and Systems*, 14(5):971–984, October 2020. ISSN 1932-4545, 1940-9990. doi:10.1109/TBCAS.2020.2998290. URL https://ieeexplore.ieee.org/document/9102993/.

[39] Mesut-Ömür Özden, Giuseppe Barbieri, and Martina Gerken. A Combined Magnetoelectric Sensor Array and MRI-Based Human Head Model for Biomagnetic FEM Simulation and Sensor Crosstalk Analysis. *Sensors*, 24(4):1186, February 2024. ISSN 1424-8220. doi:10.3390/s24041186. URL https://www.mdpi.com/1424-8220/24/4/1186.

[40] Christin Bald, Robert Bergholz, and Gerhard Schmidt. Automatic Localization of an Ultrasound Probe with the Help of Magnetic Sensors. *Current Directions in Biomedical Engineering*, 8(2):317–320, September 2022. ISSN 2364-5504. doi:10.1515/cdbme-2022-1081. URL https://www.degruyter.com/document/doi/10.1515/cdbme-2022-1081/html.

[41] Mevlüt Yalaz, Nicholas Maling, Günther Deuschl, León M. Juárez-Paz, Markus Butz, Alfons Schnitzler, Ann-Kristin Helmers, and Michael Höft. MaDoPO: Magnetic Detection of Positions and Orientations of Segmented Deep Brain Stimulation Electrodes: A Radiation-Free Method Based on Magnetoencephalography. *Brain Sciences*, 12(1):86, January 2022. ISSN 2076-3425. doi:10.3390/brainsci12010086. URL https://www.mdpi.com/2076-3425/12/1/86.

[42] Johannes Hoffmann, Sebastian Roldan-Vasco, Karolin Krüger, Florian Niekiel, Clint Hansen, Walter Maetzler, Juan Rafael Orozco-Arroyave, and Gerhard Schmidt. Pilot Study: Magnetic Motion Analysis for Swallowing Detection Using MEMS Cantilever Actuators. *Sensors*, 23(7):3594, March 2023. ISSN 1424-8220. doi:10.3390/s23073594. URL https://www.mdpi.com/1424-8220/23/7/3594.

[43] Julius Alexander Schmalz. *Analyse von magnetoelektrischen Sensoren zur Verwendung bei höheren Moden mittels der Finite-Elemente-Methode*. PhD thesis, Christian-Albrechts-Universität zu Kiel, Kiel, 2020.

[44] James Prescott Joule. On a new class of magnetic forces. *Ann. Electrc. Magn. Chem.*, 8(1842):219–224, 1842.

[45] Julian Baumann. *Einspritzmengenkorrektur in Common-Rail-Systemen mit Hilfe*

magnetoelastischer Drucksensoren. PhD thesis, Universität Fridericiana zu Karlsruhe, Karlsruhe, 2006. URL https://publikationen.bibliothek.kit.edu/1000004825. Publisher: [object Object].

[46] Jascha Lukas Gugat. *Entwurf, Analyse und Optimierung magnetoelektrischer Sensoren mit Hilfe der Finite-Elemente-Methode*. PhD thesis, Universität Kiel, Kiel, October 2016.

[47] Bernard D. Cullity and Chad D. Graham. *Introduction to magnetic materials*. IEEE Press, Piscataway, NJ, 2. ed edition, 2009. ISBN 978-0-471-47741-9.

[48] Eckhard Quandt. Giant Magnetostrictive Thin Film Technologies. In *Handbook of Giant Magnetostrictive Materials*, pages 323–343. Elsevier, 2000. ISBN 978-0-12-238640-4. doi:10.1016/B978-012238640-4/50022-X. URL https://linkinghub.elsevier.com/retrieve/pii/B978012238640450022X.

[49] André Piorra. *Ferroelektrische Schichten für magnetoelektrische Komposite*. PhD thesis, Christian-Albrechts-Universität zu Kiel, Kiel, 2014. URL https://macau.uni-kiel.de/servlets/MCRFileNodeServlet/dissertation_derivate_00005455/anpDiss.pdf.

[50] Bernard Jaffe, William R. Jr. Cook, and Hans Jaffe. Piezoelectric Ceramics. In *Piezoelectric Ceramics*, page ii. Academic Press, 1971. ISBN 978-0-12-379550-2. doi:10.1016/B978-0-12-379550-2.50001-6. URL https://linkinghub.elsevier.com/retrieve/pii/B9780123795502500016.

[51] K.-H. Hellwege. *Einführung in die Festkörperphysik*, volume 34 of *Heidelberger Taschenbücher*. Springer Berlin Heidelberg, Berlin, Heidelberg, 1976. ISBN 978-3-540-04864-0 978-3-642-96301-8. doi:10.1007/978-3-642-96301-8. URL http://link.springer.com/10.1007/978-3-642-96301-8.

[52] Walter Borchardt-Ott and Heidrun Sowa. *Kristallographie: eine Einführung für Naturwissenschaftler*. Springer-Lehrbuch. Springer Spektrum, Berlin Heidelberg, 8., überarb. und aktualisierte aufl edition, 2013. ISBN 978-3-642-34810-5.

[53] Will Kleber, Hans-Joachim Bautsch, Joachim Bohm, and Detlef Klimm. *Einführung in die Kristallographie*. Oldenbourg, München, 19., verb. aufl edition, 2010. ISBN 978-3-486-59885-8 978-3-486-59075-3.

[54] Thomas Lottermoser, Thomas Lonkai, Uwe Amann, Dietmar Hohlwein, Jörg Ihringer, and Manfred Fiebig. Magnetic phase control by an electric field. *Nature*, 430(6999):541–544, July 2004. ISSN 0028-0836, 1476-4687. doi:10.1038/nature02728. URL https://www.nature.com/articles/nature02728.

[55] Haribabu Palneedi, Venkateswarlu Annapureddy, Shashank Priya, and Jungho Ryu. Status and Perspectives of Multiferroic Magnetoelectric Composite Materials and Applications. *Actuators*, 5(1):9, March 2016. ISSN 2076-0825. doi:10.3390/act5010009. URL http://www.mdpi.com/2076-0825/5/1/9.

[56] L W Martin, S P Crane, Y-H Chu, M B Holcomb, M Gajek, M Huijben, C-H Yang, N Balke, and R Ramesh. Multiferroics and magnetoelectrics:

thin films and nanostructures. *Journal of Physics: Condensed Matter*, 20 (43):434220, October 2008. ISSN 0953-8984, 1361-648X. doi:10.1088/0953-8984/20/43/434220. URL https://iopscience.iop.org/article/10.1088/0953-8984/20/43/434220.

[57] Michael Link. *Finite Elemente in der Statik und Dynamik*. Springer Fachmedien Wiesbaden, Wiesbaden, 2014. ISBN 978-3-658-03556-3 978-3-658-03557-0. doi:10.1007/978-3-658-03557-0. URL https://link.springer.com/10.1007/978-3-658-03557-0.

[58] Markus Merkel and Andreas Öchsner. *Eindimensionale Finite Elemente: Ein Einstieg in die Methode*. Springer Berlin Heidelberg, Berlin, Heidelberg, 2014. ISBN 978-3-642-54481-1 978-3-642-54482-8. doi:10.1007/978-3-642-54482-8. URL https://link.springer.com/10.1007/978-3-642-54482-8.

[59] Ansys Mechanical, Ansys, Inc., 2024. URL https://www.ansys.com/de-de/products/structures/ansys-mechanical.

[60] CST Studio Suite, Dassault Systèmes., 2024. URL https://www.3ds.com/de/produkte-und-services/simulia/produkte/cst-studio-suite/.

[61] Jascha Lukas Gugat, Matthias C. Krantz, and Martina Gerken. Two-Dimensional Versus Three-Dimensional Finite-Element Method Simulations of Cantilever Magnetoelectric Sensors. *IEEE Transactions on Magnetics*, 49(10):5287–5293, October 2013. ISSN 0018-9464, 1941-0069. doi:10.1109/TMAG.2013.2260346. URL https://ieeexplore.ieee.org/document/6513276/.

[62] Jascha Lukas Gugat, Julius Schmalz, Matthias C. Krantz, and Martina Gerken. Magnetic Flux Concentration Effects in Cantilever Magnetoelectric Sensors. *IEEE Transactions on Magnetics*, 52(5):1–8, May 2016. ISSN 0018-9464, 1941-0069. doi:10.1109/TMAG.2015.2509948. URL http://ieeexplore.ieee.org/document/7360188/.

[63] Robert Hooke. *Lectures de Potentia Restitutiva, Or of Spring Explaining the Power of Springing Bodies*. John Martyn, Cutlerian Lecture 6. edition, 1678.

[64] Jascha Lukas Gugat, Matthias C. Krantz, Julius Schmalz, and Martina Gerken. Signal-to-Noise Ratio in Cantilever Magnetoelectric Sensors. *IEEE Transactions on Magnetics*, 52(9):1–5, September 2016. ISSN 0018-9464, 1941-0069. doi:10.1109/TMAG.2016.2557305. URL http://ieeexplore.ieee.org/document/7460198/.

[65] Mingsen Guo and Shuxiang Dong. A resonance-bending mode magnetoelectric-coupling equivalent circuit. *IEEE Transactions on Ultrasonics, Ferroelectrics and Frequency Control*, 56(11):2578–2586, November 2009. ISSN 0885-3010. doi:10.1109/TUFFC.2009.1346. URL http://ieeexplore.ieee.org/document/5306739/.

[66] V. M. Petrov, G. Srinivasan, M. I. Bichurin, and T. A. Galkina. Theory of magnetoelectric effect for bending modes in magnetostrictive-piezoelectric bilayers. *Journal of Applied Physics*, 105(6):063911, March 2009. ISSN 0021-

8979, 1089-7550. doi:10.1063/1.3087766. URL http://aip.scitation.org/doi/10.1063/1.3087766.

[67] D. Hasanyan, J. Gao, Y. Wang, R. Viswan, M. Li, Y. Shen, J. Li, and D. Viehland. Theoretical and experimental investigation of magnetoelectric effect for bending-tension coupled modes in magnetostrictive-piezoelectric layered composites. *Journal of Applied Physics*, 112(1):013908, July 2012. ISSN 0021-8979, 1089-7550. doi:10.1063/1.4732130. URL http://aip.scitation.org/doi/10.1063/1.4732130.

[68] Mesut-Ömür Özden, Alexander Teplyuk, Ömer Gümüs, Dirk Meyners, Michael Höft, and Martina Gerken. Magnetoelectric cantilever sensors under inhomogeneous magnetic field excitation. *AIP Advances*, 10(2):025132, February 2020. ISSN 2158-3226. doi:10.1063/1.5136239. URL http://aip.scitation.org/doi/10.1063/1.5136239.

[69] Mesut-Ömür Özden, Julius Schmalz, and Martina Gerken. A Combined Magnetoelectric Sensor and Human Head Model for Biomagnetic FEM Simulations. *IEEE Sensors Journal*, 23(24):30259–30270, December 2023. ISSN 1530-437X, 1558-1748, 2379-9153. doi:10.1109/JSEN.2023.3329579. URL https://ieeexplore.ieee.org/document/10313242/.

[70] Mevlut Yalaz, Alexander Teplyuk, Gunther Deuschl, and Michael Hoft. Dipole Fit Localization of the Deep Brain Stimulation Electrode Using 3D Magnetic Field Measurements. *IEEE Sensors Journal*, 20 (16):9550–9557, August 2020. ISSN 1530-437X, 1558-1748, 2379-9153. doi:10.1109/JSEN.2020.2988067. URL https://ieeexplore.ieee.org/document/9068266/.

[71] P. Hayes, M. Jovičević Klug, S. Toxværd, P. Durdaut, V. Schell, A. Teplyuk, D. Burdin, A. Winkler, R. Weser, Y. Fetisov, M. Höft, R. Knöchel, J. McCord, and E. Quandt. Converse Magnetoelectric Composite Resonator for Sensing Small Magnetic Fields. *Scientific Reports*, 9(1):16355, November 2019. ISSN 2045-2322. doi:10.1038/s41598-019-52657-w. URL https://www.nature.com/articles/s41598-019-52657-w.

[72] Elena Boto, Niall Holmes, James Leggett, Gillian Roberts, Vishal Shah, Sofie S. Meyer, Leonardo Duque Muñoz, Karen J. Mullinger, Tim M. Tierney, Sven Bestmann, Gareth R. Barnes, Richard Bowtell, and Matthew J. Brookes. Moving magnetoencephalography towards real-world applications with a wearable system. *Nature*, 555(7698):657–661, March 2018. ISSN 0028-0836, 1476-4687. doi:10.1038/nature26147. URL https://www.nature.com/articles/nature26147.

[73] Mesut-Ömür Özden and Martina Gerken. Trade-off between spatial resolution and sensitivity of magnetoelectric magnetic field sensors. In *2021 International Conference on Electromagnetics in Advanced Applications* (*ICEAA*), pages 124–124, Honolulu, HI, USA, August 2021. IEEE. ISBN 978-1-66541-386-2. doi:10.1109/ICEAA52647.2021.9539722. URL https://ieeexplore.ieee.org/document/9539722/.

[74] Mesut-Ömür Özden and Martina Gerken. A joint magnetoelectric sensor

and human head model for biomagnetic simulation. In *2022 International Conference on Electromagnetics in Advanced Applications (ICEAA)*, pages 021–021, Cape Town, South Africa, September 2022. IEEE. ISBN 978-1-66548-111-3. doi:10.1109/ICEAA49419.2022.9900002. URL https://ieeexplore.ieee.org/document/9900002/.

List of Figures

Acronyms

API Application programming interface

DC Direct current

ECG Electrocardiogram

EEG Electroencephalogram

FEM Finite element method

IDT Interdigital transducer

LOD Limit of detection

MCG Magnetocardiogram

ME Magnetoelectric

MEG Magnetoencephalogram

MMG Magnetomyogram

MRI Magnetic resonance imaging

MS Magnetostrictive

OPM Optically pumped magnetometer

PCB Printed circuit board

PDE Partial differential equation

PE Piezoelectric

POC Point of care

RF Radio frequency

SAW Surface acoustic wave

SQUID Superconducting quantum interference device

Appendix A

Conference Abstracts

This appendix includes the abstracts submitted to the IEEE International Conference on Electromagnetics in Advanced Applications (ICEAA) in 2021 [73] and 2022 [74] respectively, where I presented my research as an invited speaker.

2021 International Conference on Electromagnetics in Advanced Applications (ICEAA) | 978-1-6654-1386-2/21/$31.00 ©2021 IEEE | DOI: 10.1109/ICEAA52647.2021.9539722

Trade-off between spatial resolution and sensitivity of magnetoelectric magnetic field sensors

Mesut-Ömür Özden* (1), Martina Gerken(1)
(1) Kiel University, Kiel, Germany, e-mail: omoz@tf.uni-kiel.de; mge@tf.uni-kiel.de

Magnetoelectric (ME) magnetic field sensors are an aspiring sensor type for the accurate measurement of biomagnetic fields in applications such as magnetocardiography or placing of deep-brain stimulation electrodes. Their design allows measurement of magnetic fields in the low pT-range while offering unique benefits such as unshielded operation and no requirement of additional heating or cooling [1]. In previous work, we demonstrated that cantilever-type ME sensors of strain-coupled magnetostrictive and piezoelectric layers exhibit a strongly position-dependent behavior when excited by inhomogeneous magnetic fields [2]. Here, we investigate in a theoretical study a sensor with reduced magnetostrictive layer size with the aim to increase the spatial resolution.

The response behavior to single-coil excitation of a sensor with full length (Fig. 1(a)) and one eighth of the length covered with magnetostrictive material (Fig. 1(b)) is simulated using the finite element method (FEM) coupling the mechanic, electric, and magnetic behavior. One key result is plotted in Fig. 1(c) showing the mean induced piezoelectric potential. Both sensors are operated at the resonance frequency of 850 Hz. We find that the shorter magnetostrictive layer offers a significant increase in spatial resolution along the longitudinal sensor axis. The absolute value of the generated mean potential on the surface of the piezoelectric layer is two orders of magnitude smaller though compared to a sensor with full magnetostrictive layer length. This may be attributed to the reduced sensor excitation for a shorter magnetostrictive layer as well as to reduced magnetic flux concentration due to the changed geometry.

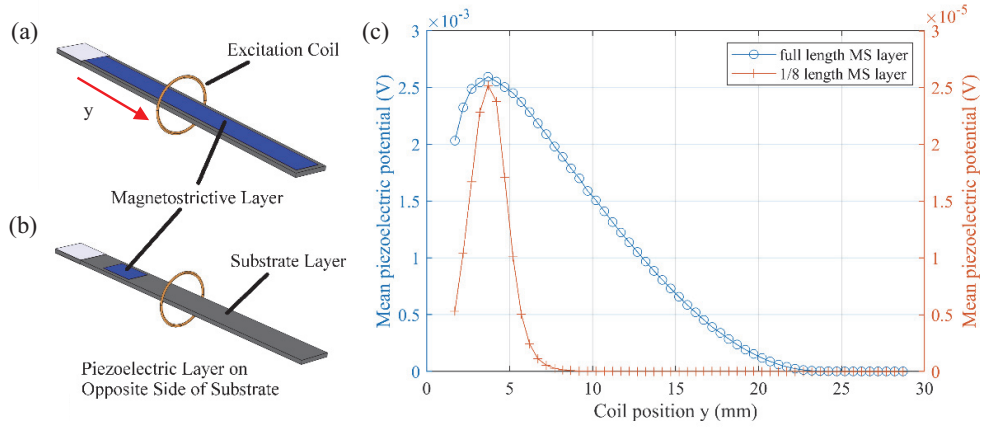

Figure 1. Schematic of sensor with (a) full magnetostrictive (MS) layer (22.90 mm) and (b) one eighth of the original length (2.86 mm) centered at a distance of y = 3.7 mm from clamping. The copper coil is centered at a position of y = 13.125 mm distance from the fixed end. (c) Comparison of simulated mean piezoelectric potential on the surface of the piezoelectric (PE) layer for different positions along the y-axis of a single excitation coil with a current of 100 mA. The full dimensions of the sensor geometry with its separate layers can be found in [2].

The shorter length of the magnetostrictive layer significantly decreases the output signal at a given excitation. However, it greatly improves the ability to localize and reconstruct the source signal. By carefully designing the sensor layers based on our findings, we aim to optimize ME sensors for both high spatial resolution for improved source reconstruction and maximum overall sensitivity for an improved limit of detection.

[1] D. Viehland, M. Wuttig, J. McCord, and E. Quandt, "Magnetoelectric magnetic field sensors," *MRS Bull.*, vol. 43, no. 11, pp. 834–840, 2018.
[2] M.-Ö. Özden, A. Teplyuk, Ö. Gümüs, D. Meyners, M. Höft, and M. Gerken, "Magnetoelectric cantilever sensors under inhomogeneous magnetic field excitation," *AIP Adv.* 10, 025132 (2020).

2022 International Conference on Electromagnetics in Advanced Applications (ICEAA) | 978-1-6654-8111-3/22/$31.00 ©2022 IEEE | DOI: 10.1109/ICEAA49419.2022.9900002

A joint magnetoelectric sensor and human head model for biomagnetic simulation

Mesut-Ömür Özden*(1) and Martina Gerken(1)
(1) Kiel University, Kiel, Germany, e-mail: omoz@tf.uni-kiel.de; mge@tf.uni-kiel.de

In recent years, thin-film magnetoelectric (ME) magnetic-field sensors have emerged as novel and advantageous devices for biomagnetic measurements. These ME sensors promise contactless readings of the magnetic fields generated by the human body, e.g., in magnetocardiography, with added benefits such as operation at room temperature without magnetic shielding [1]. The ME sensors considered here are based on strain-coupled thin-film magnetostrictive and piezoelectric layers on a cantilever. An incident magnetic field deforms the magnetostrictive layer which is coupled to a deformation of the piezoelectric layer giving a voltage signal. Previous studies often characterize the sensor performance under simplified homogeneous magnetic-field conditions. We have demonstrated that these sensors show a significantly different behavior under inhomogeneous magnetic-field excitation [2]. Here, we discuss a multiscale simulation approach using a joint sensor and simplified human head model for evaluation of sensor performance at different positions and orientations.

We use the classic anatomic three-shell human head model [3] employing different tissue types such as brain matter, skull, and skin with their respective electric and magnetic material parameters. Finite-element method (FEM) simulations are conducted for excitation with electric dipoles as models for deep-brain stimulation (DBS) electrodes. A full cantilever magnetoelectric sensor model [2] with layer thicknesses down to 20 µm and thinner layers approximated by boundary conditions is included in the simulation. With the multiscale model we can approximate electromagnetic field propagation through the head and secondary-source effects due to conductivity, leading to more accurate predictions of the sensor magnetoelectric response as a function of position and orientation. Figure 1 shows an example of the calculated magnetic flux density in the joint head and sensor model. An electric dipole source is placed within the brain domain, generating a magnetic flux density that propagates through the head and into the air domain surrounding it. The sensor geometry, as shown in the magnification, is exposed to the propagated magnetic field and picks up the signal. By using the full sensor model the exact electric response to the inhomogeneous magnetic field is calculated.

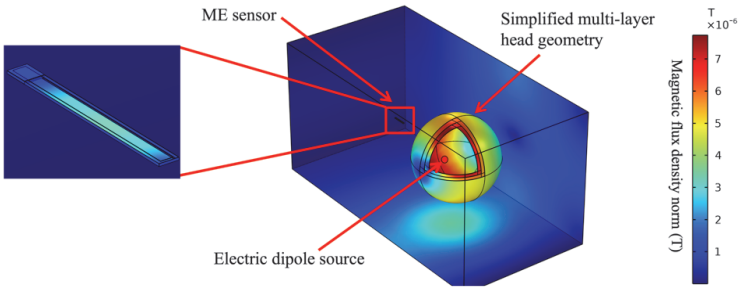

Figure 1. Multiscale FEM model including three-shell human head model with 16 cm diameter and magnetoelectric sensor with layer thicknesses down to 20 µm.

By utilizing the simplified joint ME sensor and head model and continuously increasing its complexity towards a more anatomically detailed head, we aim to achieve precise simulations of biomagnetic fields and to calculate the lead-field matrix of different sensor geometries and measurement setups such as sensor arrays around the head. This knowledge allows for adapted sensor design as well as improved placement of deep-brain stimulation (DBS) electrodes in the future.

1. E. Elzenheimer, C. Bald, E. Engelhardt, J. Hoffmann, P. Hayes, J. Arbustini, A. Bahr, E. Quandt, M. Höft, G. Schmidt, "Quantitative Evaluation for Magnetoelectric Sensor Systems in Biomagnetic Diagnostics", *MDPI Sensors*, vol. 22, 2022, pp. 1018.

2. M.-Ö. Özden, A. Teplyuk, Ö. Gümüs, D. Meyners, M. Höft, and M. Gerken, "Magnetoelectric cantilever sensors under inhomogeneous magnetic field excitation," *AIP Adv.*, vol. 10, 2020, pp. 025132.

3. Y. Huang, L. Parra, S. Haufe, „The New-York Head – A Precise standardized volume conductor model for EEG source localization and tES targeting", *Neuroimage*, vol. 140, 2016, pp. 150-162.